MINISTRY OF EDUCATION

THE ANNALS OF "DUNAREA DE JOS" UNIVERSITY OF GALATI

Fascicle IX
METALLURGY AND MATERIALS SCIENCE

YEAR XLII (XLVII)
December 2024, no. 4

ISSN 2668-4748; e-ISSN 2668-4756

GALATI UNIVERSITY PRESS

2024

EDITORIAL BOARD

THE ANNALS OF "DUNAREA DE JOS" UNIVERSITY OF GALATI
FASCICLE IX. METALLURGY AND MATERIALS SCIENCE
Nº. 4 - 2024, ISSN 2668-4748; e-ISSN 2668-4756
Volume DOI: https://doi.org/10.35219/mms.2024.4

Table of Contents

THE ANNALS OF "DUNAREA DE JOS" UNIVERSITY OF GALATI
FASCICLE IX. METALLURGY AND MATERIALS SCIENCE
Nº. 4 - 2024, ISSN 2668-4748; e-ISSN 2668-4756
Volume DOI: https://doi.org/10.35219/mms.2024.4

THE ANNALS OF "DUNAREA DE JOS" UNIVERSITY OF GALATI
FASCICLE IX. METALLURGY AND MATERIALS SCIENCE
N°. 4 - 2024, ISSN 2668-4748; e-ISSN 2668-4756
Article DOI: https://doi.org/10.35219/mms.2024.4.01

RESEARCH ON THE INFLUENCE OF FLOODS ON THE PHYSICAL CHARACTERISTICS OF SOIL

Beatrice Daniela TUDOR
"Dunarea de Jos" University of Galati, Romania
e-mail: beatrice.tudor@ugal.ro

ABSTRACT

The paper presents research on the influence of floods in the hydrographic basin of Siret River, on the soil. Soil moisture and porosity were determined to observe the influence of excess water in the floodplain area, where the soil is marshy, on the possible deterioration of soil properties, and possible landslides in the Siret riverbank area.

KEYWORDS: soil, humidity, porosity

1. Introduction

Floods are potentially very destructive events that occur when land surfaces are covered with a significant amount of water. They negatively impact the quality of life, through material damage and human casualties.

The trend of flooding is becoming more and more prevalent due to changing climatic conditions due to pollution and massive deforestation.

The main physical characteristics of the soil are: soil texture, soil structure, soil density, soil porosity, degree of subsidence, soil compaction, resistance to soil works, soil plasticity, soil swelling and contraction, adhesion and external friction, cohesion and internal friction [1, 3].

2. Experimental research on soil humidity and porosity in a flood-prone area

Soil moisture and porosity were determined on soil samples taken from the Movileni floodplain, in the hydrographic basin of Siret River. Soil samples were taken according to the requirements of STAS 17.4.4.02-84 "Nature protection. Soils. Methods of collection and preparation of samples for chemical, bacteriological and helminthological analysis", as well as STAS 28168-89 "Soils. Sample collection" [2]. The samples were taken from different depths of 10, 20 and 30 cm, respectively from a high flood risk area in the Siret River basin, Movileni village.

The soil was collected in hermetically sealed containers, so that water would not evaporate during transport, and the samples were kept in the refrigerator for no more than 24 hours [4].

3. Determination of soil moisture by gravimetric method

To determine soil moisture, the gravimetric method was used. The soil samples were dried at 105 °C in an oven until constant weight was reached and then each sample was weighed. The difference in weight obtained before and after drying represents the moisture content, which is expressed as a percentage.

The weighing was done on an analytical balance (Fig. 1).

Fig. 1. *Weighing the soil sample*

The weighing vial is placed uncovered, together with its lid, in an oven at a temperature of 105 °C, for 2 hours (Fig. 2).

THE ANNALS OF "DUNAREA DE JOS" UNIVERSITY OF GALATI
FASCICLE IX. METALLURGY AND MATERIALS SCIENCE
Nº. 4 - 2024, ISSN 2668-4748; e-ISSN 2668-4756
Article DOI: https://doi.org/10.35219/mms.2024.4.01

Fig. 2. *The oven used in the experimentation*

The sample is kept for 15 minutes, after which it is left to cool in a desiccator, with calcium chloride, for 30 min. It is then weighed on an analytical balance. The operation is repeated until the difference between two successive weightings is no greater than 0.0002 g (in most cases two dryings were sufficient).

In the weighing vial brought to constant weight, approximately 50 g of soil prepared for analysis were immediately introduced, after which it was weighed on an analytical balance. The difference from the weight of the empty weighed vial represents the mass of the soil taken for the determination of hygroscopic humidity. The weighing vial with the soil sample is placed uncovered, together with its lid, in the electric oven at a temperature of 105 ºC, and kept for 2 hours.

The drying operation is repeated by keeping the soil sample in the oven at a temperature of 105 ºC, until the difference between the last two successive weighing is less than 0.0002 g, i.e. the mass remains practically constant. All manipulations with the weighing vial are done with the help of laboratory pliers, to avoid the adhesion of impurities from the fingers on the walls of the vial.

The formula used to calculate soil moisture is:

$$U\ [\%] = (M\ water)/(M\ soil)\ X\ 100$$

where: M soil = soil mass after drying for one hour at 105 °C;

M water = M soil with water - M dry soil

To calculate the moisture content of the 3 soil samples, we weighed 50 g of soil before drying in the oven. After several successive weighing, when the soil mass remained constant, the moisture content was calculated.

The data obtained from calculating the humidity of the 3 samples were centralized in Table 1.

Table 1. *Values for humidity*

Sample	Soil before drying [g]	Soil after drying [g]	Humidity [%]
P 1 (collected from 10 cm depth)	50	41.936	83.87
P 2 (collected from 20 cm depth)	50	41.745	83.49
P 3 (collected from 30 cm depth)	50	41.734	83.46

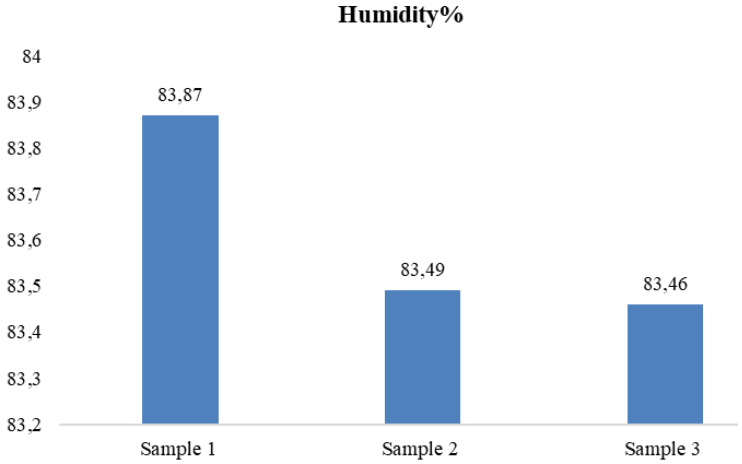

Fig. 3. *Humidity of soil samples*

THE ANNALS OF "DUNAREA DE JOS" UNIVERSITY OF GALATI
FASCICLE IX. METALLURGY AND MATERIALS SCIENCE
Nº. 4 - 2024, ISSN 2668-4748; e-ISSN 2668-4756
Article DOI: https://doi.org/10.35219/mms.2024.4.01

The graphic in Fig. 3 illustrates the values obtained for moisture for the three soil samples.

From the calculation of humidity and the graph we can say that at sample 1 (harvested from 10 cm), the highest humidity was obtained, because this soil was a swampy soil, saturated with water.

At sample 2 (harvested from a depth of 20 cm), the humidity is much lower and in sample 3 (harvested from 30 cm) depth, the humidity is very close to sample 2 with small decreases in humidity values.

4. The determination of soil porosity

For uncultivated soil, porosity values decrease with the depth of the sampling layer. The area from which we collected the samples is an uncultivated and floodable area.

Soil density depends on: the mineralogical composition, respectively the humus content and provides data on: the composition of the soil, the proportion between the mineral and organic part, the calculation of porosity and the determination of the granulometric composition of the soil.

Generally, a good porosity is considered to be that which allows the continuous circulation of air and water in the soil. Such porosity appears in soil horizons with a granular/glomerular structure, loose, rich in organic matter, with a clayey texture and characterized by intense biological activity. Within these horizons, porosity is stable, being weakly influenced by variations in the humidity regime, reaching values of 50-60% [5, 6].

Porosity is unfavourable in clayey or unstructured horizons, with high clay content, in which the pore spaces decrease greatly with increasing humidity. In these horizons, water stagnates, the soil not being aerated.

Porosity influences:

- the dynamics of gas exchange between the soil and the atmosphere;
- the quantitative and qualitative functionality of rivers and groundwater;
- it determines the recharge of the groundwater, the flow regime of rivers, and also influences their chemical composition;
- triggering of surface erosion;
- plant development.

To determine the porosity, 50 g of compacted soil, which I had previously prepared by crushing, was weighed on an analytical balance. After weighing and preparation, I introduced the soil sample into a 100 mL graduated cylinder (Fig. 4.).

Fig. 4. *Graduated cylinder with soil sample*

Part of the added water infiltrates into the soil, filling its pores and displacing the respective air. The volume occupied by the soil together with water is read on the cylinder. The number of mL that constitutes the difference between 100 and the volume occupied by the soil together with water represents the pore volume.

The water and soil samples are left for 24 hours after which the pore volume is read and calculated (Fig. 5).

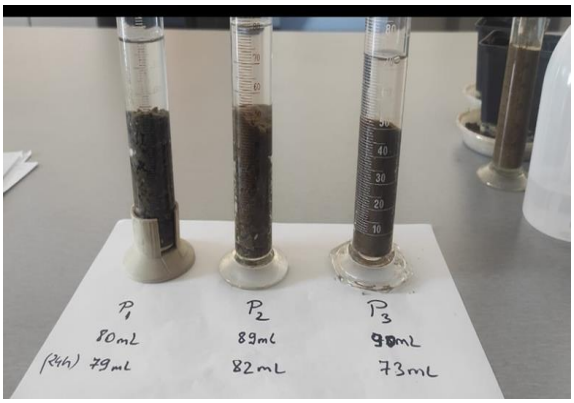

Fig. 5. *Pore volume, reading after 24 hours*

Calculation of porosity of soil samples:

Pore volume = 100 - Vt (water + soil)

For sample P1 collected from a depth of 10 cm (boggy soil):

P1: 50 g soil + 50 mL water

The volume of soil and water read immediately after inserting the sample into the cylinder is = 80 mL

Vt water + soil = 80 mL

V pores = 100 - 80 = 20 mL (air)

After 24 hours we calculated the porosity of sample P1:

Porosity (P1) after 24 h = ((100 - 79) · 100)/50= 21 · 2 = 42%

THE ANNALS OF "DUNAREA DE JOS" UNIVERSITY OF GALATI
FASCICLE IX. METALLURGY AND MATERIALS SCIENCE
Nº. 4 - 2024, ISSN 2668-4748; e-ISSN 2668-4756
Article DOI: https://doi.org/10.35219/mms.2024.4.01

For sample P2 collected from a depth of 20 cm (wet soil):

P2 50 g soil + 50 mL water

The volume of soil and water read immediately after inserting the sample into the cylinder is = 89 mL

Vt water + soil = 89 mL

V pores = 100 - 89 = 11 mL (air)

After 24 hours we calculated the porosity of sample P2:

Vt water + soil = 82 mL

Porosity (P2) after 24 h = ((100 - 82) · 100)/50 = 18 · 2 = 36%

For sample P3 collected from a depth of 30 cm (wet-dry soil):

P3 50 g soil + 50 mL water

The volume of soil and water read immediately after inserting the sample into the cylinder is = 90 mL

Vt water + soil = 90 mL

V pores = 100 - 90 = 10 mL (air)

After 24 hours we calculated the porosity of sample P3:

Vt water + soil = 73 mL

Porosity (P3) = ((100 - 73) · 100)/50 = 25 · 2 = 54%

The data obtained from the porosity determinations are summarized in Fig. 6.

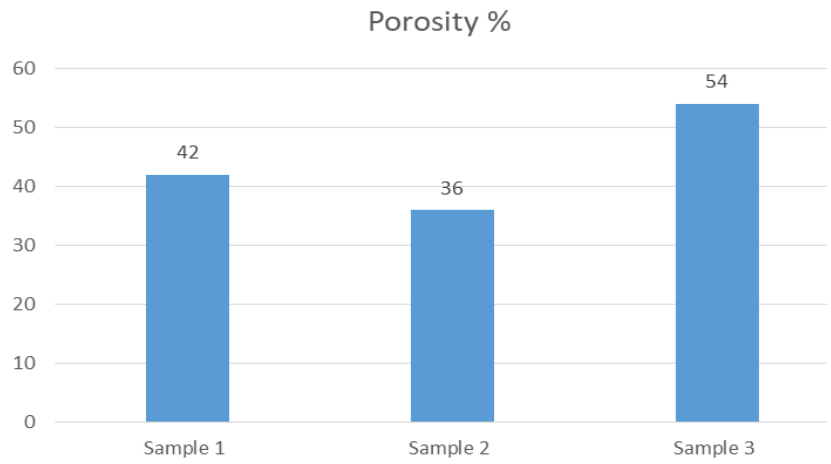

Fig. 6. *Humidity of soil samples*

5. Conclusions

Floods negatively influence the quality of life through material damage and human casualties. Due to climate change, the rainfall and hydrological levels of rivers have changed, increasing the risk of flooding, especially in the downstream areas of the river basins.

The determination of soil moisture and porosity was aimed at seeing how excess water from a floodplain area, where we had a swampy soil, influences some physical characteristics of the soil and its possible damage that can lead to landslides in the area.

Following the moisture determinations, at the sample collected from a depth of 10 cm, the highest moisture was obtained, because this soil was a swampy soil, saturated with water.

In the sample collected from a depth of 20 cm, the humidity is much lower and, in the sample, collected from a depth of 30 cm, the humidity is very close to sample 2 with small decreases in humidity values.

Regarding porosity, in the sample collected from 30 cm, we obtained the highest value, because at this depth the water did not fill the volume of the pores in the soil.

In the sample collected from a depth of 20 cm, the porosity is lower than in the sample collected from a depth of 10 cm, because the water infiltrated and occupied the volume of the pores.

References

[1]. Aurel Saracin, *Topografie*, Editura Matrix Rom Bucuresti, 2005.
[2]. Constantin Cosarca, *Topografie Ingineresca*, Matrix Rom Bucuresti, 2003.
[3]. Radu Mihăiescu, *Monitoringul integrat al mediului*, Cluj-Napoca, 2014.
[4]. ***, http://enviro.ubbcluj.ro/studenti/cursuri%20suport/Carte_Monitoring_Radu_SITE.pdf.
[5]. ***, http://www.mmediu.ro/protectia_mediului/calitate_aer.htm.
[6]. ***, https://inundatii.ro/wpcontent/uploads/2022/07/PFRAReportRO10Siret.pdf.

THE ANNALS OF "DUNAREA DE JOS" UNIVERSITY OF GALATI
FASCICLE IX. METALLURGY AND MATERIALS SCIENCE
Nº. 4 - 2024, ISSN 2668-4748; e-ISSN 2668-4756
Article DOI: https://doi.org/10.35219/mms.2024.4.02

ON THE DISPERSION OF GASES DISCHARGED TO THE CHIMNEY OF A THERMAL POWER PLANT

Adrian LEOPA
"Dunarea de Jos" University of Galati, Engineering and Agronomy Faculty of Braila,
Calarasilor Street, 29, RO-810017, Braila, Romania
e-mail: adrian.leopa@ugal.ro

ABSTRACT

This paper presents a theoretical study on the dispersion of gaseous pollutants from a natural gas thermal power plant in the event of a malfunction. Using the Gaussian model, the dispersion of nitrogen oxides generated by such a thermal power plant was evaluated across different atmospheric stability classes. This allowed for an assessment of whether the concentration of this pollutant meets the maximum permissible limits established by Romanian laws, as well as an identification of the affected areas.

KEYWORDS: dispersion, gaussian, nitrogen oxides, atmospheric stability

1. Introduction

Currently, the air pollution situation is causing concerns at all levels of society, having a significant impact on public health, the environment and the economy. Most specialists in the field believe that we can talk about significant anthropogenic air pollution starting with the first industrial revolution, 1760-1840, when the steam engine was perfected and the use of coal was widely used, especially in the textile industry. This revolution marked a turning point in the evolution of human society, transitioning from an agrarian and artisanal economy to one based on industry and mechanized production. From this point forward, people's hopes for a better life took on new dimensions, given the advantages brought by the Industrial Revolution. However, one of the side effects of this industrial development was the release of gaseous pollutants into the atmosphere, such as SO_2, CO, CO_2, NO_x, VOCs, PM, and others.

At European level the Directive 2008/98 CE imposes that "by 2020, the preparing for re-use, recycling and other material recovery, including backfilling operations using waste to substitute other materials, of non-hazardous construction and demolition waste excluding naturally occurring material defined in category 17 05 04 in the list of waste shall be increased to a minimum of 70% by weight". Considering the harmful effects on human health and beyond, the phenomenon of air pollution has drawn the attention of authorities, leading to the implementation of measures aimed at regulating this field. The link between air pollution and related diseases dates to 400 BC, with Hippocrates addressing this topic in his writings [1]. Gradually, due to the continuous increase in air pollution, various legislative norms were introduced to reduce this type of pollution. For example, in England, the Smoke Abatement Act was passed in 1273 [1].

Awareness of the link between air pollution and its environmental issues led to international measures, culminating in the Human Environment Summit in Stockholm in 1972 under the auspices of the United Nations. Representatives from 113 participating countries adopted a declaration containing 26 fundamental principles regarding environmental protection. Following this event, other international summits addressing topics in this area occurred periodically; however, agreements among signatory countries have not succeeded in halting the rise in air pollution.

It is up to all of us to recognize the danger that this phenomenon poses to ourselves and to future generations.

2. Urban Air Pollution

Urban agglomerations have emerged as an inherent effect of human societal development, offering advantages such as easier access to services, education, healthcare, and culture. However, they also have disadvantages, including air pollution.

THE ANNALS OF "DUNAREA DE JOS" UNIVERSITY OF GALATI
FASCICLE IX. METALLURGY AND MATERIALS SCIENCE
Nº. 4 - 2024, ISSN 2668-4748; e-ISSN 2668-4756
Article DOI: https://doi.org/10.35219/mms.2024.4.02

In Romania, an important source of air pollution comes from activities related to heating homes during the cold season and providing hot water.

In other words, the abandonment of centralized heating systems in many Romanian cities resulted in the shift of pollution from outside to inside the city, leading to a series of adverse consequences for urban residents.

In addition to contributing to the transformation of cities into "heat islands," they also have a negative impact on human health by emitting toxic gases such as NOx and CO.

Natural gas-fired thermal power plants have become an important source of urban air pollution in recent years, especially in localities where centralized hot water distribution systems have been dismantled.

3. Evaluation of Flue Gas Dispersion from a Heating Plant Using the Gaussian Model for a Continuous Source

Typically, methane gas-fired boilers are not considered polluting if CO_2 emissions are excluded. However, in cases of wear or faulty combustion, they can become significant sources of pollution. Under these conditions, understanding the dispersion of flue gases from such a plant is of particular interest.

As a case study for this scenario, we will consider the thermal power plant located in a historic building in the municipality of Braila, which currently houses the Faculty of Engineering and Agronomy, Fig. 1.

The heating plant responsible for supplying thermal energy is equipped with two GAS XP60CE burners, each with a capacity ranging from 232 to 522 kW, Fig. 2.

Fig. 1. *The headquarters of the Faculty of Engineering and Agronomy in Braila: 1. Heating Plant Room; 2. Flue Gas Stack*

Fig. 2. *Heating Plant*

THE ANNALS OF "DUNAREA DE JOS" UNIVERSITY OF GALATI
FASCICLE IX. METALLURGY AND MATERIALS SCIENCE
N°. 4 - 2024, ISSN 2668-4748; e-ISSN 2668-4756
Article DOI: https://doi.org/10.35219/mms.2024.4.02

3.1. Mathematical Model

To evaluate the dispersion of the exhaust gases from this plant into the atmosphere, the Gaussian model for continuous sources will be applied. Assuming the wind direction aligns with the OX axis, the evolution of the plume will follow the pattern shown in Fig. 3.

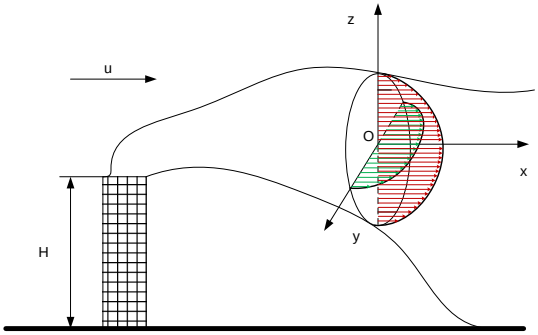

Fig. 3. *Dispersion of the pollutant plume*

Given that pollutant dispersion along the OX direction can be neglected relative to advection, the well-known Gaussian equation characterizing the pollutant concentrations emitted from the chimney can be expressed by equation (1):

$$C(x,y,z,H) = \frac{Q}{2\pi\sigma_y\sigma_z u} e^{-\frac{y^2}{2\sigma_y{}^2}} \left\{ e^{\left[-\frac{(z-H)^2}{2\sigma_z{}^2}\right]} + e^{\left[-\frac{(z+H)^2}{2\sigma_z{}^2}\right]} \right\}$$

where:

Q - pollutant emission rate, μg/s;
x, y, z - coordinates of the axis system;
z - the height at which the concentration of the pollutant is assessed;
u - wind speed;
H - chimney height;
σ_y, σ_z - dispersion parameters, it was considered that the dispersion is insignificant in the Ox direction in relation to the distance travelled in the wind direction.

3.2. Stability of the atmosphere

Atmospheric stability is an important factor in the dispersion of pollutants. In a stable atmosphere, air tends to remain at the same altitude, while in an unstable atmosphere, air can exhibit upward and/or downward movements.

The stability classes were defined according to the Procedures for Evaluating Air Quality Impact of New Stationary Sources, EPA [4], Table 1.

Table 1. *Atmospheric stability classes*

Surface wind speed (m/s)	Daytime insolation			Nighttime	
	Strong	Moderate	Slight	Thin overcast > 4/8 low cloud cover	< 3/8 cloud cover
< 2	A	A- B	B	-	-
2- 3	A- B	B	C	E	F
3- 5	B	B- C	C	D	E
5- 6	C	C- D	D	D	D
> 6	C	D	D	D	D
A: very unstable, B: unstable, C: moderately unstable, D: neutral, E: stable, F: very stable					

3.3. Dispersion Parameters

Since, in this case, the wind speed is constant and the emission of flue gases is steady, the dispersion parameters have been evaluated based on the relationships established by Briggs-McElroy-Pooler for urban conditions, Table 2.

4. Simulation of an Emergency Situation

A failure scenario was simulated in which the plant in question does not operate within nominal parameters, releasing harmful gases into the atmosphere, specifically nitrogen oxides (NOx). The Gaussian model for continuous sources was used to evaluate the dispersion of nitrogen oxides discharged from the plant's chimney under different atmospheric stability classes.

The numerical solution of the equation evaluating the Gaussian dispersion of the considered pollutant was carried out under the following assumptions: wind speed and direction are constant; the emission rate of the pollutant is constant; meteorological conditions in the horizontal direction

THE ANNALS OF "DUNAREA DE JOS" UNIVERSITY OF GALATI
FASCICLE IX. METALLURGY AND MATERIALS SCIENCE
No. 4 - 2024, ISSN 2668-4748; e-ISSN 2668-4756
Article DOI: https://doi.org/10.35219/mms.2024.4.02

(OX) are constant; the atmospheric stability class is constant; the mixing height is constant; the pollutant does not undergo chemical reactions over short distances; NOx mass flow rate, r = 1.62 g/m^3; exhaust gas flow rate, Q = 473.4 m^3; exhaust area, S = 0.24 m^2; height of the exhaust chimney, h = 17 m; gas temperatures at the exit of the chimney, T = 137 ^{o}C. The Matlab programming environment was used for the graphical representation of the pollutant plume, considering different combinations of atmospheric stability classes and wind speed [6-8].

Table 2. *Dispersion coefficients: Analytical formulas of Briggs-McElroy-Pooler,* [5]

Briggs-McElroy-Pooler		
Stability	σ_y	σ_z
Urban conditions		
A - B	$0.32\ x\ (1 + 0.0004\ x)^{-1/2}$	$0.24\ x\ (1 + 0.001\ x)^{-1/2}$
C	$0.22\ x\ (1 + 0.0004\ x)^{-1/2}$	$0.20\ x$
D	$0.16\ x\ (1 + 0.0004\ x)^{-1/2}$	$0.14\ x\ (1 + 0.0003\ x)^{-1/2}$
E - F	$0.11\ x\ (1 + 0.0004\ x)^{-1/2}$	$0.08\ x\ (1 + 0.00015\ x)^{-1/2}$

For the same atmospheric stability class, A, but with different wind speeds, it is observed that the maximum pollutant concentration occurs at the lower speed, specifically 17.6 µg/m^3 at 72 m from the source, Fig. 4. When the wind speed is 2 m/s, the maximum concentration decreases to 4.4 µg/m³, occurring at 289 m from the source, Fig. 5. The same graphical representations show that as wind speed increases, the area affected by the pollutant also expands. For a pollutant concentration of 1 µg/m³, the difference between the points where this value is reached is approximately 500 m greater when the wind speed is 2 m/s.

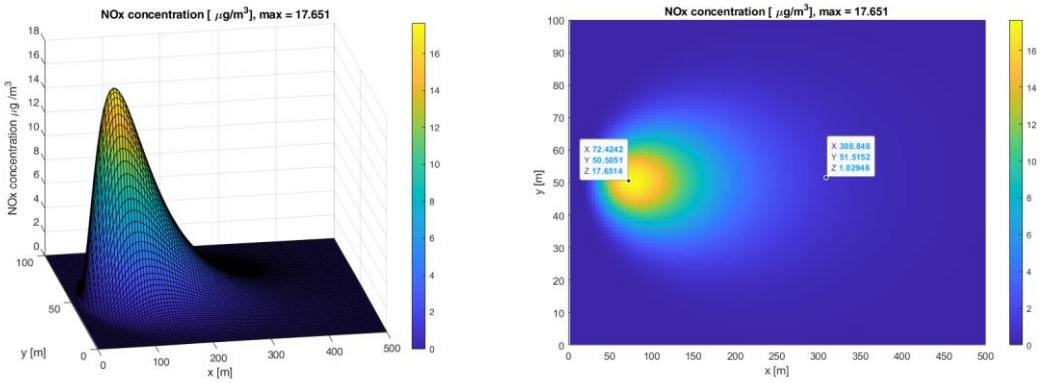

a. 3D representation *b. 2D representation*

Fig. 4. *Dispersion of the pollutant plume for atmospheric stability class A and wind speed v = 0.5 m/s*

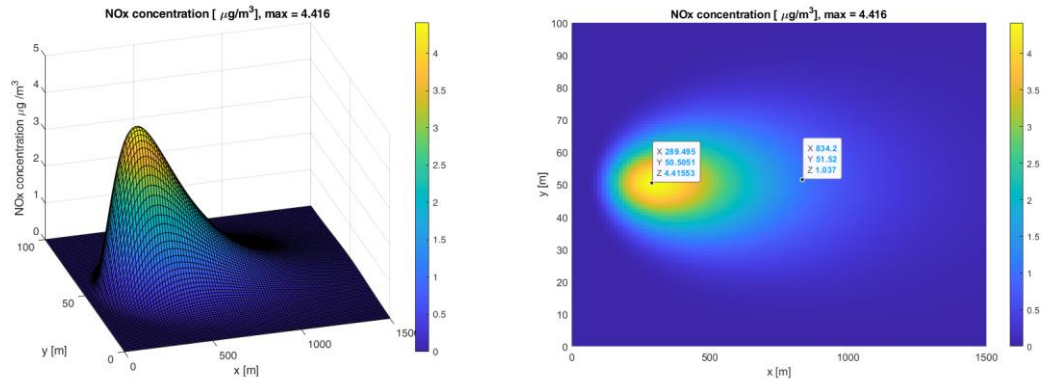

a. 3D representation b. 2D representation

Fig. 5. *Dispersion of the pollutant plume for atmospheric stability class A and wind speed v = 2 m/s*

THE ANNALS OF "DUNAREA DE JOS" UNIVERSITY OF GALATI
FASCICLE IX. METALLURGY AND MATERIALS SCIENCE
Nº. 4 - 2024, ISSN 2668-4748; e-ISSN 2668-4756
Article DOI: https://doi.org/10.35219/mms.2024.4.02

For atmospheric stability class C and a wind speed of 2 m/s, the maximum pollutant concentration and the distance from the source at which a concentration of 1 μg/m³ is reached are very similar to those observed for atmospheric stability class A at the same wind speed, Fig. 6.

For stability class C and a wind speed of 3 m/s, the maximum ground-level concentration is only 2.71 μg/m^3 at 506 meters from the emission source, while a concentration of 1 μg/m³ is reached at 1132 meters, Fig. 7. For atmospheric stability class D and a wind speed of 6 m/s, the maximum pollutant concentration decreases to 0.88 μg/m^3, reached at1273 m from the source, Fig. 8.

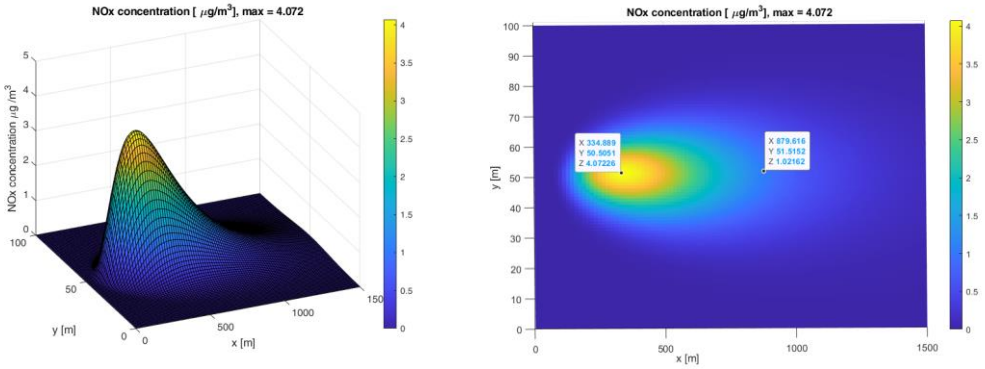

a. 3D representation *b. 2D representation*

Fig. 6. *Dispersion of the pollutant plume for atmospheric stability class C and wind speed v = 2 m/s*

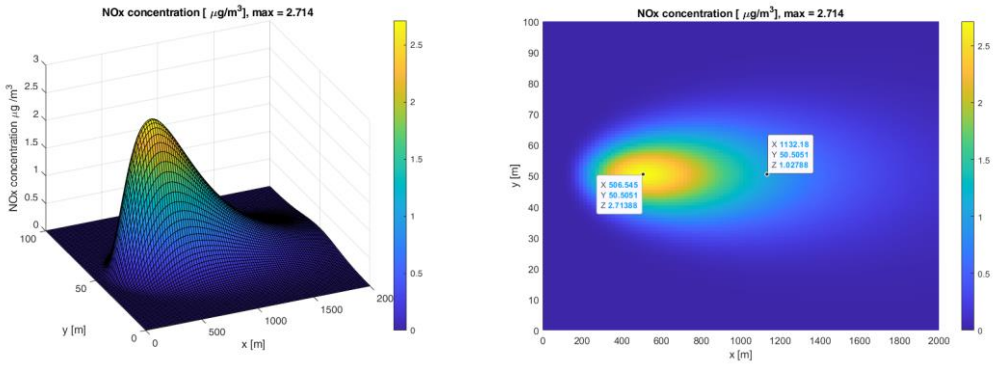

a. 3D representation b. 2D representation

Fig. 7. *Dispersion of the pollutant plume for atmospheric stability class C and wind speed v = 3 m/s*

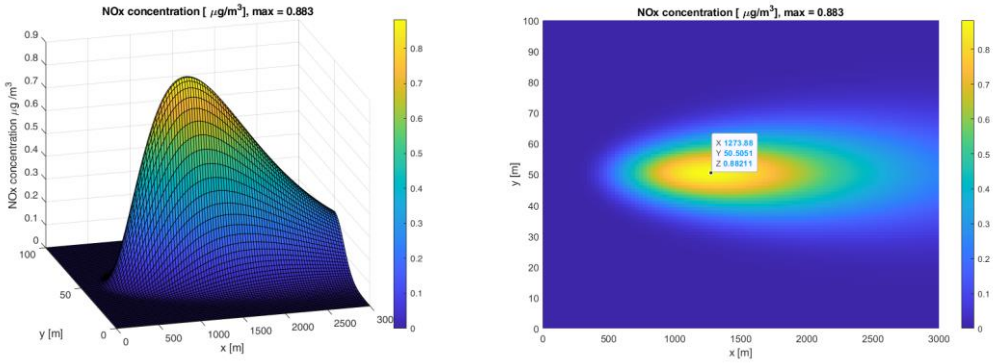

a. 3D representation b. 2D representation

Fig. 8. *Dispersion of the pollutant plume for atmospheric stability class D and wind speed v = 6 m/s*

THE ANNALS OF "DUNAREA DE JOS" UNIVERSITY OF GALATI
FASCICLE IX. METALLURGY AND MATERIALS SCIENCE
Nº. 4 - 2024, ISSN 2668-4748; e-ISSN 2668-4756
Article DOI: https://doi.org/10.35219/mms.2024.4.02

For atmospheric stability class E-F and a wind speed of 5 m/s, the maximum pollutant concentration decreases to 0.41 µg/m^3, reached at a distance of 1455 meters from the source, Fig. 9.

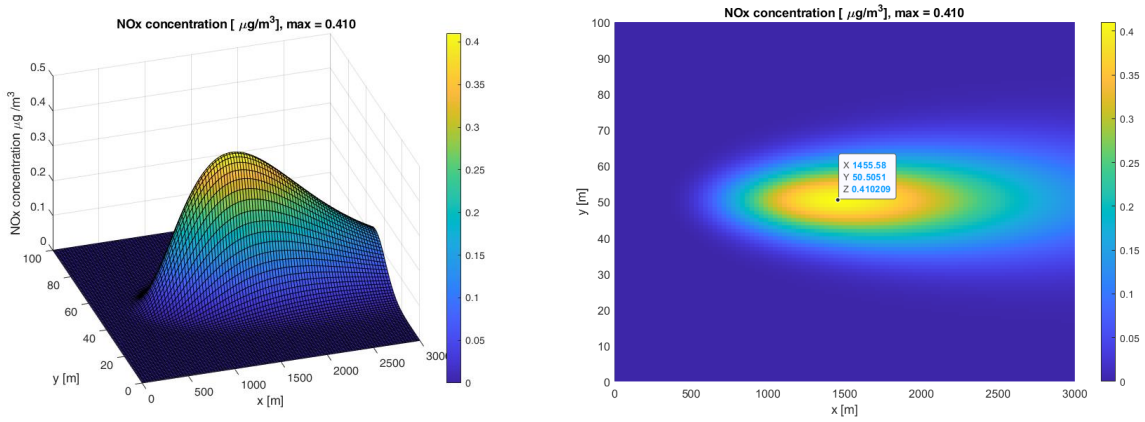

a. 3D representation b. 2D representation

Fig. 9. *Dispersion of the pollutant plume for atmospheric stability class E-F and wind speed 5 m/s*

5. Conclusions

The NOx concentration determined in the considered cases is below the maximum permissible values regulated in Romania by law no. 104/2011 on ambient air quality. This theoretical study is particularly important when planning the placement of a system that generates atmospheric pollutants with pathogenic effects on human health, as the Gaussian model allows for the evaluation of pollutant dispersion based on operating conditions and atmospheric stability class. Additionally, this model can be used to simulate the dispersion of gaseous pollutants in the event of malfunctions in combustion systems at various continuously operating installations.

References

[1]. Fowler D., *et al.*, *A chronology of global air quality*, Philosophical Transaction Royal Society a Mathematical, Phisical and Engineering Science, 2020.
[2]. ***, https://www.visualcapitalist.com/global-temperature-graph-1851-2020/.
[3]. Cuculeanu G., *Gaussian approach of the atmospheric pollutant diffusion*, https://www.asecib.ase.ro/simpozion/2009/full_papers/pdf/31_Cuculeanu-ro.pdf.
[4]. Alen and Durrenberger, *Gaussian Plume modeling*, Chemical Engineering, 357.
[5]. Kavishwar S. M., ***et al.***, *Dispersion Modeling of Hazardous Chemicals with MATLAB Software in the View of Safety*, IJMEIT, vol. 2, issue 10, 2014.
[6]. Stockie J., *The mathematics of atmospheric dispersion modelling*, Society for Industrial and Applied Mathematics, vol. 53, no. 2, p. 349-372, 2011.
[7]. Holzbecher E., *Environmental Modeling Using MATLAB*, Springer, 2012.
[8]. Ghinea M., Fireteanu V., *Calcul numeric, grafica, aplicatii*, Teora, 2008.

THE ANNALS OF "DUNAREA DE JOS" UNIVERSITY OF GALATI
FASCICLE IX. METALLURGY AND MATERIALS SCIENCE
Nº. 4 - 2024, ISSN 2668-4748; e-ISSN 2668-4756
Article DOI: https://doi.org/10.35219/mms.2024.4.03

PHYSICO-CHEMICAL CHARACTERIZATION OF SOIL SAMPLES FROM BÂRLAD MUNICIPALITY

Gina Genoveva ISTRATE, Andreea Liliana LAZĂR, Eliza DĂNĂILĂ
Interdisciplinary Research Centre in the Field of Eco-Nano Technology and Advance Materials CC-ITI, Faculty of Engineering, "Dunarea de Jos" University of Galati, 111 Domneasca Str., 800008, Galati, Romania
e-mail: gina.istrate@ugal.ro

ABSTRACT

Soil quality is now thought of in a way that emphasises functionality in a broad context, involving soil not only as an environment for crop production but also as an important reservoir for water storage, as a buffer for filtering, transforming, and neutralising pollutants, and as a habitat for plants and animals. Some attributes (pH, soil conductivity, etc.) can be associated with several easily identified threats to soil quality, some of which are interrelated in the same way. For the present work, laboratory analyses were carried out to determine the physico-chemical parameters of soil from different areas. For soil quality analysis, the following parameters were determined: pH, conductivity, acidity, alkalinity, total nitrogen, aluminium, phosphates, iron, heavy metals, calcium, and magnesium content in the soil.

KEYWORDS: aqueous soil extract, acidity, alkalinity, heavy metal

1. Introduction

The continuous growth of the population requires the highest quality and highest possible agricultural production. Some of the measures that can lead to increased agricultural production are those that increase production per unit area and those that bring unproductive land into agricultural use. Solving these problems is based first and foremost on a thorough knowledge of the soil as the main means of agricultural production [1, 2].

As agriculture is the main source of food for a growing world population, the sustainability of agricultural production is a problem of great concern for the human race.

More attention is now being paid to increasing the country's arable land area through the cultivation of new land and to preventing and combating soil pollution resulting from various anthropogenic activities (industrial, agricultural, etc.) [1].

Climate change is also expected to increasingly affect Romania and its agricultural sector in the medium and long term. Romania will have to expect a steady increase in average annual temperature, similar to projections for Europe, which can vary between 0.5 °C and 1.5 °C by 2029 and between 2.0 °C and 5.0 °C by 2099, depending on the global scenario. Precipitation patterns are expected to change significantly and have a differentiated territorial impact in Romania. The northern part of the country is likely to see gains in crop productivity in the medium term but will be subject to high winter rainfall and water shortage problems in summer. Southern and south-eastern Romania will be more severely affected and heat waves and droughts will lead to a general decrease in crop production and productivity [4].

Soil acidity is determined by dissociated H+ cations in water or saline solutions upon contact with the solid phase (actual or dissociated acidity) and by H^+ and Al^{3+} cations adsorbed on the surface of colloidal particles (potential or adsorbed acidity). Soil acidity controls the solubility and precipitation of the chemical compounds of all essential plant nutrients and is therefore a decisive factor in their availability.

Understanding the nature of soil acidity and managing it is an integral part of soil fertility. Soil acidity has a widespread influence on soil fertility and plant growth. For example, in strongly acid soils (pH < 5) Ca, Mg, P, B, and Mo become deficient, while Mn and Fe can reach toxic limits. Aluminium toxicity is also a serious problem for these soils. Similarly, the availability of Cu, Fe, Zn, and Mn is reduced in calcareous alkaline soils. In mineral soils, the pH for the highest availability of most nutrients is 6.5, while in organic soils (peat and mud) the optimum pH is around 5.5. For soils in our country, pH values range

THE ANNALS OF "DUNAREA DE JOS" UNIVERSITY OF GALATI
FASCICLE IX. METALLURGY AND MATERIALS SCIENCE
Nº. 4 - 2024, ISSN 2668-4748; e-ISSN 2668-4756
Article DOI: https://doi.org/10.35219/mms.2024.4.03

from 3.5 to 9.5 or 10-11 in the case of solonetz or sodic solonchak [1-3].

In addition, the pH affects the solubility and effectiveness of certain toxic chemicals (such as aluminium) and plants can absorb them [5].

The soil's pH has a direct association with the bacterial community in the ecosystem, which has a direct effect on soil acidification. Most microorganisms have an optimal pH range for survival and functioning [6].

A strong acidic or alkaline pH, due to the weak activities of bacteria-bound microbes determine the mineralisation of organic matter in the soil to slow down or stop. As a result, certain diseases will increase under conditions of low soil pH (acidic) or high soil pH (alkaline) [7].

Bacterial diversity and microbial activity are increased at higher pH values and decreased at lower soil pH values. Therefore, pH is a good predictor of bacterial community structure. Some environmental factors that define soil pH are mineral concentrations, erosion, mineralogy, and water balance [8-13].

Soil alkalinity can be natural or caused by human activity. Natural alkalinity is the result of the release of Na_2CO_3 from the soil through watering, while anthropogenic alkalinity, caused by human activities, is due to the application of fertilisers and irrigation water with high $NaHCO_3$ content [2].

Alhagi camelorum is a perennial plant widely distributed in Asia, Europe, America, and Australia, with reported uses in pharmaceuticals, animal feed and soil conservation. Alhagi may be a good indicator of soil alkalinity and could be considered a sign of low alkalinity and low salinity of soils in arid and rigid terrestrial ecosystems [14].

Plants take up calcium and magnesium in the form of Ca^{2+} and Mg^{2+}, available cations in most soils, although Mg deficiency is more common than Ca deficiency. Like calcium, magnesium can be easily leached and soils with low cation exchange capacity have low magnesium content. It is important that there is a balance of Mg, K, and Ca ions in the soil because these elements are dominant in areas with high cation exchange capacity. Since most soils with a pH of 7.0 or higher have abundant Ca and even Mg, it is generally not necessary to add these nutrients to crops each season [2, 3].

For example, chemical remedies could be used to alter the composition of cations adsorbed by soil aggregates. This would promote the formation of aggregate structures, improve soil structures and delay the return of soil salinisation. The most effective way to ensure the survival and sustainability of plant communities is to grow salt-tolerant halophytes [20].

In this study, determinations were performed for three types of soil taken from a depth of 10 cm: soil taken from a field in the area of Bârlad (Sample 1-P1), soil taken from the vicinity of the bearing factory in Bârlad (Sample 2- P2), and a garden soil sample taken from the area of Bârlad (Sample 3-P3).

For soil quality analysis, the following parameters were determined: pH, conductivity, acidity, alkalinity, total nitrogen, aluminium, phosphates, iron, heavy metal, calcium, and magnesium content in the soil.

To carry out the laboratory analyses, it was necessary to obtain an aqueous soil extract in a ratio of 1:5 by mixing 100 g soil with 500 mL distilled water. The mixture was stirred for one hour at medium speed for homogenization. After the stirring was completed, the aqueous soil extract was filtered through filter paper. The filtration operation is repeated as often as necessary to obtain a clear extract as possible for the next step, i.e. the above-mentioned analyses.

2. Results and discussions

Determining the soil's pH

The pH is the concentration of hydrogen ions in a solution, and the pH scale ranging from 0 to 14 units is used to measure the acidic and basic character of the solution. The natural pH of soil depends on the rock from which the soil was formed (base material) and the weathering processes that have acted on it – for example, climate, vegetation, topography, and time. These processes tend to cause a decrease in pH (increase in acidity) over time. Some agricultural activities can also accelerate the acidification process.

There are several methods to determine soil pH, but a portable HACH Multiparameter was used to monitor the pH of the aqueous soil extract in our field of interest.

Figure 1 shows the results obtained from the pH determination of aqueous soil extract.

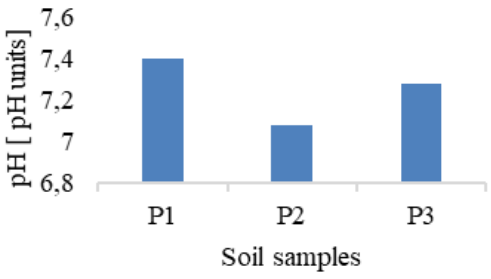

Fig. 1. *Results obtained after determining the pH of the aqueous soil extract*

It can be seen from the attached chart that the analysed soil has close pH values ranging from the lowest value of 7.08, which is the soil near the bearing factory, to a value of 7.4 pH units, which is

THE ANNALS OF "DUNAREA DE JOS" UNIVERSITY OF GALATI
FASCICLE IX. METALLURGY AND MATERIALS SCIENCE
Nº. 4 - 2024, ISSN 2668-4748; e-ISSN 2668-4756
Article DOI: https://doi.org/10.35219/mms.2024.4.03

the field soil. From these determinations, it can be concluded that the soil closest to neutral pH is sample 2.

The soil's reaction (soil pH) is of particular importance for the general characterization of soils, as well as for agricultural practice. It depends on the supply of nutrients to the soil.

Determining the soil's conductivity

Conductivity (also known as electrical conductivity or EC for short) is a measure of the ability of a substance to conduct an electric current and can be measured using a conductivity meter. In the agriculture and farming industry, conductivity can be used as an indicator of general soil nutrient levels.

The higher the conductivity and the concentration of salts, and the lower the conductivity, the easier it is to fertilize the soil. For this reason, it is necessary to analyse how electrical conductivity can affect substances in the soil.

During the determinations in the present study, the electrical conductivity of the soil was determined with the HACH portable Multiparameter.

According to the Commission Decision (EU) 2015/2099 of November 18, 2015, establishing the ecological criteria for the award of the EU Ecolabel for growing media, soil improvers and mulches, the electrical conductivity of the finished product must be less than 1000 µS/cm.

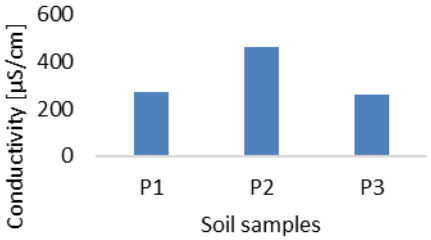

***Fig. 2.** Results obtained following the determination of soil conductivity*

In the attached chart in Figure 2, it can be seen that sample 2 has the highest electrical conductivity (465 µS/cm) and the other two soil samples have close values of electrical conductivity. None of the analysed soil samples exceeds the maximum value allowed by law.

Determining the soil's acidity

Hydrolytic acidity (A_h) is revealed by treating the soil with an alkali-hydrolysing salt (consisting of a strong base and a weak acid), which removes more adsorbed hydrogen or other acidic ions.

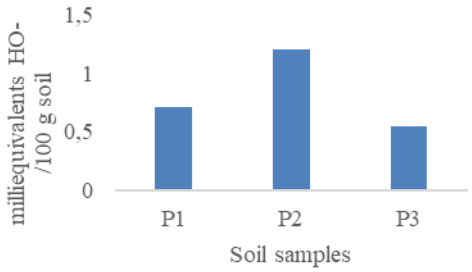

***Fig. 3.** Results obtained following the determination of soil acidity*

As can be seen from the above chart, the soil sample with the highest acidity is sample 2, followed by sample 1, and the lowest value was obtained from the soil sample taken from the garden (sample 3).

Hydrolytic acidity is the parameter that really indicates the quality of soil. When analysing soil, a number of parameters can fluctuate depending on the moisture level, but hydrolytic acidity is a constant that indicates the physical and chemical state of the soil at any given time. Experts have explained that a hydrolytic acidity level between 0 and 1 indicates soil with a good pH.

Determining the soil's total alkalinity

The alkaline reaction of the soil solution is determined by the composition of different compounds in the soil: carbonates in alkaline and alkaline-earth bicarbonates, sodium silicates, sodium humates, etc. Soil alkalinity can be natural or caused by human activity. Natural alkalinity is the result of the release of Na_2CO_3 from the soil by watering the soil, while artificial alkalinity, caused by human activities, is due to the application of fertilizers and irrigation water with high $NaHCO_3$ content [1].

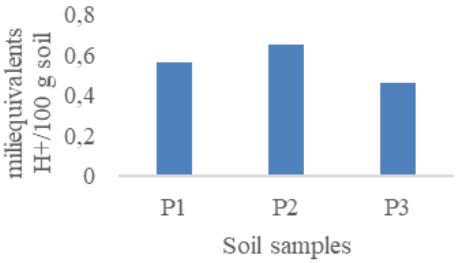

***Fig. 4.** Results obtained following the determination of soil alkalinity*

The chart presented in Figure 4 shows that the soil sample with the highest alkalinity is sample 2, with alkalinity of 0.651 milli equivalents H^+/100 g soil followed by the other samples with similar values. All analysed soil samples are weak in alkaline.

THE ANNALS OF "DUNAREA DE JOS" UNIVERSITY OF GALATI
FASCICLE IX. METALLURGY AND MATERIALS SCIENCE
Nº. 4 - 2024, ISSN 2668-4748; e-ISSN 2668-4756
Article DOI: https://doi.org/10.35219/mms.2024.4.03

Determining the calcium and magnesium cation content

The soil solution contains mineral, organic, and organo-mineral combinations. The mineral compounds consist of salts of mineral acids (carbonates, bicarbonates, ammonium, nitrates, nitrites, chlorides, sulphates, phosphates of Ca, Mg, Na, K, etc.) and various acids of Fe, Al, Mn. Organo-mineral combinations with different degrees of solubility are formed by combining humic acids with other types of organic acids with basic ions, represented by Ca^{2+}, Mg^{2+}, Na^{+}, K^{+}, etc. Calcium and magnesium cations in the soil are intended to improve the physical, chemical, and biological characteristics of the soil, correct over-acidification, and reduce soil depletion. Ca and Mg salts help restore soil structure [1].

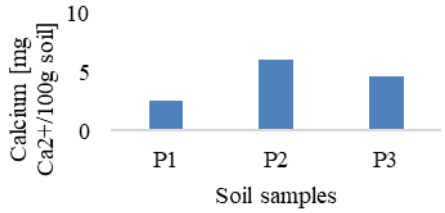

***Fig. 5.** Results obtained following the determination of calcium content*

The importance of calcium in soil is essential for healthy crops, especially if you grow vegetables. Calcium regulates the acid balance, but if the macronutrient is not sufficient, the concentration of acid in the soil starts to increase, disrupting root nutrition.

From the data presented in Figure 5, we can observe a difference between the soil sample from the field (sample 1) with the lowest value (2.52 mg Ca^{2+}/100 g sol) and soil sample 2 which has the highest value for calcium content (6.048 mg Ca^{2+}/100 g sol). The garden sample (soil sample 3) has a medium calcium content comparing the two extreme values.

The signs of a calcium deficiency in the soil are visible in crop plants: stunted growth, chlorosis, brown leaf tips, and spots. These tell you when the soil is suffering from a lack of calcium and when to intervene to lower the soil pH level when the soil has become too acidic.

The graph represented in Figure 6 shows a low magnesium content obtained in the garden soil sample (sample 3), the highest value for soil magnesium content was obtained for sample 2, 14.7 mg Mg^{2+}/100 g soil.

The main symptom of magnesium deficiency in plants is interveinal chlorosis. Interveinal chlorosis occurs when a yellow discoloration, sometimes accompanied by a reddish-brown colour appears between the leaf veins. The veins themselves remain green. The key to identify a magnesium deficiency is the localization of this chlorosis, as it can be mistaken for iron deficiency.

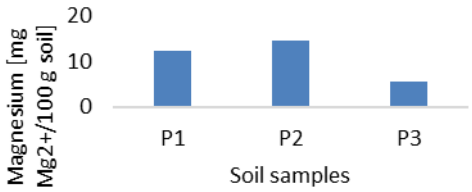

***Fig. 6.** Results obtained following the determination of magnesium content*

Determining the total nitrogen in soils

Nitrogen is one of the major elements necessary for life. It will simulate above-ground growth and produce the rich green colour that is characteristic of healthy plants, which is why nitrogen is essential for the plant's life. 78% of the atmosphere is covered by molecular nitrogen (N_2); Total nitrogen determination was carried out using a UV-VIS DR 5000 spectrophotometer with special standard solutions to identify the total nitrogen content in the soil.

Figure 7 shows the spectrophotometer used in some of the analyses carried out for this study.

***Fig. 7.** Spectrophotometer HACH LANGE DR5000*

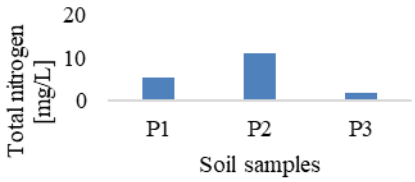

***Fig. 8.** Results obtained following the determination of total nitrogen*

From the graph presented in Figure 8, we observe that the highest total nitrogen content was obtained in soil sample 2, followed by the field soil

THE ANNALS OF "DUNAREA DE JOS" UNIVERSITY OF GALATI
FASCICLE IX. METALLURGY AND MATERIALS SCIENCE
Nº. 4 - 2024, ISSN 2668-4748; e-ISSN 2668-4756
Article DOI: https://doi.org/10.35219/mms.2024.4.03

sample (sample 1) and the lowest total nitrogen content in soil was obtained for the garden soil sample (sample 3).

Determining the aluminium content in the soil

The determination of the aluminium content in the aqueous soil extract was carried out using the UV-VIS DR 5000 spectrophotometer at a wavelength of 620 nm.

Fig. 9. *Aluminium determination kit*

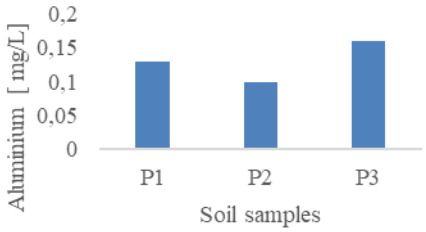

Fig. 10. *Results obtained following the determination of aluminium*

According to the above graph, the highest amount of aluminium was found in the garden soil sample (sample 3), i.e. 0.16 mg/L, followed by the field sample with a close value of 0.13 mg/L, and the lowest amount of aluminium was found in sample 2, i.e. 0.10 mg/L.

Soil aluminium test results provide suggestions for correcting soil toxicity, one of the best ways to correct soil toxicity is agricultural lime.

Determination of phosphates

Phosphates are found in the soil as easily soluble primary phosphates and as secondary phosphates, tertiary, ortho-alkalcic phosphates, phosphates adsorbed on the surface of iron and aluminium oxides, or clay, which are poorly soluble.

The determination of phosphates in the aqueous soil extract was carried out by spectrophotometer and had the following steps: the foil from the cap of the bottle was removed with the standard solution, 2 mL of the sample was pipetted to be analysed, then the cap with the inner part was put to mix with the substance in the stopper and vigorously shook; then heated in a thermostat for one hour at 100 °C; the vial was allowed to cool to room temperature, then shook rigorously several times, then added 0.2 mL of reagent B, stirred several times and inserted into the spectrophotometer for reading the result.

Fig. 11. *Phosphate determination kit*

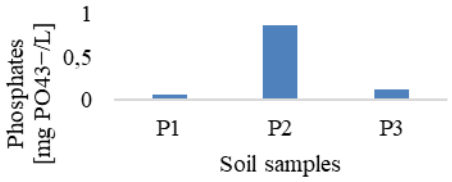

Fig. 12. *Results obtained following the determination of phosphates*

As can be seen in the graph above, the highest number of phosphates was detected in sample 2 with a value of 0.87 mg PO_4^{3-}/L, the other two samples being close in terms of values, the lowest being for sample 1 with 0.058 mg PO_4^{3-}/L.

According to studies, the factors influencing phosphorus retention in soils are: soil pH, soil texture and structure (clay-rich soils contain high amounts of phosphorus), iron, aluminium, calcium, and magnesium content, soil moisture and temperature.

Determination of iron

To determine the iron content in the sample to be analysed, it was proceeded as follows: 2 mL of the aqueous extract sample was pipetted into a vial containing the standard solution, then the vial was closed and homogenized the content. After a 5-minute pause, it was shaken a few more times, then the vial was placed in the spectrophotometer cuvette to determine the iron content.

The graph presented in Figure 13 shows that the highest value for iron content is obtained for soil sample 2 with a value of 0.895 mg Fe^{2+}/Fe^{3+}/L, the lowest value being identified in soil sample 3 from the garden, i.e. 0.489 mg Fe^{2+}/Fe^{3+}/L.

In iron excess, the leaves are initially covered with browning spots which with time turn a uniform

THE ANNALS OF "DUNAREA DE JOS" UNIVERSITY OF GALATI
FASCICLE IX. METALLURGY AND MATERIALS SCIENCE
Nº. 4 - 2024, ISSN 2668-4748; e-ISSN 2668-4756
Article DOI: https://doi.org/10.35219/mms.2024.4.03

brown colour. Excess iron occurs on acid soils and excess moisture, where the soluble Fe content can increase from 0.1 to 50-100 ppm in only a few weeks.

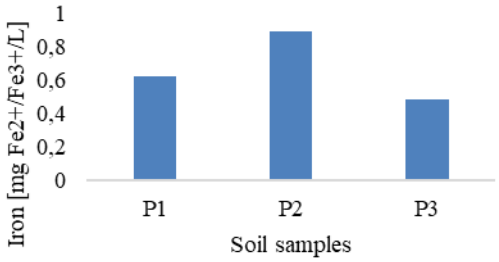

Fig. 13. *Results obtained after determining the iron content*

Determining heavy metals in the soil

Heavy metals fall into two categories: essential and non-essential.

Essential metals (micronutrients) are: chromium, cobalt, copper, manganese, molybdenum, iron, selenium, and zinc, which are necessary for the optimal functioning of biological and biochemical processes in the body.

Non-essential metals such as arsenic, cadmium, mercury, and lead have no known biological function.

The determination of the amounts of metals was carried out using the X-ray fluorescence spectrometer. X-ray fluorescence spectroscopy (XRF) measures the characteristic X-rays emitted from a sample after it is bombarded with high-energy radiation.

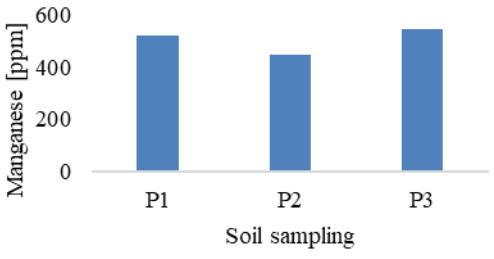

Fig. 14. *Results obtained following the determination of manganese content*

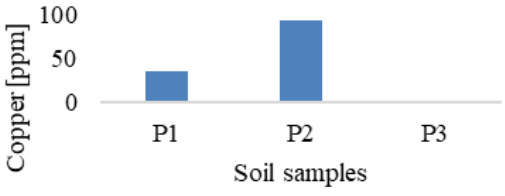

Fig. 15. *Results obtained following the determination of copper content*

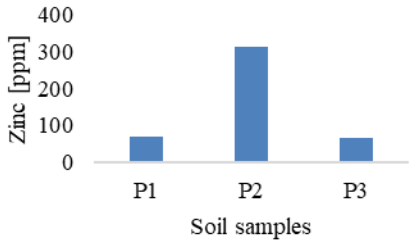

Fig. 16. *Results obtained following the determination of zinc content*

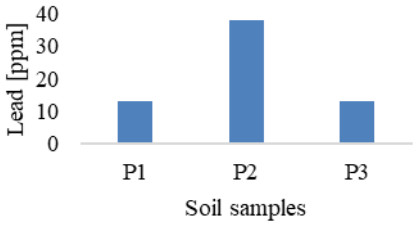

Fig. 17. *Results obtained following the determination of lead content*

From the data presented in Figures 14-17, the following can be observed:

The amount of manganese is relatively equal for all analysed soil samples, around 450 ppm, which means that it is within the values required by the legislation, the normal values being 900 mg/kg dry soil.

Concerning the amount of copper in the analysed soil samples, it was detected only in two of the three samples, i.e. sample 2 and sample 1, values above the normal value were detected, respectively 36 ppm and 94 ppm, the threshold of the normal value being 20 mg/kg, but below the alert threshold, which is 100 mg/kg dry soil.

Zinc is found in all analysed soil samples with values close to each other for the garden and field samples, around 70 ppm, but a higher value was obtained for sample 2, i.e. 312 ppm slightly above the alert threshold (AT alert threshold – 300 mg/kg dry soil).

As in the municipality of Bârlad, the nearby area where the zinc concentration exceeds the alert threshold is an industrial zone, it is possible that this is one of the determining factors of zinc concentrations above the alert threshold value.

The concentration of lead in the reference areas is approximately the same for the garden and field samples, i.e. around 13 ppm, but for soil sample 2 a higher value of 38 ppm was detected, above the normal value (20 mg/kg dry soil) but still below the alert threshold (50 mg/kg dry soil).

3. Conclusions

Soil is a complex environmental factor without which life on Earth would not be possible. Due to the constituents that are often found in soil (mineral and organic matter, air, water, and micro-organisms) and with the help of which soil fulfils certain functions such as water purification, nutrient recycling and gas exchange with the atmosphere. Since the soils analysed in this article do not have an ideal composition, changes in the content of soil phases will influence the physical, chemical, and biological properties of the soil.

The study of the soil in the sampling areas consists of laboratory analysis in order to determine the soil quality. The soil has been analysed in terms of physico-chemical parameters by the following determinations: pH, conductivity, acidity, alkalinity, total nitrogen, aluminium, phosphates, iron, heavy metals, calcium, and magnesium content in the soil.

The results obtained from the soil pH determination – show that all samples have a pH close to neutral to weakly alkaline with values between 7-7.4 pH units.

Determination of soil alkalinity – the highest alkalinity was obtained for soil sample 2 with an alkalinity of 0.651 milli equivalents H^+/100 g soil, followed by the other two samples with values close to each other. All analysed soil samples are weakly alkaline.

Soil acidity determination – the highest soil acidity value was obtained for soil sample 2, followed by soil sample 1, and the lowest value was obtained from soil sample 3.

Determination of heavy metals content in soil – regarding the amount of copper in the analysed soil samples, values above the normal value were detected, i.e. 36 ppm in soil sample 1 and 94 ppm in soil sample 2, the threshold of normal value was 20 mg/kg, but below the alert threshold.

Zinc is found in all analysed soil samples with values close to each other for the garden and field samples, around 70 ppm, but a higher value was obtained for soil sample 2, i.e. 312 ppm slightly above the alert threshold.

References

[1]. Blaga Ghe., Filipov F., Rusu I., Udrescu S., Vasile D., Pedologie, Ed. AcademicPres, 2005.
[2]. Mureșan A. C., *Chimia și poluarea solului*, Editura Universității "Dunărea de Jos" Galați, 2018.
[3]. Rajendra Prasad, James F. Power., *Soil fertility management for sustainable agriculture*, ISBN 1-56670-254-2, Boca Raton, CRC Press, doi.org/10.1201/9780367803063, 1997.
[4]. Ministerul Agriculturii și Dezvoltării Rurale, *Strategia pentru dezvoltarea sectorului agroalimentar pe termen mediu și lung orizont 2020-2030*, București, 2015.
[5]. Malik A. A., *et al.*, *Land use driven change in soil pH affects microbial carbon cycling processes*, Nat Commun, 9(1), 3591, doi: 10.1038/s41467-018-05980-1, 2018.
[6]. Yan L., *et al.*, *The aluminum tolerance and detoxification mechanisms in plants; recent advances and prospects*, Crit. Rev. Environ. Sci. Technol. 52, p. 1491-1527, https://doi.org/10.1080/10643389.2020.1859306, 2022.
[7]. Lehmann J., Kleber M., *The Contentious Nature of Soil Organic Matter*, Nature, 528, p. 60-68. https://doi.org/10.1038/nature16069, 2015.
[8]. Theresa Merl, *et al.*, *Measuring soil pH at in situ like conditions using optical pH sensors (pH-optodes)*, Soil Biology and Biochemistry, 175, 108862, 10.1016/j.soilbio.2022.108862, 2022.
[9]. Fierer N., Jackson R. B., *The diversity and biogeography of soil bacterial communities*, Proceedings of the National Academy of Sciences of the United States of America, 103, p. 626-631, https://doi.org/10.1073/pnas.0507535103, 2006.
[10]. Rousk J., *et al.*, *Soil bacterial and fungal communities across a pH gradient in an arable soil*, The ISME Journal, 4 (10), p. 1340-1351, https://doi.org/10.1038/ismej.2010.58, 2010.
[11]. Cao H., *et al.*, *Soil pH, total phosphorus, climate and distance are the major factors influencing microbial activity at a regional spatial scale*, Scientific Reports 6, p. 1-10, https://doi.org/10.1038/srep25815, 2016.
[12]. Slessarev E. W., *et al.*, *Water balance creates a threshold in soil pH at the global scale*, Nature 540, p. 567-569, https://doi.org/10.1038/nature20139, 2016.
[13]. Yu Shi, *et al.*, *Threshold effects of soil pH on microbial co-occurrence structure in acidic and alkaline arable lands*, Science of the Total Environment, 800, 149592, 10.1016/j.scitotenv.2021.149592, 2021.
[14]. Hadi Pirasteh-Anosheh, *et al.*, *Relationship between soil salinity and alkalinity with Alhagi camelorum growth in hypersaline and hyperarid environments*, Journal of Arid Environments, 206, 104830, 10.1016/j.jaridenv.2022.104830, 2022.
[15]. Haixia Zhao, *et al.*, *Physicochemical properties and salinization characteristics of soils in coastal land reclamation areas: A case study of China-Singapore Tianjin Eco-City*, Heliyon, 8, e12629, DOI:10.1016/j.heliyon.2022.e12629, 2023.

THE ANNALS OF "DUNAREA DE JOS" UNIVERSITY OF GALATI
FASCICLE IX. METALLURGY AND MATERIALS SCIENCE
Nº. 4 - 2024, ISSN 2668-4748; e-ISSN 2668-4756
Article DOI: https://doi.org/10.35219/mms.2024.4.04

RESEARCH ON NANOSTRUCTURED HYBRID MATERIALS FOR SENSING DOPAMINE BY CYCLIC VOLTAMMETRY

Elena Emanuela HERBEI, Viorica GHISMAN, Nicoleta BOGATU, Alina-Crina MUREȘAN, Iuliana-Raluca URSACHE, Daniela-Laura BURUIANĂ

Interdisciplinary Research Centre in the Field of Eco-Nano Technology and Advance Materials CC-ITI,Faculty of Engineering, "Dunarea de Jos" University of Galati, 47 Domnească, 800008 Galati, Romania
e-mail: elena.herbei@ugal.ro

ABSTRACT

In this research, we present chemical method of obtaining hybrid nanostructured particles used to modify the screen-printed carbon electrode to detect the redox activity of dopamine. Dopamine (DA) is a neurotransmitter that plays a very important role in the functioning of mammalian systems (central nervous, hormonal, renal, and cardiovascular), and its deficiency results in the development of diseases (Parkinson's and Alzheimer's, restless legs syndrome, or schizophrenia). Magnetite and titanium oxide nanoparticles were functionalized by chemical reaction to be used to modify SPCE. The chemical method used to modify the nanoparticles was a sol-gel chemical reaction. The hybrid materials were analyzed by scanning electron microscopy (SEM/EDX) and by cyclic voltammetry (CV). The alcoholic solution based on magnetite-Fe_3O_4 (F1) and magnetite/titania-TiO_2 (F2) was used is order to be dropped cast onto SPCE surface. The modified SPCE was measured at 0.1 V/s by cyclic voltammetry. The cyclic voltammetry was conducted using a Potentiostat/galvanostat multichannel electrochemical device from OrigaLys, France, OrigaFlex model OGF+01A. Optical microscopy (OM) analyzed the modified surface of screen-printed electrodes. The TiO_2 was characterized through field emission scanning electron microscopy (FE-SEM) with EDX elemental analysis.The modified carbon electrode shows the different waveforms of the voltage applied to the working electrode depending on chemical composition of modified electrodes. The constructed sensor exhibited acceptable selectivity, but not good stability and needs more improvements of chemical composition to provide selectivity, reproducibility, and stability for repeated measurements. The CV curves show very low oxidation and reduction activity due to the unstable contact between the electrode and nanoparticles.

KEYWORDS: hybrid materials, nanostructure, cyclic voltammetry

1. Introduction

The demand for new and hybrid materials or materials with new properties is currently high. The physico-chemical modification of their surface can improve the performance of the sensors (electrochemical). For this purpose, artificial components (hybrid nanostructures, polymer films, nanoparticles), biological (enzymes), or their combination can be used. By chemically modifying the surface of the electrochemical sensor, with thin and nanostructured films or by self-assembling monolayers, its performance can be improved by: facilitating the transfer of electrons selective accumulation or diffusion of analytes the possibility of identifying substances that do not have electroactive properties. Screen-printed electrodes (SPEs) offer some advantages over traditional electrodes in the areas of cost, solution volume, and operating temperature [1]. The primary use of cyclic voltammetry is for the creation of biosensors, not for target analytes to be determined, as it is a widely used electrochemical technique. By using this technique, it is possible to evaluate the redox behavior of species

THE ANNALS OF "DUNAREA DE JOS" UNIVERSITY OF GALATI
FASCICLE IX. METALLURGY AND MATERIALS SCIENCE
Nº. 4 - 2024, ISSN 2668-4748; e-ISSN 2668-4756
Article DOI: https://doi.org/10.35219/mms.2024.4.04

that are present both in solution and sorbed to the electrode [2].

In their work, Keerthi *et al.* [3] were able to synthesize a core-shell hybrid nanomaterial of Mo NPs@f-MWCNTs using acid condensation and use it, to detect DA for the first time electrochemically. The interaction of positively charged Mo NPs on the surface of MWCNT through strong electrostatic interactions involves anchor sites for the interaction of negatively charged oxygen functional groups on the MWCNT. Cheng *et al.* [4] proposes to modify bare electrodes with hybrids made of highly purified AuNBPs and MWCNTs, which are used to enhance the selectivity and sensitivity of the electrochemical sensor, detecting DA in the presence of Ascorbic Acid and Uric Acid.

Other researchers used ZnO/CuO to modify SPCE [5], the nanocomposite of ZnO/CuO is grown on the gold-coated glass substrate by hydrothermal growth technique in two steps and the hybrid material is used for the selective determination of dopamine by cyclic voltammetric and amperometric techniques. The response was found linear for the concentration of 10^{-3} M to 8.0 mM dopamine. The sensitivity of 90.9 μAmM^{-1} cm^{-2} and a detection limit of 1.0×10^{-4} mM were also observed for the presented dopamine sensor. There are also carbon nano coils and copper tetra(p-methoxyphenyl) porphyrin nanocomposite used for electrochemical detection of dopamine [6]. The electroanalytical performances of SPCE/rGO/Ru complex/RuO_2 and SPCE/rGO/RuO_2 to individually and simultaneously detect dopamine and uric acid were estimated by differential pulse voltammetry method (DPV) At room temperature, the developed modified sensor's stability towards 10 µM of DA was tested for nine days [7]. An eco-friendly carbon paste electrode (BHA/rGO/CPE), crafted from an innovative hydroxyapatite/reduced graphene oxide hybrid, is used to detect dopamine (DA). Eggshells, sourced from environmental bio-waste, were utilized to produce hydroxyapatite (BHA) in this experiment [8].

Hybrid materials have been developed to meet certain new performance requirements.

Modification of surface solid supports is one of the most common methods for enhancing the sensitivity and selectivity of electroanalytic compounds involved in physiological processes. Various fields of materials science can benefit from the use of inorganic-organic hybrids due to their simple processing and molecular design capabilities. This work reports the preparation of hybrid materials based on magnetite-Fe_3O_4 and magnetite/titania-TiO_2 for SPCE surface modification to be used in dopamine detection. We measured a buffer solution with 0.1 µM dopamine solution to observe the redox activity.

2. Experimental

Reagents: All chemicals are of analytical grade and used without any further purification and proceeded from Sigma Aldrich, TiO_2 nano-powder, <100 nm particle size, 99.5% trace metals basis, and magnetite was prepared by coprecipitation method.

Preparation of sols and experimental method: Sols based on magnetite and titania were prepared using an alcoholic solvent and functionalized agent (3-(trimethoxysilyl) propyl methacrylate) and were obtained by mixing the magnetite and titania with (3-(trimethoxysilyl) propyl methacrylate 1:1 molar ratio under vigorous agitation at 60 ºC tantalum in an alcoholic solvent. Screen-printed carbon electrodes (SPCEs) from the Methrom Drop Sens model C110, measuring L33 × W10 × H0.5 mm, were used. The modified working electrode (WE) was carbon-based with a 4 mm diameter, the auxiliary electrode (AE) was made of carbon, and the reference electrode (RE) was composed of silver. A 1 µL sol of nanohybrid suspension was drop-cast onto the SPCE's working electrode surface and air-dried at room temperature.

3. Results and discussion

3.1. SEM analysis

The SEM images (Figure 1) show a non-homogenous, discontinuous aspect regarding the distribution of particles, a high roughness. The magnetite particles are of different sizes, not uniform (Fig. 1. a, b), covered with maghemite spherules probably due to incomplete oxidation of magnetite (Fig. 2. a, b) but also coated with titanium oxide in the form of symmetrical flowers (Fig. 3. a, b).

The top view of magnetite samples F1 to F2 indicates generally the agglomeration of magnetite and also the coated magnetite with titania. In F1 and F2 SEM images, we observe irregularly agglomerated forms of magnetite with dimensions varying from hundreds of nanometres to microns. Also, here we observe different morphologies such as spheres and flowers.

THE ANNALS OF "DUNAREA DE JOS" UNIVERSITY OF GALATI
FASCICLE IX. METALLURGY AND MATERIALS SCIENCE
Nº. 4 - 2024, ISSN 2668-4748; e-ISSN 2668-4756
Article DOI: https://doi.org/10.35219/mms.2024.4.04

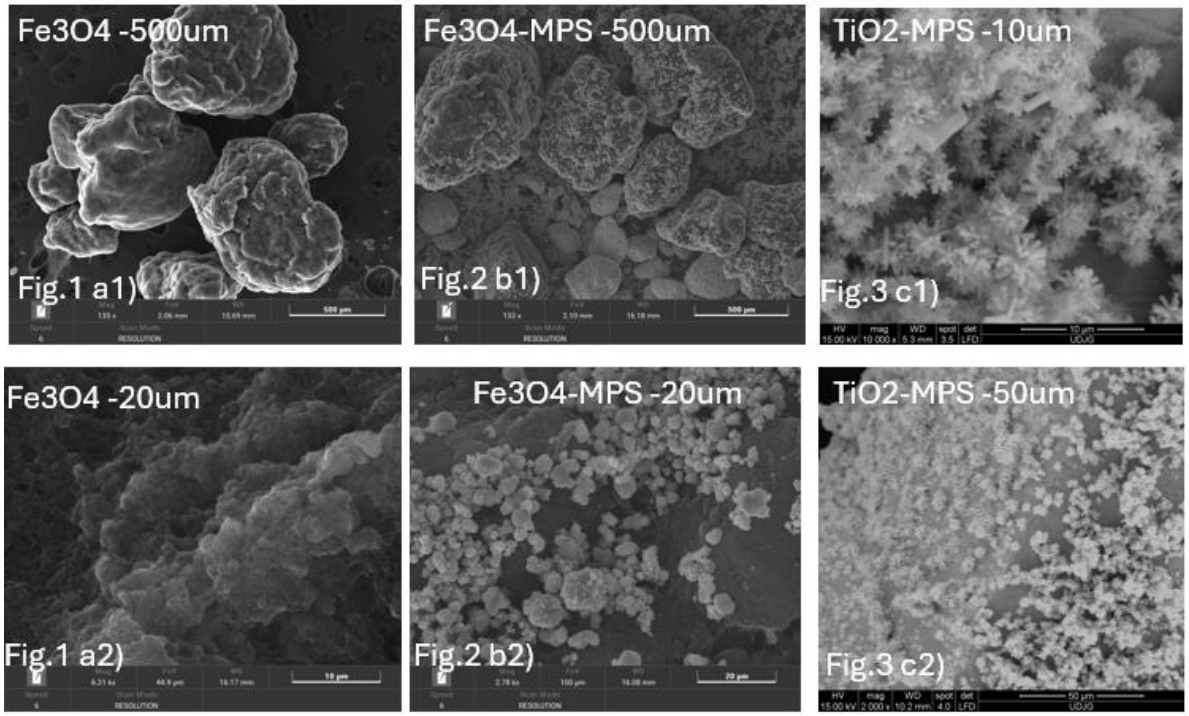

Fig. 1. *Top view (a) SEM images of Fe_3O_4 (a1-500 um, a2-20 um), (b) of Fe_3O_4-MPS (b1-500 um, b2-20 um), (c), Fe_3O_4/TiO_2-MPS (c1-10 um, c2-50 um)*

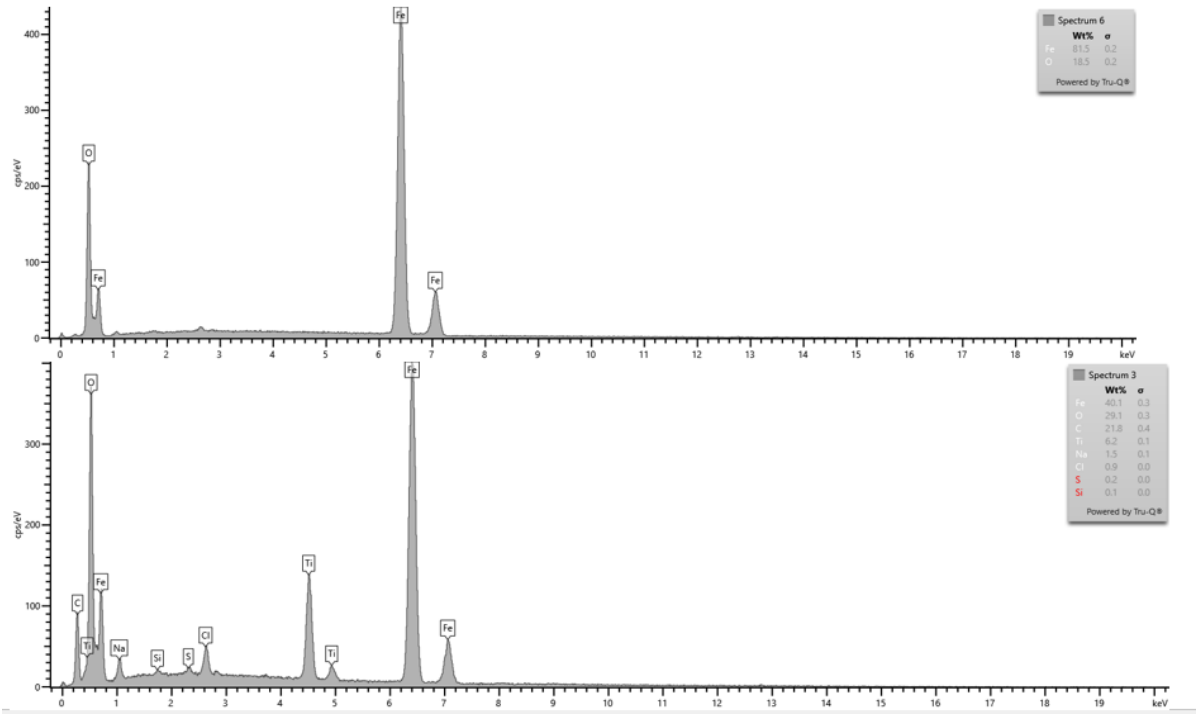

Fig. 2. *EDX of Fe_3O_4 and Fe_3O_4/TiO_2*

THE ANNALS OF "DUNAREA DE JOS" UNIVERSITY OF GALATI
FASCICLE IX. METALLURGY AND MATERIALS SCIENCE
Nº. 4 - 2024, ISSN 2668-4748; e-ISSN 2668-4756
Article DOI: https://doi.org/10.35219/mms.2024.4.04

Table 1. *Results from EDX element composition (%)*

Sample code	T (°C)	Elemental percent from EDX analysis (%)			pH
		Fe	O	Ti	
F1	T = 96	56.2	31.23	8.7	11-12
F2	T = 96	81.5	18.5	-	11-12

3.2. Cyclic voltammetry for the modified SPCE with magnetite and titania hybrid materials

The potential graph assessing the electrochemical stability of electrolytes is crucial for identifying oxidation and reduction potentials. The study focused on evaluating the electrochemical behavior to observe the effects of surface-modified SPCEs in a standard redox analyte. Initially, the experiment involved measuring the unmodified SPCE in a buffer and dopamine solution to activate necessary parameters. The electrochemical signal was recorded at a 0.1 V/s scan rate across five cycles to stabilize the electrode, depicted by the blue curves in Figure 3. These voltammograms revealed irregular anodic and cathodic peaks throughout the five cycles.

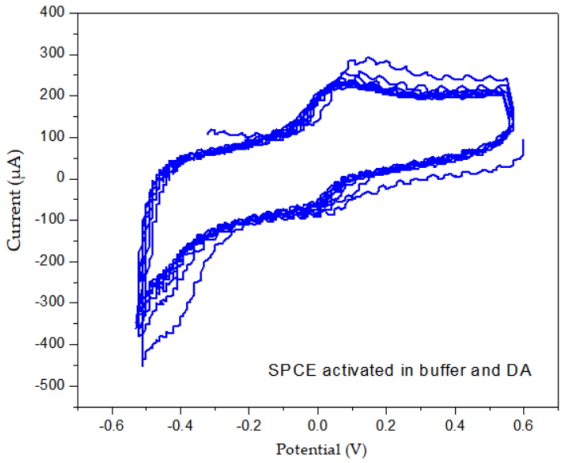

Fig. 3. *Cyclic voltammograms for unmodified SPCE in buffer and DA solution*

After this measurement, we conducted the CVs for the modified SPCE with Fe_3O_4-MPS (Figure 4) and Fe_3O_4/TiO_2-MPS (Figure 5) in buffer and the 1 µM dopamine solution. The scan rates for all the measurements were 0.1V/s. The measurements were done for 5 times for each electrode to observe modification of redox activity. In the case of electrode modified with magnetite the oxidation and reduction peaks are very decreased almost similar with the measurements for the unmodified SPCE. This can be assumed to the morphology of the magnetite grains.

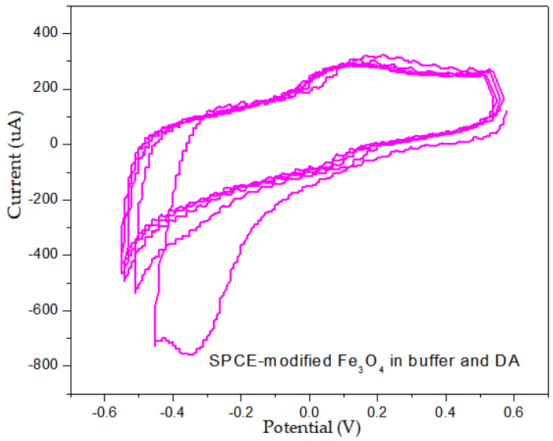

Fig. 4. *Cyclic voltammograms for Fe_3O_4 modified SPCE in buffer and DA solution*

For the samples Fe_3O_4/TiO_2-MPS the voltammograms showed lower oxidation and reduction activity for all the measurements. Probably the presence of TiO_2 on the magnetite surface increased the electron transfer from the solution.

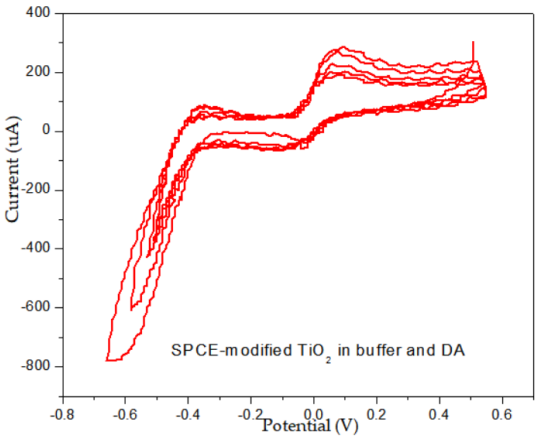

Fig. 5. *Cyclic voltammograms for Fe_3O_4/TiO_2 modified SPCE in buffer and DA solution*

4. Conclusions

In this work, we prepared 2 hybrid alcoholic sols based on magnetite and magnetite/titania to modify the screen-printed carbon electrode to observe the redox activity of dopamine of 1 µL concentration. The SEM/EDX images showed a non-homogenous, discontinuous aspect regarding the distribution of particles, a high roughness surface. The magnetite particles are of different sizes, not uniform covered with maghemite spherules probably due to incomplete oxidation of magnetite and also coated with titanium oxide in the form of symmetrical flowers. The dimension of magetite is varying from few hundred of nanometres to microns agglomeration particles. The voltammograms showed lower to minimum oxidation and reduction activity for the samples based on magnetite. In the case of magnetite /titania modified SPCE the presence of TiO_2 on the magnetite surface increased the electron transfer from the solution and the redox activity was increased.

Funding

"This research was funded by "Support and development of CDI-TT activities in the "Dunărea de Jos" University of Galați - Internal grant RF2473/ 31.05.2024 - title project „Materiale hibride nanostructurate utilizate în structura unor senzori modificați pentru identificarea dopaminei MH-SPCED (Acronim MH-SPCED)".

References

[1]. Reducks D., *et al.*, *Screen-Printed Electrode Information*, Pine Res. Instrum., vol. 10036, p. 1-10, 2019.
[2]. Banerjee S., *et al.*, *Electrochemical Detection of Neurotransmitters*, Biosensors, vol. 10, no. 8, doi: 10.3390/bios10080101, 2020.
[3]. Keerthi M., *et al.*, *A core-shell molybdenum nanoparticles entrapped f-MWCNTs hybrid nanostructured material based non-enzymatic biosensor for electrochemical detection of dopamine neurotransmitter in biological samples*, Sci. Rep., vol. 9, no. 1, p. 1-12, doi: 10.1038/s41598-019-48999-0, 2019.
[4]. Cheng J., *et al.*, *A novel electrochemical sensing platform for detection of dopamine based on gold nanobipyramid/multi-walled carbon nanotube hybrids*, Anal. Bioanal. Chem., vol. 412, no. 11, p. 2433-2441, doi: 10.1007/s00216-020-02455-5, 2020.
[5]. Khun K., *et al.*, *An electrochemical dopamine sensor based on the ZnO/CuO Nanohybrid structures*, J. Nanosci. Nanotechnol., vol. 14, no. 9, p. 6646-6652, doi: 10.1166/jnn.2014.9367, 2014.
[6]. Aqsa Batool Bukhari S., *et al.*, *Efficient electrochemical detection of dopamine with carbon nanocoils and copper tetra(p-methoxyphenyl)porphyrin nanocomposite*, Arab. J. Chem., vol. 15, no. 12, p. 104375, doi: 10.1016/j.arabjc.2022.104375, 2022.
[7]. Guerniche D., *et al.*, *Novel hybrid material based on Ru complex and its RuO2 oxide for dopamine and dopamine-uric acid simultaneous determination*, J. Organomet. Chem., vol. 997, p. 122769, doi: 10.1016/j.jorganchem.2023.122769, 2023.
[8]. Gopal T. V., *et al.*, *Eco-friendly and bio-waste based hydroxyapatite/reduced graphene oxide hybrid material for synergic electrocatalytic detection of dopamine and study of its simultaneous performance with acetaminophen and uric acid*, Surfaces and Interfaces, vol. 24, no. October 2020, p. 101145, doi: 10.1016/j.surfin.2021.101145, 2021.

THE ANNALS OF "DUNAREA DE JOS" UNIVERSITY OF GALATI
FASCICLE IX. METALLURGY AND MATERIALS SCIENCE
Nº. 4 - 2024, ISSN 2668-4748; e-ISSN 2668-4756
Article DOI: https://doi.org/10.35219/mms.2024.4.05

RESEARCH ON THE INFLUENCE OF CLEANING PRODUCTS ON THE QUALITY OF OPTICAL LENS SURFACES

Beatrice Daniela TUDOR, Iustina BĂBUȘANU
"Dunarea de Jos" University of Galati, Romania
e-mail: beatrice.tudor@ugal.ro

ABSTRACT

The paper presents research on the evaluation of the influence of maintenance products, such as cleaning solutions, on the quality of lenses. The research analysed the effects of these products on scratch resistance and image clarity. The eyeglass lenses were cleaned repeatedly with cleaning products, namely eyeglass wipes, liquid soap and dishwashing detergent. The results of this study are essential for knowing how to maintain these lenses, in order to preserve the properties and quality of the surfaces.

KEYWORDS: lenses, cleaning solutions, eyeglass

1. Introduction

The field of optical lens manufacturing is very vast and has great applicability in several engineering fields.

The development of modern technologies for manufacturing these optical lenses and the emergence of new materials with superior properties have led to the diversification of the fields in which these types of lenses find their application [1, 4].

Optical lenses are essential components of many optical devices, such as eyeglasses, cameras, telescopes, and microscopes. Lens manufacturing technology has developed significantly over the years, leading to improvements in precision, performance, and cost.

Lenses can be made from a variety of materials, including glass, plastic, and crystal. Each material has specific optical and mechanical properties that influence the performance and use of the lens.

A deeper understanding of how lens quality is affected by maintenance products can contribute to the development of more durable and efficient lenses that meet the needs of users in a more satisfactory way [2, 3].

2. Experimental research on the influence of maintenance products on the quality of optical lens surfaces

The research analysed the influence of cleaning products, namely eyeglass wipes, liquid soap and dishwashing detergent, on the quality of the lens surface.

The analysis was carried out on a set of lenses of different thicknesses and diopters, with and without protection, respectively:

- Lenses with medium protection with diopter -0.50 with 1.25 mm lens thickness.
- Lenses without protection with diopter -0.50 with a lens thickness of 1.20 mm.
- Lenses with medium protection with diopter -0.25 with 1.17 mm lens thickness.
- Lenses without protection with diopter -0.25 with a lens thickness of 1.15 mm.
- Sunglasses lens without diopters

To observe the influence of maintenance products on the quality of the lenses, a microscopic analysis of the lens surfaces was performed, and the PH of the solutions used for cleaning was determined, in order to analyse the degree of damage to the lens's protective layer and determine how they influence the quality of the surface [5].

To see the influence of the degree of acidity of the cleaning solutions on the quality of the lens surface, the PH of the solutions used for cleaning, namely liquid soap and dishwashing detergent, was determined. The analysis of the lens surfaces was done using an optical microscope, within the microscopy laboratory of the Faculty of Engineering.

The determination of the pH of liquid soap and dishwashing detergent is shown in Fig. 1.

The data obtained for the pH of cleaning solutions are presented in Table 1.

THE ANNALS OF "DUNAREA DE JOS" UNIVERSITY OF GALATI
FASCICLE IX. METALLURGY AND MATERIALS SCIENCE
N°. 4 - 2024, ISSN 2668-4748; e-ISSN 2668-4756
Article DOI: https://doi.org/10.35219/mms.2024.4.05

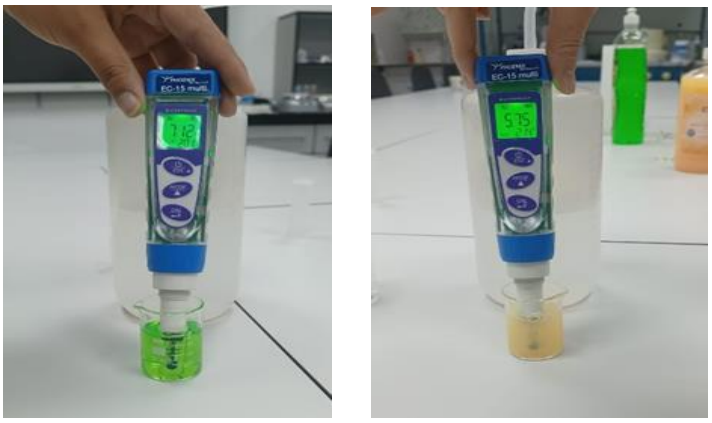

a b

Fig. 1. *Determination of the pH of cleaning solutions (a. dishwashing detergent, b. liquid hand soap)*

Table 1. *pH of cleaning solutions*

	Liquid dishwashing detergent		**Liquid hand soap**	
PH	7.12	20 °C	5.56	20 °C
Conductivity	-10.3 mW	63.3 mS	81.5 mW	56.2 mS
TSD (Total dissolved solids)	45.5 ppt		40.0 ppt	
Salinity	41.5 g/L		36.4 g/L	

The microscopic analysis of the lens surface was performed with the KERN optical microscope assembly, monitor and computer.

The powerful and adjustable 50W halogen unit ensures optimal illumination of the samples.

The technical data of the KERN optical microscope are:

- infinite optical system;
- 30° inclined viewing position;
- diopter compensation on both eyepieces;
- dimensions: L×W×H 747×271×379 mm;
- net weight approx. 12.968 kg.

The images obtained from microscopic analysis are shown in Fig. 3.

Following microscopic analysis, it can be seen that the quality of the lens surface is influenced by the protective layer, regardless of the diopter value.

Both at the lenses with diopters of -0.50 and in those with diopters of -0.25, a small deterioration of the lens surface is observed. At the lenses without protection, cleaned with hand soap, we observe surface deterioration.

For the lenses with diopters of -0.50 and -0.25 with and without protection, cleaned with dishwashing detergent, we obtained the following images shown in Fig. 4.

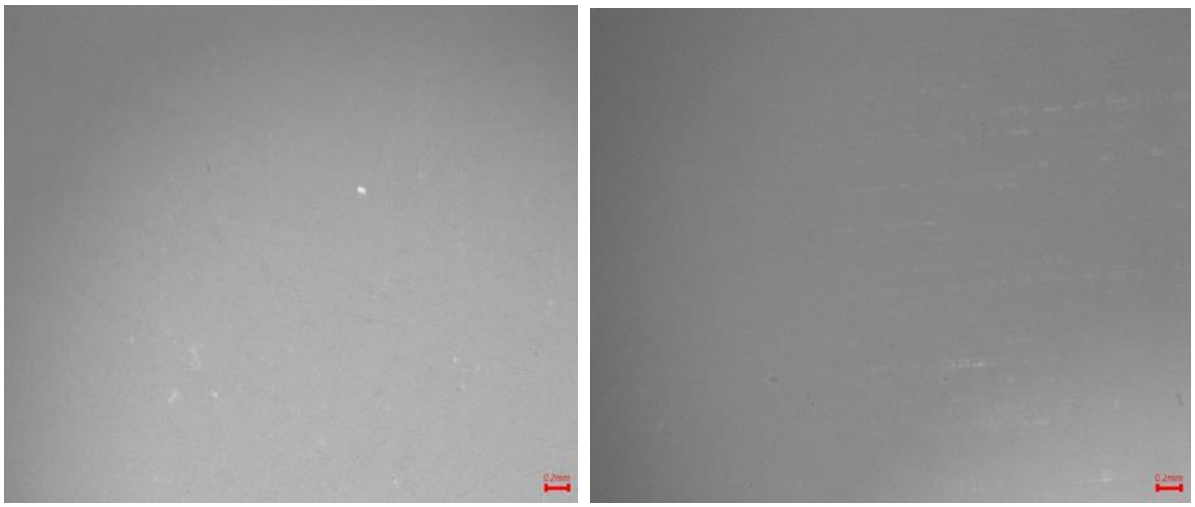

a. Lenses with medium protection with diopter -0.50 b. Lenses without protection with diopter -0.50

THE ANNALS OF "DUNAREA DE JOS" UNIVERSITY OF GALATI
FASCICLE IX. METALLURGY AND MATERIALS SCIENCE
Nº. 4 - 2024, ISSN 2668-4748; e-ISSN 2668-4756
Article DOI: https://doi.org/10.35219/mms.2024.4.05

c. Lenses with medium protection with diopter -0.25

d. Lenses without protection with diopter -0.25

Fig. 3. *Lenses with diopters of -0.50 and -0.25 with and without protection cleaned with liquid hand soap*

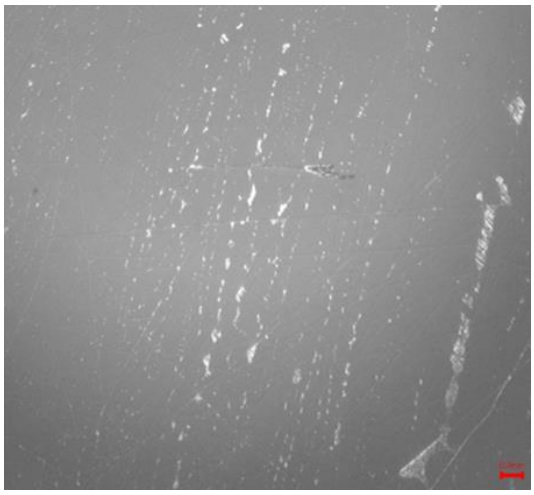

a. Lenses with medium protection with diopter -0.50

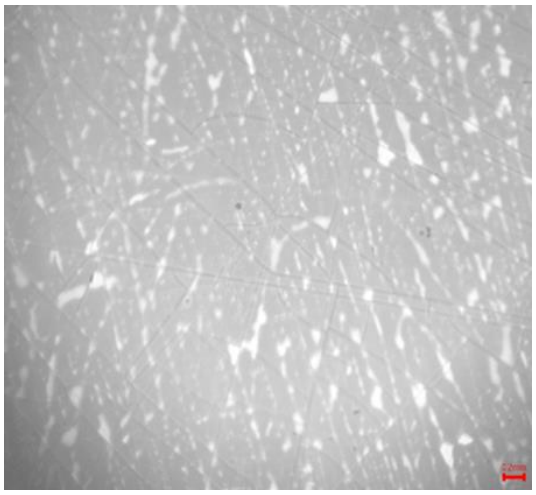

b. Lenses without protection with diopter -0.50

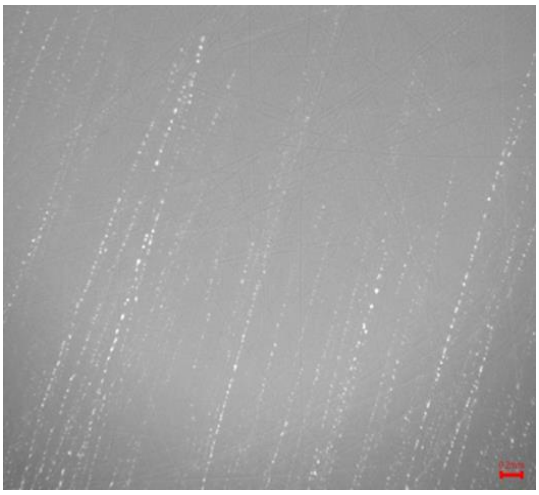

c. Lenses with medium protection with diopter -0.25

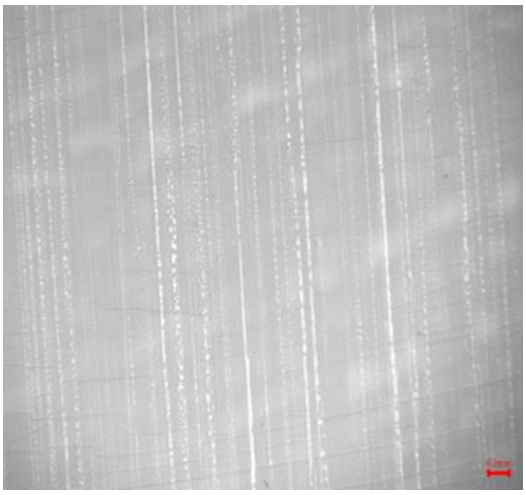

d. Lenses without protection with diopter -0.25

Fig. 4. *Lenses with diopters of -0.50 and -0.25 with and without protection cleaned with dishwashing detergent*

THE ANNALS OF "DUNAREA DE JOS" UNIVERSITY OF GALATI
FASCICLE IX. METALLURGY AND MATERIALS SCIENCE
Nº. 4 - 2024, ISSN 2668-4748; e-ISSN 2668-4756
Article DOI: https://doi.org/10.35219/mms.2024.4.05

For lenses cleaned with dishwashing detergent, we observed, as in the case of those cleaned with liquid soap, a more advanced deterioration of the surface quality of the lenses without protection.

The surface damage was greater for lenses cleaned with dishwashing detergent than for those cleaned with liquid soap, because dishwashing detergent has a higher pH, 7.12 compared to 5.56 for liquid soap.

For lenses with diopters of -0.50 and -0.25 with and without protection, cleaned with eyeglass wipes, we obtained the following images shown in Fig. 5.

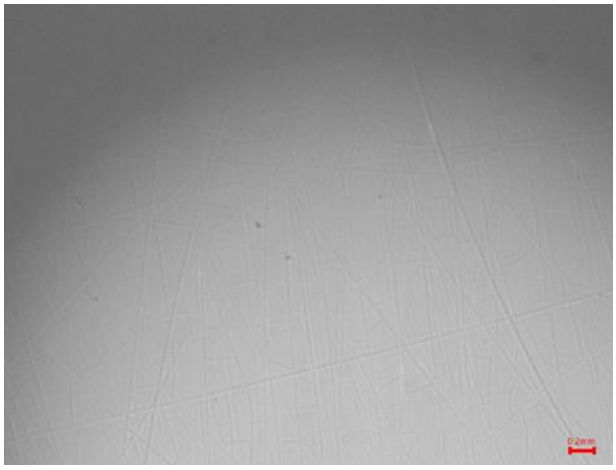

a. Lenses with medium protection with diopter -0.50

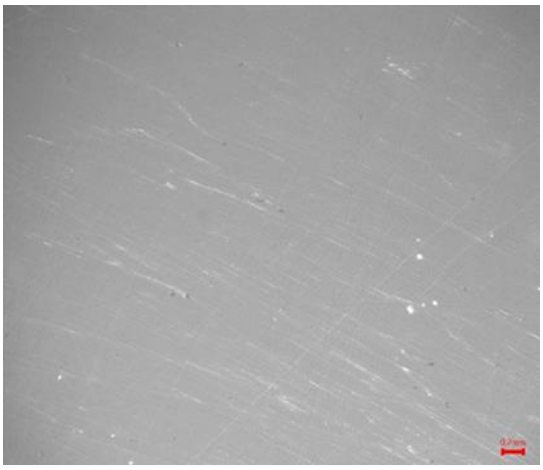

b. Lenses without protection with diopter -0.50

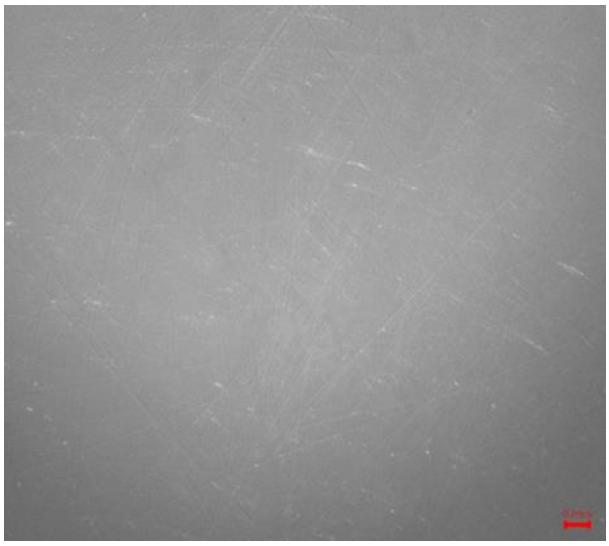

c. Lenses with medium protection with diopter -0.25

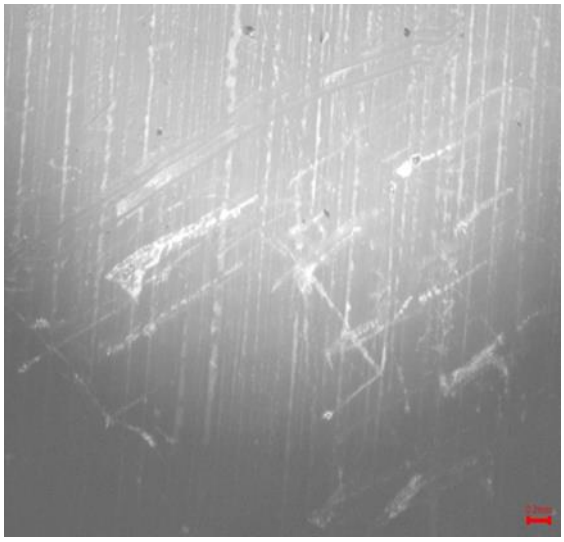

d. Lenses without protection with diopter -0.25

Fig. 5. *Lenses with diopters of -0.50 and -0.25 with and without protection, cleaned with eyeglass wipes*

The greatest degree of deterioration in surface quality was observed at unprotected lenses, cleaned with an eyeglass wipe. I recommend using wipes to clean your glasses as rarely as possible, only in situations where we cannot immediately use liquid soap.

In the group of lenses analysed under the optical microscope, we also included a pair of non-prescription sunglasses, from the lower quality category, cleaned with eyeglass wipes and dishwashing detergent, to highlight the fact that their surface quality is also influenced by cleaning products.

For both cleaning products, the surface was damaged. The images are presented in Fig. 6.

Following microscopic analysis of the surfaces of spectacle lenses for vision protection and correction, we concluded that long-term maintenance of lenses with inappropriate products damages vision by affecting the quality of the lens surface.

THE ANNALS OF "DUNAREA DE JOS" UNIVERSITY OF GALATI
FASCICLE IX. METALLURGY AND MATERIALS SCIENCE
Nº. 4 - 2024, ISSN 2668-4748; e-ISSN 2668-4756
Article DOI: https://doi.org/10.35219/mms.2024.4.05

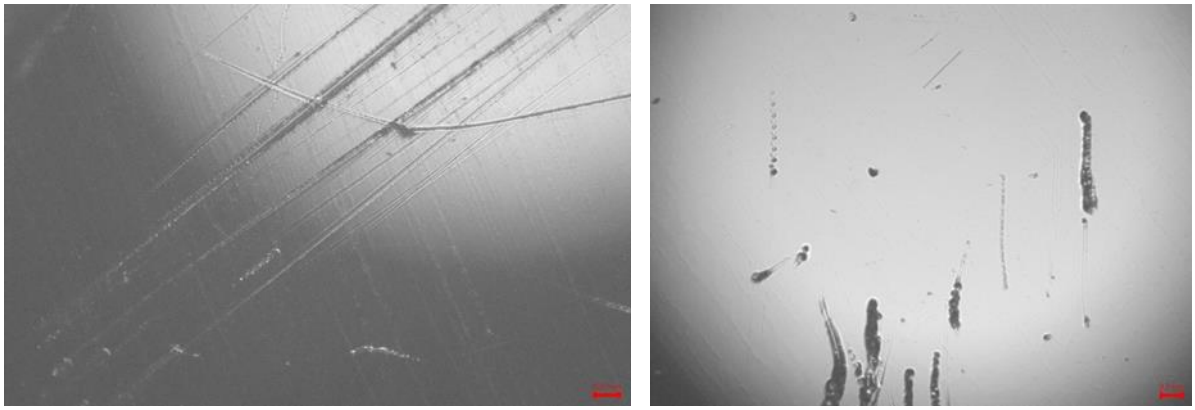

a. sunglasses lens, cleaned with glasses wipes b. sunglasses lens, cleaned with detergent

Fig. 6. *Sunglasses lenses without prescription, cleaned with eyeglass wipes and dishwashing detergent*

The materials used to clean lenses, used improperly and over a long period of time, accentuate vision difficulties, deepening them over time by deteriorating the quality of the lens surface. As a result of using these cleaning materials, scratches appeared on the lens surface and the protective layer was damaged.

The most damaged surfaces were on lenses that were cleaned with dishwashing detergent, which had the highest pH value.

The best surface quality was obtained at lenses cleaned with liquid soap.

Lenses cleaned with eyeglass wipes showed scratches after multiple uses.

Both uncoated and coated lenses showed deterioration in surface quality, with more advanced surface deterioration occurring in lenses without a protective coating.

4. Conclusions

The experimental research consisted of evaluating the influence of maintenance products, such as cleaning solutions, on the quality of lenses. We analysed the influence of these cleaning products on scratch resistance and image clarity. The results of this study are essential for improving the quality of lenses and associated maintenance products.

A deeper understanding of the optical and mechanical characteristics of lenses and how they are affected by maintenance products can contribute to the development of more durable and efficient lenses that best meet the needs of users. The results of this study are essential for knowing how to maintain these lenses to preserve the properties and quality of the surfaces.

References

[1]. ***, Differences_in_the_optical_properties_of_photochro%20MATERIALE%20PROTECȚIE%20LENTILE.pdf.
[2]. ***, Method_of_glass_selection_for_color_correction_in_%20MATERIALE%20PROTECȚIE%20LENTILE.pdf.
[3]. ***, Photochromic_Coatings%20MATERIALE%20PROTECȚIE%20LENTILE.pdf.
[4]. ***, https://www.everydayhealth.com/vision/new-directions-whats-coming-down-the-pike-in-eyewear/.
[5]. ***, https://www.icf.ro/Institut/lab04/XPS_ESCA_book2009.pdf.
[6]. ***, https://www.phys.uaic.ro/wp-content/uploads/2022/05/Lisnic-Petru-Rezumatul-tezei-de-doctorat.pdf.
[7]. ***, https://www.ucecom-spiruharet.ro/wp-content/uploads/2014/05/MIX_Tehnologia-lentilelor_teme.pdf.

THE ANNALS OF "DUNAREA DE JOS" UNIVERSITY OF GALATI
FASCICLE IX. METALLURGY AND MATERIALS SCIENCE
N°. 4 - 2024, ISSN 2668-4748; e-ISSN 2668-4756
Article DOI: https://doi.org/10.35219/mms.2024.4.06

ENHANCED RETINAL VESSEL DETECTION USING GRADIENT PYRAMID FUSION ALGORITHM

Cristian-Dragoș OBREJA
Department of Materials and Environmental Engineering, Faculty of Engineering, "Dunarea de Jos" University of Galati 47 Domneasca, 800008 Galati, Romania
e-mail: cristian.obreja@ugal.ro

ABSTRACT

The main goal of this study is to create an innovative approach to retinal vessel detection using the gradient pyramid fusion algorithm to improve edge continuity and measurement precision in retinal images. Traditional methods, like wavelet transform and guided filter, face challenges with background noise, artifacts and uneven illumination, which can distort vessel measurement. The proposed fusion method manages to overcome these limitations by combining the strengths of traditional techniques, which creates more continuous edges through gradient fusion across multiple scales, thus managing to also limit the number of image artifacts. We used images from the DRIVE database, to evaluate the fusion algorithm's precision, with results showing improved vascular tree detection and continuous edges, a reduction in the number of artifacts and improved measurement accuracy. The results show that this image fusion method improves the retinal image analysis, thus helping in early disease diagnosis.

KEYWORDS: wavelet transform, gradient pyramid fusion, edge detection, image fusion, guided filter

1. Introduction

Retinal image analysis is playing an important role in early detection and diagnosis of ocular and systemic diseases, especially those concerning the vascular system, such as diabetic retinopathy and hypertension. Vascular abnormalities, such as those generated by diabetic retinopathy, often require accurate measurement, however, asymmetry in vessels and complex backgrounds are usually some of the motives contributing to the lack of precision in vessel diameter measurements [1-3]. Most algorithms today detect blood vessels using techniques related to segmentation, probing or edge detection. These are realized by using various gradient masks for edge detection. Furthermore, morphological operations are carried out to obtain accurate edge maps especially for noise affected images. Thresholding is a fundamental method of image segmentation, which separates foreground (in our case, blood vessels) from background [4-9]. Moreover, advanced threshold techniques continue to enhance information coming from localized areas of an image. Probing methodology uses algorithms in which a vessel path is tracked while detecting edges in a real time manner. However, these bear serious limitations due to background noise and uneven illumination, thereby making quantitative measurements difficult [10-14]. In this paper the gradient pyramid image fusion algorithm represents a new method used to overcome such limitations by merging the merits of different traditional filters. [10] Using a merged representation of gradient pyramids, the technique proposed here attempts to generate sharper and more continuous edges without affecting any important useful information in the retinal images. The performance of the GPF algorithm for producing high-quality vascular edge maps and accurate measurement values of retinal vessel diameter is assessed in this paper. [14-16]

The structure of the paper is organised in four sections, the firs one is introduction. Section 2 covers materials and methods, while Sections 3 present experimental results and discussion. Conclusions are provided in Section 5.

2. Materials and methods

2.1. Database and the Algorithm

A total of 40 retinal images from the DRIVE digital retinal image database were analysed [17].

THE ANNALS OF "DUNAREA DE JOS" UNIVERSITY OF GALATI
FASCICLE IX. METALLURGY AND MATERIALS SCIENCE
Nº. 4 - 2024, ISSN 2668-4748; e-ISSN 2668-4756
Article DOI: https://doi.org/10.35219/mms.2024.4.06

This dataset consists of 20 randomly selected images and 20 manually segmented images, which serve as ground truth. Figure 1 illustrates the flowchart of the proposed method.

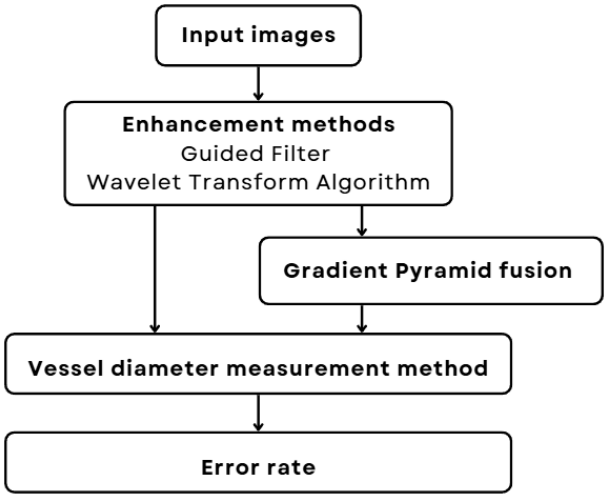

Fig. 1. *Flow chart of the proposed method*

2.2. Guided Filter (GF)

It is an image processing technique that has wide applications in edge-preserving, smoothing, noise reduction, and detail enhancement. It differs from other basic averaging filters, which blur edges across the board, in that it smooths out with the preservation of edges. The main steps of the guided filter are: computation of the mean and variance of the guidance image, calculate the correlation between the guidance image and the input image, use these values in generating filtering coefficients and apply these coefficients to produce the final filtered image. The algorithm is based on a set of equations [18-20]. Local means of the input image and guidance image are computed using a window of size determined by the radius:

$$\mu_G = \frac{1}{|\omega|}\sum_{i\epsilon\omega} G(i), \mu_I = \frac{1}{|\omega|}\sum_{i\epsilon\omega} I(i)$$

where ω *is the* number of pixels in the local window.

In the next step, we calculate the variance of the guidance image locally, covariance between the guidance and the input image as:

$$\sigma_G^2 = \frac{1}{|\omega|}\sum_{i\epsilon\omega}(G(i) - \mu_G)^2$$

$$\sigma_{IG} = \frac{1}{|\omega|}\sum_{i\epsilon\omega}(G(i) - \mu_G)(I(i) - \mu_I)$$

The filtering coefficients a and b are then calculated, with the former controlling the detail adaptation rate:

$$a = \frac{\sigma_{IG}}{\sigma_G^2 + \varepsilon}$$

$$b = \mu_I - a * \mu_G$$

where ε represents the regularization constant to control the edge preservation level. Furthermore, the final filtered image is obtained by the local weighted average of coefficients:

$$Q(i) = a * G(i) + b$$

This filter finds frequent application in image denoising and detail amplification because of the great efficiency and versatility in maintaining important structural features of images [18].

2.3. Wavelet Transform-Based Algorithm (WT)

The Wavelet Transform-Based Enhancement algorithm is a sophisticated method in image processing aimed at reducing noise and bringing out finer details. It works by breaking down an image into frequency components through the Discrete

THE ANNALS OF "DUNAREA DE JOS" UNIVERSITY OF GALATI
FASCICLE IX. METALLURGY AND MATERIALS SCIENCE
Nº. 4 - 2024, ISSN 2668-4748; e-ISSN 2668-4756
Article DOI: https://doi.org/10.35219/mms.2024.4.06

Wavelet Transform (DWT). This decomposition allows the separation of low-frequency components (representing the main structure of the image) from high-frequency components (containing fine details and noise). By adjusting each component selectively, this approach balances noise reduction with detail enhancement [21].

The algorithm involves four primary stages: wavelet decomposition, noise reduction, detail enhancement, and wavelet reconstruction, each governed by specific mathematical operations:

• Wavelet Decomposition: The image is split into multiple levels, yielding a vector of wavelet coefficients (C) and a structure (S) that defines each level's size. This is represented by the equation:

$$C, S = wavedec2(I, decomposition\_level, wavelet\_type)$$

• Noise Reduction: Using a technique called soft thresholding, noise is reduced by setting small, noisy details to zero, preserving significant parts. This operation is expressed as:

$$\mathrm{d}\_thresholded = sign(d) \cdot max(|\ d\ | - noise\_threshold, 0)$$

• Detail Enhancement: Here, the remaining details are boosted by multiplying specific wavelet coefficients by a "detail factor," enhancing edges and finer structures. This is shown with:

$$d\_enhanced = \mathrm{d}\_thresholded \cdot detail\_factor$$

• Wavelet Reconstruction: Finally, all modified coefficients are combined to reconstruct an enhanced image using the inverse wavelet transform:

$$I\_enhanced = waverec2(C\_modified\ , S, wavelet\_type).$$

This method improves image quality by reducing unwanted noise and emphasizing edges, yielding a cleaner, sharper result [22].

2.4. Gradient Pyramid fusion algorithm (GPF)

The Gradient Pyramid fusion algorithm combines multiple images by capturing and merging key details across varying scales. It starts by decomposing each input image into a pyramid of gradient images, which represents intensity changes at multiple scales. Each pyramid level highlights gradients that reveal shifts in intensity, isolating critical features in each image.

The algorithm then proceeds with the fusion stage, where it creates gradient pyramids for each input image and selects the maximum gradient at every level. This selection effectively merges the most prominent details from both images into a unified gradient pyramid. The fused pyramid is then used to reconstruct a single, cohesive image that retains essential details from the original inputs.

The process involves several key steps: constructing the gradient pyramid by calculating gradient magnitudes using Sobel filters, down sampling each level with pyramid (using 'reduce') for each RGB channel, and expanding each pyramid level in the reconstruction stage to add it to the level below. This process is repeated independently for each colour channel to produce a final, full-colour RGB image. Finally, the algorithm saves and displays the original images, the gradient pyramids, and the fused image, providing a clear view of how features from the input images combine into a refined, enhanced result [23-25].

At each level l in the pyramid, the fused gradient $G_F^{(l)}$ is obtained by selecting the maximum gradient values from each pixel of the two input images, $G_A^{(l)}$ and $G_B^{(l)}$:

$$G_F^{(l)}(x,y) = \max(G_A^{(l)}(x,y), G_B^{(l)}(x,y))$$

where $G_A^{(l)}$ is the gradient of image A at level l, $G_B^{(l)}$ is the gradient of image B at level l, $G_F^{(l)}$ is the fused gradient at level l and (x,y) are the pixel coordinates. This equation selects the strongest edges at each level and pixel position, ensuring that the most prominent features from both images are preserved.

THE ANNALS OF "DUNAREA DE JOS" UNIVERSITY OF GALATI
FASCICLE IX. METALLURGY AND MATERIALS SCIENCE
Nº. 4 - 2024, ISSN 2668-4748; e-ISSN 2668-4756
Article DOI: https://doi.org/10.35219/mms.2024.4.06

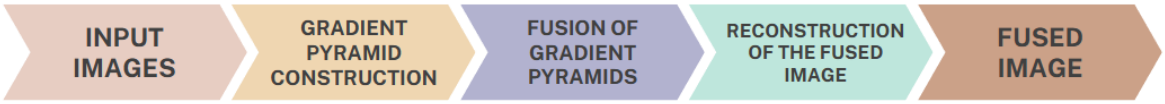

Fig. 2. *Flow chart of the fusion algorithm*

2.5. Vessel Diameter Measurement

The vessel diameter measurement method outlined here uses a series of precise image processing steps to accurately detect and analyse vessel diameters. It begins with contrast enhancement through CLAHE (Contrast Limited Adaptive Histogram Equalization), which boosts vessel visibility by enhancing contrast [26]. Next, edge detection via the Canny method identifies vessel boundaries, with an optional morphological closing step to seal small gaps in these edges.

Afterward, skeletonization reduces the vessel image to a single-pixel-wide structure, simplifying the geometry for measurement. A distance transform then calculates the Euclidean distance from each pixel to the nearest edge; doubling this distance gives an estimated diameter at each skeleton point. Finally, all non-zero diameter values are collected, and the mean diameter is calculated and presented for analysis [27].

Fig. 3. *Flow chart of the vessel diameter measurement algorithm*

3. Results and discussion

To evaluate the proposed fusion algorithm's performance relative to traditional filters, tests were conducted on a set of 20 randomly selected retinal images. Figure 4 provides examples of vascular maps generated using the Gradient Pyramid fusion, Wavelet Transform-based algorithm, and Guided Filter. Diameter measurements were made for retinal vessels across all images, comparing processed, fused, and ground truth data for a comprehensive assessment.

Fig. 4. *Examples of vascular map. (a) Original input image; (b) ground truth image; (c) Guided filter; (d) Wavelet transform-based filter; (e) Gradient Pyramid fusion*

Figure 5 shows examples of vascular maps produced during the different stages of the vessel diameter measurement algorithm. The processed images (both by guided filter and wavelet algorithm) together with the fused image, are used as input information for the vessel diameter measurement algorithm. Over this images a contrast enhancement algorithm is applied, followed by Canny edge detector. Finally, a skeletonization operation is made and the blood vessel diameter map is generated, followed by the diameter's values measurement.

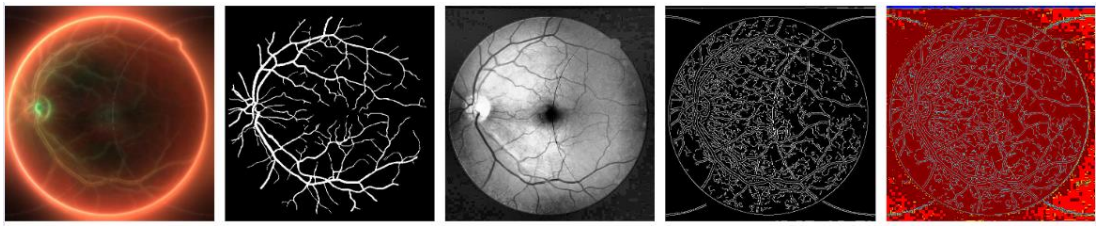

Fig. 5. *Examples of vascular map. (a) Fused image; (b) ground truth image; (c) CLAHE filter; (d) Canny edge detection; (e) Blood vessel diameter map*

THE ANNALS OF "DUNAREA DE JOS" UNIVERSITY OF GALATI
FASCICLE IX. METALLURGY AND MATERIALS SCIENCE
Nº. 4 - 2024, ISSN 2668-4748; e-ISSN 2668-4756
Article DOI: https://doi.org/10.35219/mms.2024.4.06

Table 1 displays the average vessel diameter values along with the associated error rates for the Gradient Pyramid fusion, Wavelet Transform-based algorithm, and Guided Filter.

This paper examines the Gradient Pyramid fusion algorithm's ability to generate highly accurate edge maps, particularly for measuring retinal vessel diameters and calculating error rates. One major advantage of this fusion method is its capability to produce uninterrupted edges.

Table 1. *The average vessel diameter values and the average percentage error*

Ground truth	GF	e_{GF}%	WT	e_{WT}%	GPF	e_{GPF}%
2.210	2.097	5.128	2.098	5.053	2.137	3.318

As shown in Table 1, the average vessel diameters and error percentages are reported for manually segmented, filtered, and fused retinal images. Among traditional filters, the wavelet transform-based filter (WT) shows the lowest error rates. WS's average error rate is 5.053%, while GF's error rate is 5.053%. The GPF fusion further improves accuracy, with an error rate of 3.318%.

As illustrated in Figure 4, the WT and GF filters enhance the image and improve edges, but there are still areas where there is not enough of a difference between the blood vessel edge and the background. Furthermore, the fusion method achieves greater accuracy and lower error rates than traditional filters. Gradient Pyramid fusion yields the highest alignment with the ideal edge map, as defined by manual segmentation. Traditional enhancement algorithms may lack precision, while the fusion technique effectively combines the strengths of both filters to achieve smooth, continuous edges without over-detection.

Despite the additional edges from distorted vessels in retinopathy maps, GPF fusion consistently outperforms conventional filters in identifying true edges. By merging the outputs of WT and GF, this fusion method enhances the accuracy of retinal images more effectively than either filter alone.

4. Conclusions

This study demonstrates the Gradient Pyramid Fusion (GPF) algorithm's effectiveness in producing accurate, high-quality edge maps for retinal images, particularly for vessel diameter measurement. By combining the strengths of the Wavelet Transform (WT) and Guided Filter (GF), GPF significantly improves accuracy, continuity, and edge definition over traditional filters. Supported by quantitative analysis, the results show that GPF excels at preserving essential structural features while reducing error rates, making it a promising tool for advancing retinal image analysis and other applications that demand precise edge detection and image enhancement.

References

[1]. Abràmoff M. D., Lavin P. T., Birch M., Shah N., Folk J. C., *Pivotal trial of an autonomous AI-based diagnostic system for detection of diabetic retinopathy in primary care offices*, Digital Medicine, 1(1), p. 1-8, https://doi.org/10.1038/s41746-018-0040-6, 2018.

[2]. Antal B, Hajdu A., *An ensemble-based system for microaneurysm detection and diabetic retinopathy grading*, IEEE Transactions on Bio-medical Engineering, 59(6), p. 1720-1726, DOI: 10.1109/tbme.2012.2193126, 2012.

[3]. Fraz M. M., *et al.*, *Blood vessel segmentation methodologies in retinal images–a survey*, Computer Methods and Programs in Biomedicine, 108 (1), p. 407-433, https://doi.org/10.1016/j.cmpb.2012.03.009, 2012.

[4]. Niemeijer M., *et al.*, *Retinopathy online challenge: automatic detection of microaneurysms in digital color fundus photographs*, IEEE Trans Med Imaging, 29(1), p. 185-95, doi: 10.1109/TMI.2009.2033909, 2010.

[5]. Staal J., *et al.*, *Ridge-based vessel segmentation in color images of the retina*, IEEE Transactions on Medical Imaging, 23 (4), p. 501-509, https://doi.org/10.1109/TMI.2004.825627, 2004.

[6]. Zana F., Klein J. C., *Segmentation of vessel-like patterns using mathematical morphology and curvature evaluation*, IEEE Transactions on Image Processing, 10 (7), p. 1010-1019, https://doi.org/10.1109/83.931095, 2001.

[7]. Hoover A., Kouznetsova V., Goldbaum M., *Locating blood vessels in retinal images by piecewise threshold probing of a matched filter response*, IEEE Transactions on Medical Imaging, 19 (3), p. 203-210, https://doi.org/10.1109/42.845178, 2000.

[8]. Soares J. V., *et al.*, *Retinal vessel segmentation using the 2-D Gabor wavelet and supervised classification*, IEEE Transactions on Medical Imaging, 25 (9), p. 1214-1222, https://doi.org/10.1109/TMI.2006.879967, 2006.

[9]. Yin Y., Adel M., Bourennane S., *Retinal vessel segmentation using a probabilistic tracking method*, Pattern Recognition, 45 (4), p. 1235-1244, https://doi.org/10.1016/j.patcog.2011.09.019, 2012.

[10]. Kaur H., Koundal D., Kadyan V., *Image Fusion Techniques: A Survey*, Arch Computat Methods Eng, 28, p. 4425-4447, https://doi.org/10.1007/s11831-021-09540-7, 2021.

[11]. Budai A., *et al.*, *Robust vessel segmentation in fundus images*, International Journal of Biomedical Imaging, Article 154860, https://doi.org/10.1155/2013/154860, 2013.

[12]. Al-Diri B., Hunter A., Steel D., *An active contour model for segmenting and measuring retinal vessels*, IEEE Trans Med Imaging, 28(9), p. 1488-97, doi: 10.1109/TMI.2009.2017941, 2009.

[13]. Zhang B., *et al.*, *Retinal vessel extraction by matched filter with first-order derivative of Gaussian*, Computer Methods and Programs in Biomedicine, 122 (3), p. 168-179. https://doi.org/10.1016/j.cmpb.2015.08.008, 2015.

[14]. Dashtbozorg B., *et al.*, *An automatic graph-based approach for artery/vein classification in retinal images*, IEEE Trans Image Process, 23(3), p. 1073-83, doi: 10.1109/TIP.2013.2263809, 2014.

[15]. Zhang L., Zhang J., *A New Saliency-Driven Fusion Method Based on Complex Wavelet Transform for Remote Sensing Images*,

in IEEE Geoscience and Remote Sensing Letters, vol. 14, no. 12, p. 2433-2437, doi: 10.1109/LGRS.2017.2768070, 2017.

[16]. Jiang X., Mojon D. S., *Adaptive local thresholding by verification-based multithreshold probing with application to vessel detection in retinal images*, IEEE Transactions on Pattern Analysis and Machine Intelligence, 25 (1), p. 131-137, https://doi.org/10.1109/TPAMI.2003.1159954, 2003.

[17]. ***, *DRIVE: Digital Retinal Images for Vessel Extraction* (Image Sciences Institute, University Medical Center Utrecht), http://www.isi.uu.nl/Research/Databases/DRIVE/, 2004.

[18]. He K., Sun J., Tang X., *Guided image filtering*, IEEE Transactions on Pattern Analysis and Machine Intelligence, 35(6), p. 1397-1409, https://doi.org/10.1109/TPAMI.2012.213, 2013.

[19]. He K., Sun J., Tang X., *Guided image filtering*, IEEE Trans Pattern Anal Mach Intell, 35(6), p. 1397-409, doi: 10.1109/TPAMI.2012.213, PMID: 23599054, 2013.

[20]. Kou F., *et al.*, *Gradient Domain Guided Image Filtering*, IEEE Trans Image Process, 24 (11), p. 4528-39, doi: 10.1109/TIP.2015.2468183, 2015.

[21]. Mallat S., *A theory for multiresolution signal decomposition: The wavelet representation*, IEEE Transactions on Pattern Analysis and Machine Intelligence, 11 (7), p. 674-693, https://doi.org/10.1109/34.192463, 1989.

[22]. Donoho D. L., *De-noising by soft-thresholding*, IEEE Transactions on Information Theory, 41 (3), p. 613-627, https://doi.org/10.1109/18.382009, 1995.

[23]. Li S., Kang X., Hu J., *Image fusion with guided filtering*, IEEE Transactions on Image Processing, 22 (7), p. 2864-2875, https://doi.org/10.1109/TIP.2013.2244222, 2013.

[24]. Burt P. J., Adelson E. H., *The Laplacian pyramid as a compact image code*, IEEE Transactions on Communications, 31 (4), p. 532-540, https://doi.org/10.1109/TCOM.1983.1095851, 1983.

[25]. Shao Z., Cai J., *Remote Sensing Image Fusion with Deep Convolutional Neural Network*, IEEE Journal of Selected Topics in Applied Earth Observations and Remote Sensing, vol. 11, no. 5, p. 1656-1669, doi: 10.1109/JSTARS.2018.2805923, 2018.

[26]. Moraru L., *et al.*, *Retinal vessel enhancement based on the Gaussian function and image fusion*, AIP Conf. Proc., 1796 (1), 040007, https://doi.org/10.1063/1.4972385, 2017.

[27]. Li R., *et al.*, *A survey of multi-source image fusion*, Multimed Tools Appl, 83, p. 18573-18605, https://doi.org/10.1007/s11042-023-16071-9, 2024.

THE ANNALS OF "DUNAREA DE JOS" UNIVERSITY OF GALATI
FASCICLE IX. METALLURGY AND MATERIALS SCIENCE
Nº. 4 - 2024, ISSN 2668-4748; e-ISSN 2668-4756
Article DOI: https://doi.org/10.35219/mms.2024.4.07

REMEDIATION OF SOIL CONTAMINATED WITH HYDROCARBON USING THE SUCCESIVE EXTRACTION METHOD WITH SOLVENTS

Maria POPA
Petroleum-Gas University of Ploiesti, Faculty of Petroleum Refining and Petrochemistry, Romania
e-mail: mpopa@upg-ploiesti.ro

ABSTRACT

Soils can be accidentally polluted with liquid hydrocarbons. The penetration of the pollutant into the soil structure will always be both vertical and horizontal. It is very important to act immediately to stop this migration. The choice of the depollution method is the most difficult action to be chosen by specialists.

The paper deals with the method of successive solvent extraction, the solvents used being, in order of use: petroleum ether, benzene and toluene. Two soil types were chosen: garden soil from Romania and red soil from Greece. The degree of depollution (%) is calculated for each of the two soil types.

KEYWORDS: soil properties, extraction, pollutant, diesel oil

1. Introduction

When, accidentally or not, a soil is polluted with liquid hydrocarbons, they migrate into the soil structure in different ways. This is influenced by the soil properties (density, capillarity, particle size and permeability) as well as the properties of the pollutant (density and viscosity).

When the nature of the pollutant is known, it is easier to choose the extraction solvents. If there is insufficient information on the composition of the pollutant, the choice of solvents comprises a longer list [1-4].

In this paper, two types of soils were chosen which were polluted under laboratory-controlled conditions with 5% of the same pollutant – diesel oil.

The studies carried out on this topic were based on the analysis of soils and their behavior in successive solvent extractions. The method of depollution by successive extractions has high costs, but pollutant recovery can be a gain [1].

There are many recent studies on accidental pollution, soil being the most affected environmental factor [5-9].

2. Material and methods

2.1. Soil analysis

Two soil types were chosen for the experiments: garden soil and red soil.

The garden soil used in the experiments had not been treated in the last 20 years with chemicals that could have altered its physical properties and nutrient content in any way.

The red soil is soil taken from a swampy, vegetated area that is undisturbed by human action.

The two soil types were characterized by: density, capillarity, permeability and grain size.

Soil density is a property that depends on several factors (depth, degree of subsidence, moisture content, organic and inorganic matter content) [10].

Two types of density are defined and can be calculated:

Apparent density:

$$\rho_{apparent} = \frac{m_{soil}}{V_{soil\ layer}}, \text{ g/cm}^3 \quad (1)$$

Real density:

$$\rho_{real} = \frac{m_{soil}}{V_{soil}} = \frac{m_{soil}}{V_{soil\ layer} - V_{voids}}, \text{ g/cm}^3 \quad (2)$$

Knowing these densities can also determine the porosity of the soil:

$$\varepsilon = 1 - \frac{\rho_{apparent\ soil}}{\rho_{real\ soil}} \quad (3)$$

The determinations were made in a glass ampoule as shown in Figure 1.

THE ANNALS OF "DUNAREA DE JOS" UNIVERSITY OF GALATI
FASCICLE IX. METALLURGY AND MATERIALS SCIENCE
N°. 4 - 2024, ISSN 2668-4748; e-ISSN 2668-4756
Article DOI: https://doi.org/10.35219/mms.2024.4.07

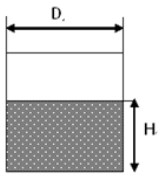

Fig. 1. *Glass ampoule with soil sample* [10]

Capillarity is the property that represents the phenomenon of a liquid penetrating the soil structure from bottom to top. This penetration occurs through the spaces between solid aggregates. In order to establish this penetration into the soil structure, it is necessary to moisten the soil samples, since it is necessary to imitate the horizons of soils [1, 2].

The device used in the laboratory consists of a glass tube (L > 50 cm, di = 2 cm) into which the moistened soil is introduced over a length of 50 cm.

The tube is protected at the base with gauze to prevent loss of sample. It is immersed in a vessel containing the liquid to be analysed (water and diesel oil).

Due to the capillarity of the soil layer the liquid will move ascending and form a moving moisture front, characterized by the height $H_{humidity}$ (H).

The value of the wet height will be measured every 10 minutes for one hour. Finally, the variation of the height of the moisture front with time will be graphically plotted.

The experimental scheme is shown in Figure 2.

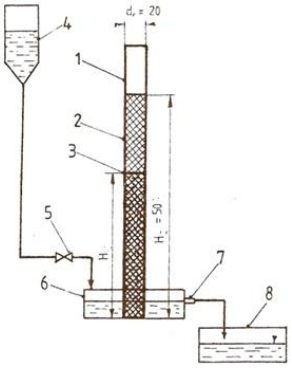

Fig. 2. *The experimental scheme for capillarity* [10]. *1-glass tube, 2-soil layer, 3-moisture front, 4-liquid supply vessel, 5-holding, 6- constant liquid level vessel, 7-pre-fill zone, 8-collecting*

Permeability is the property of soil that allows a fluid to flow through its structure. It is dependent on the clearances between soil aggregates. In the case of a pollutant, this property will influence the infiltration rate in the event of an accidental spill. The movement of the pollutant front leaves behind a soil saturated with the pollutant.

After the fluid permeates through the soil layer and begins to drip into the graduated cylinder 6 start measuring the time, noting the amounts filtered, at 15-minute intervals for one hour. After one hour, stop the flow of fluid and wait until all the fluid above the soil layer has passed through the soil volume and no more drops are flowing into the graduated cylinder 6 at the bottom.

The amount of liquid product embedded in the soil structure represents the retention capacity of that soil (kg liquid/m^3 dry soil). The retention capacity varies inversely with permeability [10].

The values measured and calculated during operation of the module to determine the permeability and retention capacity are:

$$V_{soil} = \frac{\pi \cdot d_{soil}^2}{4} \cdot H_{soil}, \text{ cm}^3 \quad (4)$$

- H_{soil} - soil layer height, cm;
- d_{soil} - soil layer diameter, cm;
- V_{soil} - soil layer volume, cm^3.

$$P_\tau = V_\tau \cdot \frac{60}{\tau}, \text{ cm}^3/\text{h} \quad (5)$$

- Pτ - average permeability for time τ, cm^3/h;
- Vτ - the volume of liquid filtered through the layer during τ = 15, 30, 45, 60 minutes.

$$P_a = \frac{P_{15}+P_{30}+P_{45}+P_{60}}{4}, \text{ cm}^3/\text{h} \quad (6)$$

P_a - average total permeability, cm^3/h.

$$C_R = \frac{(m_f - m_o)\cdot 10^3}{V_{soil}}, \text{ kg liquid/m}^3\text{soil} \quad (7)$$

- C_R - retention capacity, kg liquid/m^3soil;
- m_i the initial mass of the dry soil layer, g;
- m_f the final mass of the dry soil layer, g.

The experimental scheme is shown in Figure 3.

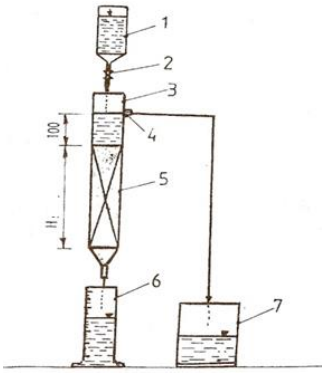

Fig. 3. *The experimental scheme for permeability* [10]. *1-liquid feed vessel, 2-holding, 3-glass tube Wolff, 4-strainer, 5-soil layer, 6-graduated cylinder, 7-collector vessel*

THE ANNALS OF "DUNAREA DE JOS" UNIVERSITY OF GALATI
FASCICLE IX. METALLURGY AND MATERIALS SCIENCE
Nº. 4 - 2024, ISSN 2668-4748; e-ISSN 2668-4756
Article DOI: https://doi.org/10.35219/mms.2024.4.07

Granulometry is the percentage distribution of soil particle size. In general, soil with a larger particle size will be more permeable to liquids. This property will be determined by the sieving method. The experimental assembly is shown in Figure 4.

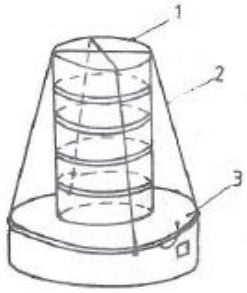

Fig. 4. *The experimental assembly for granulometry* [10]. *1-sifting sieves with different holes, 2-elastic support ropes, 3- vibrating system for the sieves*

2.2. Pollutant analysis

The controlled pollution product (5%) was characterized by density and viscosity, properties that will influence the penetration of the pollutant into the soil structure. These determinations were made at three different temperatures (20, 40 and 60 Celsius degree).

2.3. Extractive depollution method

Based on solubility differences, the separation of components from the soil pollutant can be realized by extraction. The solid-liquid extraction is done using the Soxhlet apparatus, as shown in Figure 5. The successive solvent extraction method involves the use of several solvents without removing the sample from the apparatus. Different solvents are used which will extract different components of the pollutant. These were, in order of use: petroleum ether, benzene, toluene. For each solvent used over the polluted sample cartridge, the extraction takes until the solvent is 'clean'. With a single solvent, extraction can take several hours. In each case, the solvent used can be recovered and the test sample will be oven dried at a temperature slightly above the boiling temperature of the solvent. The sample remaining after drying is weighed.

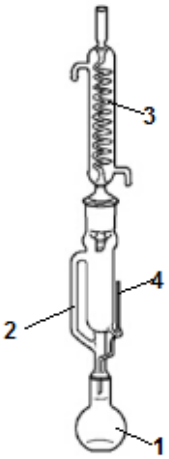

Fig. 5. *Soxhlet apparatus* [10]. *1-distilling ball, 2-side tube, 3-cooler, 4-siphon apparatus*

3. Results and discussions

The densities for the two soil samples are shown in Table 1.

Table 2 shows the measured values for the layer wetted with the two liquids: water and diesel oil.

Figure 6 shows the variation of the wetted layer height with time.

Table 3 shows the results for the average permeability and the retention capacity.

Table 4 shows the granulometric variation and Figure 7 shows the histogram corresponding to this variation.

The density and viscosity of diesel oil are given in the Table 5 for three temperatures.

Table 1. *Calculated values for density and porosity*

No. crt.	Calculated sizes	UM	Type of soil	
			Garden soil	Red soil
1.	m_{soil}	g	43	50.4
2.	$V_{soil\ layer}$	cm^3	52.8	52.8
3.	V_{voids}	cm^3	24.7	19.5
4.	Apparent density, $\rho_{apparent}$	g/cm^3	0.814	0.955
5.	Real density, ρ_{real}	g/cm^3	1.53	1.51
6.	Porosity, ε	-	0.468	0.368

THE ANNALS OF "DUNAREA DE JOS" UNIVERSITY OF GALATI
FASCICLE IX. METALLURGY AND MATERIALS SCIENCE
N°. 4 - 2024, ISSN 2668-4748; e-ISSN 2668-4756
Article DOI: https://doi.org/10.35219/mms.2024.4.07

Table 2. *Wetted layer heights for two types of soil*

No. crt.		Type of soil			
		Garden soil		Red soil	
		Water	Diesel oil	Water	Diesel oil
1.	$H_{10\ min}$, mm	28	36	39	49
2.	$H_{20\ min}$, mm	35	54	45	62
3.	$H_{30\ min}$, mm	42	67	51	62
4.	$H_{40\ min}$, mm	50	82	55	62
5.	$H_{50\ min}$, mm	56	89	57	64
6.	$H_{60\ min}$, mm	62	98	62	69

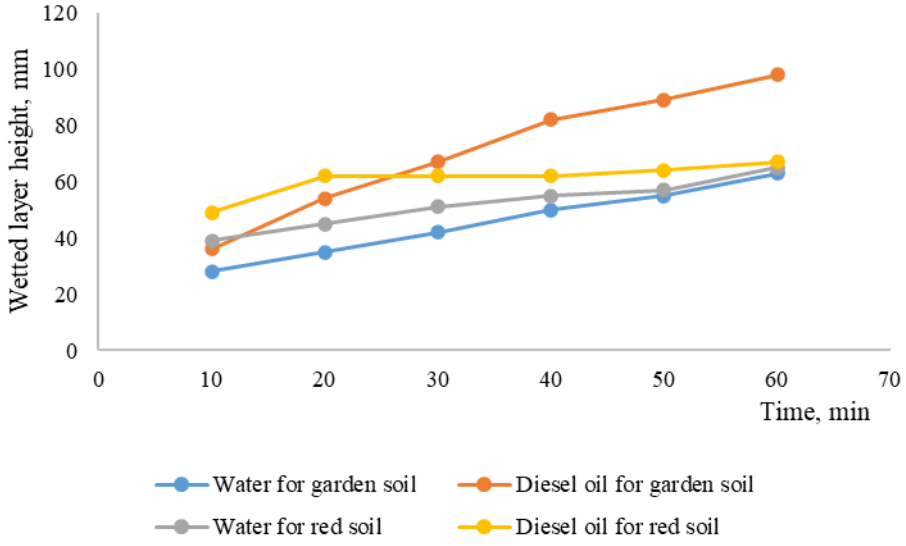

Fig. 6. *Variation in the height of the wetted layer with time*

Table 3. *Sizes measured and calculated for permeability and retention capacity*

No. crt.	Measured sizes	Type of soil			
		Garden soil		Red soil	
		Water	Diesel oil	Water	Diesel oil
1.	m_0, g	348.4	375.2	364.6	364.6
2.	H_{soil}, cm	12	13.8	14.5	14.5
3.	d_{soil}, cm	4.1	4.1	4.1	4.1
4.	V_{soil}, cm^3	158.4	182.2	191.4	191.4
5.	V_{15}, cm^3	300	22.5	410	715
6.	V_{30}, cm^3	546	45.4	710	1340
7.	V_{45}, cm^3	774	68.6	960	1920
8.	V_{60}, cm^3	924	92.5	1185	2410
9.	m_f, g	424	436.2	424.8	404.4
10.	P_{15}, cm^3/h	1200	90	1640	2860
11.	P_{30}, cm^3/h	1092	90.8	1420	2680
12.	P_{45}, cm^3/h	1032	91.47	1280	2560
13.	P_{60}, cm^3/h	924	92.5	1185	2410
14.	P_a, cm^3/h	1062	48.6	1381.25	2627.5
15.	C_R, kg/m^3	477	335	314.5	206

THE ANNALS OF "DUNAREA DE JOS" UNIVERSITY OF GALATI
FASCICLE IX. METALLURGY AND MATERIALS SCIENCE
Nº. 4 - 2024, ISSN 2668-4748; e-ISSN 2668-4756
Article DOI: https://doi.org/10.35219/mms.2024.4.07

Table 4. *Granulometric variation*

Type of soil		Sieve 1 1.5 mm	Sieve 2 0.49 mm	Sieve 3 0.2 mm	Sieve 4 0.12 mm	Sieve 5 0.088 mm	Sieve 6 0.06 mm	Σm_i	Sieve 7 Losses
Garden soil	m_i, g	49.6	32.8	8	2.4	1.6	0.8	95.2	4.8
	%	49.6	32.8	8	2.4	1.6	0.8	95.2	4.8
Red soil	m_i, g	55.4	30.6	8	3.4	0.2	0.1	97.6	2.4
	%	55.4	30.6	8	3.4	0.2	0.1	97.6	2.4

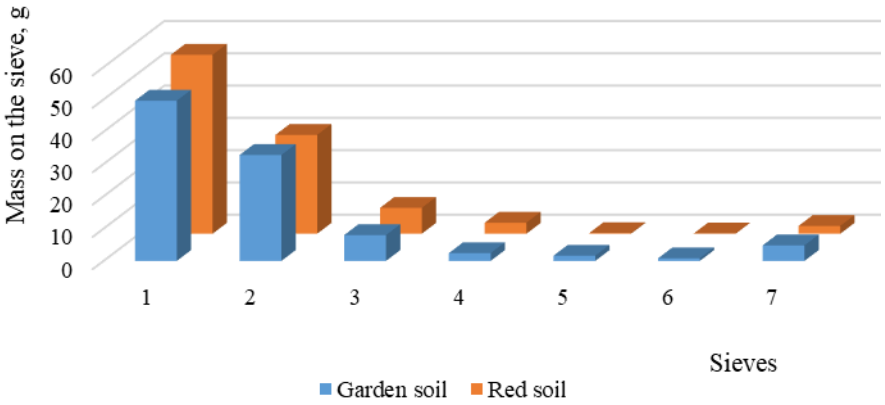

Fig. 7. *The histogram corresponding for granulometric variation*

Table 5. *The density and the viscosity values for diesel oil for three temperature*

No. crt.	Temperature, ºC	Diesel oil	
		Density, kg/m^3	Viscosity, kg/ms
1.	20	836.2	$5.2 \cdot 10^{-6}$
2.	40	819.6	$4.07 \cdot 10^{-6}$
3.	60	813.2	$3.23 \cdot 10^{-6}$

Table 6. *Results of successive solvent extraction for garden soil*

Clean garden soil			
	Petroleum ether	**Benzene**	**Toluene**
Organic material extracted with, g	0.0193	0.0287	0.0146
Total mass organic extracted, g	0.0626		
Polluted garden soil with 5% diesel oil			
	Petroleum ether	**Benzene**	**Toluene**
Total mass organic extracted + diesel oil with, g	0.5701	0.0184	0.0372
Total mass organic extracted + diesel oil, g	0.6252		
Total diesel oil extracted, g	0.563		
Depollution degree, %	56.3		

It was necessary for this study to know the physical properties of both soils and pollutants. This information helps to analyse the penetration of the pollutant into the soil structure.

When an environmental accident occurs, you need to act quickly. It is difficult to choose an optimal method for depollution of soils contaminated with hydrocarbons.

The successive extraction method with solvents can be one of these options.

The advantage of this method is that, although solvents are very expensive, they can be recovered in the successive extraction method. The pollutant can also be recovered.

THE ANNALS OF "DUNAREA DE JOS" UNIVERSITY OF GALATI
FASCICLE IX. METALLURGY AND MATERIALS SCIENCE
Nº. 4 - 2024, ISSN 2668-4748; e-ISSN 2668-4756
Article DOI: https://doi.org/10.35219/mms.2024.4.07

Table 7. *Results of successive solvent extraction for red soil*

Clean red soil			
	Petroleum ether	**Benzene**	**Toluene**
Organic material extracted with, g	0.0253	0.0413	0.03
Total mass organic extracted, g	0.0966		
Polluted red soil with 5% diesel oil			
	Petroleum ether	**Benzene**	**Toluene**
Total mass organic extracted + diesel oil with, g	0.9870	0.0692	0.0397
Total mass organic extracted + diesel oil, g	1.0959		
Total diesel oil extracted, g	0.9993		
Depollution degree, %	99.93		

4. Conclusions

The choice of soil types was not accidental. Garden soil has a high humus content (indicated by colour). The presence of this component has a great influence on the behavior of liquids (water and diesel oil).

The higher porosity of the garden soil (0.468) will influence the penetration and stagnation of liquids in voids.

The maximum wetted layer is 98 cm for diesel oil in garden soil compared to 69 cm for red soil.

The pollutant retention capacity in the soil is higher for garden soil (335 kg/m^3) than for red soil (206 kg/m^3). This aspect explains why the degree of depollution for red soil is higher (99.93%).

For successive extraction with solvents, when comparing results for different soils it is easy to determine the number of solvents. There is a possibility that for the lower degree of depollution, there may be another solvent to extract other components remaining in the soil structure. A proposed option for future studies would be a mixture of alcohol: benzene (1:1).

References

[1]. Popa M., *Tehnologii de depoluare și reconstrucție ecologică a solurilor contaminate*, Editura Universității Petrol-Gaze din Ploiești, ISBN 978-973-719-698-9, 2017.
[2]. Neag G., *Depoluarea solurilor și apelor subterane*, Editura Casa Cărții de Știință, Cluj Napoca, 1997.
[3]. Micle V., Neag Gh., *Procedee și echipamente de depoluare a solurilor și a apelor subterane*, Editura U.T. Press, Cluj-Napoca 2009.
[4]. Popa M., *Elemente de pedologie. Poluarea solurilor cu hidrocarburi și reconstrucția ecologică*, Editura Universității Petrol-Gaze din Ploiești, ISBN 978-973-719-747-4, 2018.
[5]. Sun Q., *et al.*, *Effect of Organic Fertilizer Application on Microbial Community regulation and Pollutant Accumulation in Typical Red Soil in South China*, Agronomy, 14 (9), 2150, https://doi.org/10.3390/agronomy14092150, 2024.
[6]. Ma Y., *et al.*, *The Impact of Humic Acid Fertilizers on Crop Yield and Nitrogen Use Efficiency: A Meta-Analysis*, Agronomy, 14 (12), 2763, https://doi.org/10.3390/agronomy14122763, 2024.
[7]. Pavel L. V., *Overview of ex situ decontamination techniques for soil cleanup*, Environmental Engineering and Management Journal, vol. 7, no. 6, p. 815-834, 2008.
[8]. Crețu R., *Investigation of some organic pollutants impact on physico-chemical characteristics of plantlets*, The Annals of Dunărea de Jos University of Galați, Fascicle IX, Metallurgy and Material Science, no. 3, https://doi.org/10.35219/mms.2019.3.08, 2019.
[9]. Tudor B. D., *Studies and research on soil analysis in a derelict area, where there was a landfill*, The Annals of Dunarea de Jos University of Galati, Fascicle IX, Metallurgy and Material Science, no. 1, https://doi.org/10.35219/mms.2023.1.07, 2023.
[10]. Pătrașcu C., *et al.*, *Depoluarea solurilor contaminate cu produse petroliere*, Editura Universității Petrol-Gaze din Ploiești, ISBN 978-973-719-243-1, 2008.

THE ANNALS OF "DUNAREA DE JOS" UNIVERSITY OF GALATI
FASCICLE IX. METALLURGY AND MATERIALS SCIENCE
Nº. 4 - 2024, ISSN 2668-4748; e-ISSN 2668-4756
Article DOI: https://doi.org/10.35219/mms.2024.4.08

DEVELOPING A NON-INVASIVE INTELLIGENT SYSTEM FOR BLOOD GLUCOSE LEVEL ESTIMATION USING REFLECTIVE OPTICAL SENSORS

Mihaela MARIN, Teodora Alexandra Dobrin, Florin Bogdan MARIN
"Dunarea de Jos" University of Galati, Romania
e-mail: mihaela.marin@ugal.ro

ABSTRACT

This paper introduces a non-invasive system for blood glucose monitoring using a reflective optical sensor (TCRT5000) integrated with an Arduino platform. The system integrates a detection unit equipped with an infrared LED, phototransistor, microcontroller, OLED display, and Bluetooth module-with real-time data visualization and wireless transmission to mobile devices. The TCRT5000 sensor detects light reflectivity changes caused by blood flow, indirectly estimating glucose levels without the discomfort of invasive techniques. Validation was conducted by comparing system readings with a standard glucometer under varied conditions. The system achieved high performance metrics, including 97.14% accuracy, 97.9% precision, 98.59% sensitivity, and 90.91% specificity. Minor variations were observed, attributable to environmental and individual differences. Despite this, the results confirm the device's reliability and usability, making it a promising alternative for frequent and accessible glucose monitoring. Advantages include affordability, ease of use, and adaptability, which are integral to encouraging patient compliance and improving health outcomes. Future developments may incorporate advanced optical sensors such as NIR spectroscopy or Raman technologies, alongside machine learning algorithms, to improve accuracy and extend functionality. The proposed system highlights the potential for non-invasive methods to revolutionize diabetes care in both personal and clinical settings.

KEYWORDS: optical sensors, OLED, Bluetooth module

1. Introduction

Managing diabetes involves continuous blood sugar monitoring, dietary adjustments, regular exercise, and, if necessary, medication or insulin therapy. Advanced tools such as Continuous Glucose Monitoring (CGM) systems and insulin pumps have improved patient outcomes by maintaining stable glucose levels and reducing risks of hyperglycaemia or hypoglycaemia [1-3]. Personalized prevention and monitoring approaches are critical for effective management.

Diabetes complications affect multiple systems, including the eyes, kidneys, nerves, and cardiovascular system [4-7]. Common issues include diabetic retinopathy, nephropathy, neuropathy, and a higher risk of cardiovascular diseases such as myocardial infarction and stroke [8-10]. Preventing these complications requires strict glycaemic control, regular monitoring, a healthy lifestyle, patient education, and access to advanced technologies. Self-management is essential for minimizing vascular complications and premature mortality. Effective self-care combines regular glucose monitoring, adherence to treatment, and lifestyle changes, with personalized guidance improving outcomes [11-14].

Technological advancements have transitioned diabetes monitoring from invasive finger-prick methods to non-invasive CGM systems [15]. These innovations enable real-time glucose monitoring, offering critical insights for treatment adjustments. Devices like Dexcom G4 Platinum [16] and FreeStyle Libre [17] demonstrate high accuracy and user acceptance, revolutionizing diabetes care.

This paper presents the development of an intelligent, non-invasive blood glucose monitoring system using a reflective optical sensor (TCRT5000) integrated with an Arduino platform. The system

THE ANNALS OF "DUNAREA DE JOS" UNIVERSITY OF GALATI
FASCICLE IX. METALLURGY AND MATERIALS SCIENCE
Nº. 4 - 2024, ISSN 2668-4748; e-ISSN 2668-4756
Article DOI: https://doi.org/10.35219/mms.2024.4.08

comprises a detection unit with an infrared LED, a phototransistor, a microcontroller, an OLED display, and a Bluetooth module for wireless data transmission to mobile devices.

2. Experimental procedure

This research focuses on developing an intelligent system for non-invasive blood glucose monitoring. As illustrated in the block diagram (Figure 1), the glucose monitoring system comprises a detection unit and a reception unit. The components include: a development board (Arduino), illustrated in Figure 2, an OLED screen (Figure 3), a Bluetooth module (Figure 4), jumper wires (male-female and male-male connectors), breadboard and a reflective optical sensor (TCRT5000).

The detection unit consists of an infrared sensor, a microcontroller, and a Bluetooth transceiver module. The reflective optical sensor is utilized to detect the presence and variations in light reflectivity, which can be influenced by changes in blood flow. However, it does not directly measure blood glucose levels. The reception unit consists of a mobile phone with Bluetooth connectivity. The glucose sensor captures signals related to glucose variations, which are then processed by the microcontroller. The microcontroller performs signal analysis, calculation, and decision-making. It subsequently transmits the glucose level data to: the serial monitor of the Arduino IDE software, the OLED screen, and the Bluetooth module, allowing the connected mobile phone to receive the transmitted data.

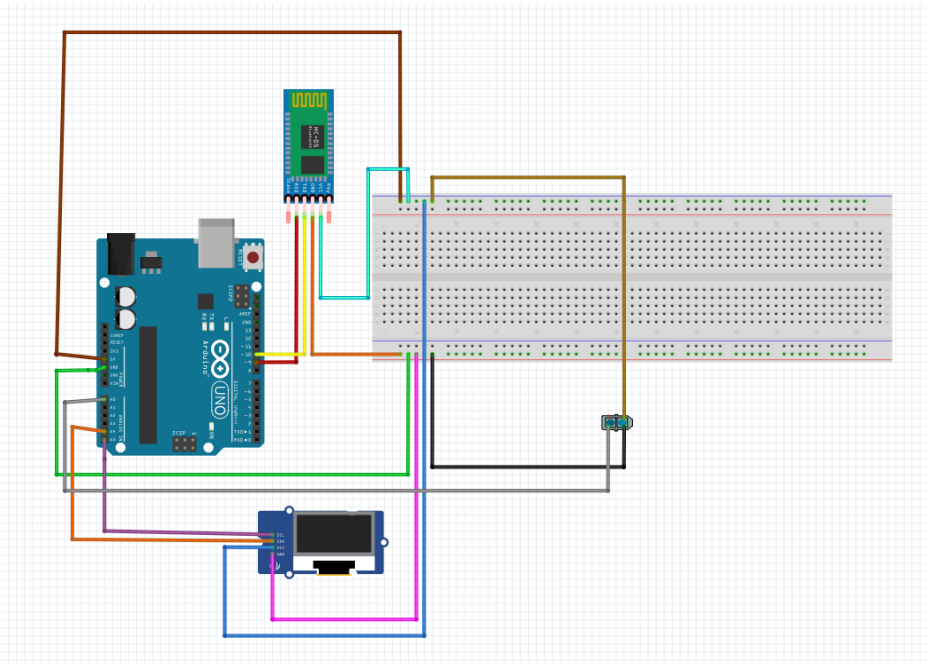

Fig. 1. *Block diagram of the proposed system architecture*

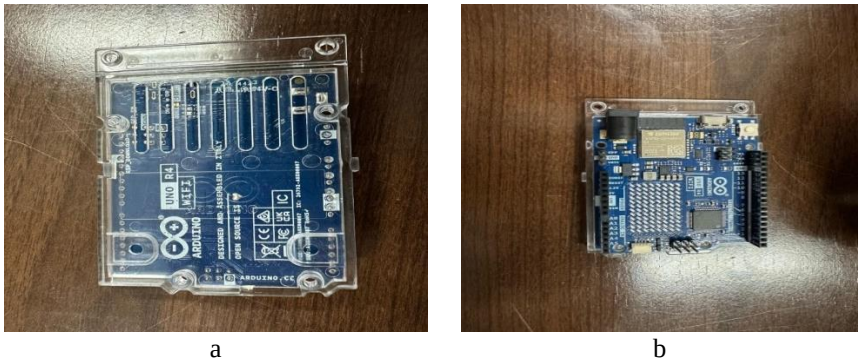

a b

Fig. 2. *Arduino UNO board: a. front side, b. back side*

THE ANNALS OF "DUNAREA DE JOS" UNIVERSITY OF GALATI
FASCICLE IX. METALLURGY AND MATERIALS SCIENCE
Nº. 4 - 2024, ISSN 2668-4748; e-ISSN 2668-4756
Article DOI: https://doi.org/10.35219/mms.2024.4.08

OLED (Organic Light Emitting Diode) technology relies on the use of organic polymers as semiconducting materials in light-emitting diodes (LEDs). These materials act like tiny particles "ready" to emit light when electrically stimulated. This innovative approach allows OLEDs to achieve high efficiency, lightweight construction, and the ability to produce flexible and thin displays, making them ideal for modern electronic devices and applications. Figure 4 shows the Bluetooth component.

a b

Fig. 3. *OLED screen: a. front side, b. back side*

a b

Fig. 4. *Bluetooth module: a. front side, b. back side*

The TCRT5000 (Figure 5) is a small yet powerful tool in the world of detection, combining the capabilities of an infrared LED and a phototransistor in a single compact body. This sensor's versatility and efficiency make it an essential component for proximity detection and reflective sensing applications.

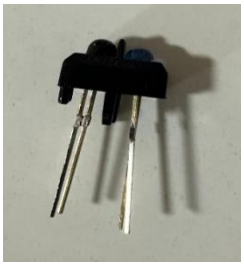

Fig. 5. *TCRT5000 sensor*

Arduino Bluetooth Control (Figure 6) is an application that gives the ability to control the Arduino board (and other similar boards) via Bluetooth, allowing to create custom projects with the new functionalities available in the application.

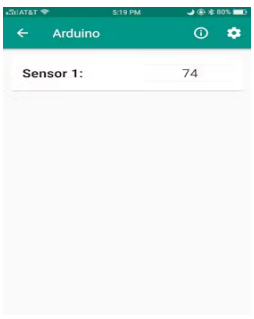

Fig. 6. *Ardutooth App Interface* [18]

THE ANNALS OF "DUNAREA DE JOS" UNIVERSITY OF GALATI
FASCICLE IX. METALLURGY AND MATERIALS SCIENCE
Nº. 4 - 2024, ISSN 2668-4748; e-ISSN 2668-4756
Article DOI: https://doi.org/10.35219/mms.2024.4.08

To activate the monitoring system using the TCRT5000 sensor and other components, they need to be connected to a development board, such as Arduino. All components are connected to the development board as shown in Figure 7. This setup ensures proper communication between components and allows for efficient data acquisition and processing within the monitoring system.

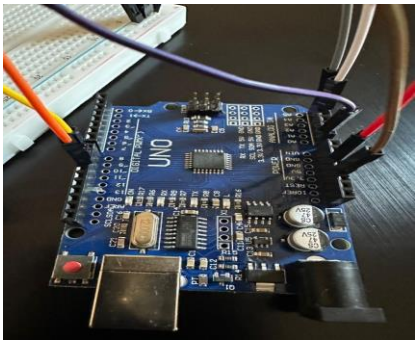

Fig. 7. *Jumper wires connected to Arduino board pins*

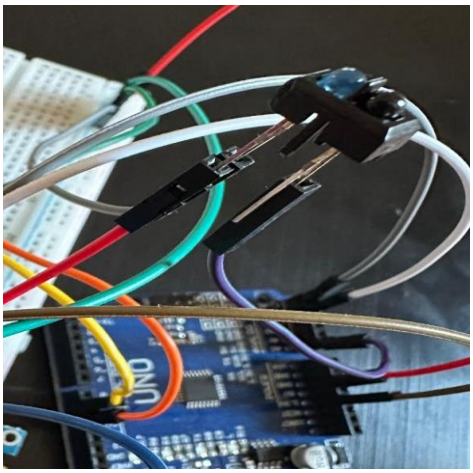

Fig. 8. *Connecting the wires to the TCRT5000 sensor*

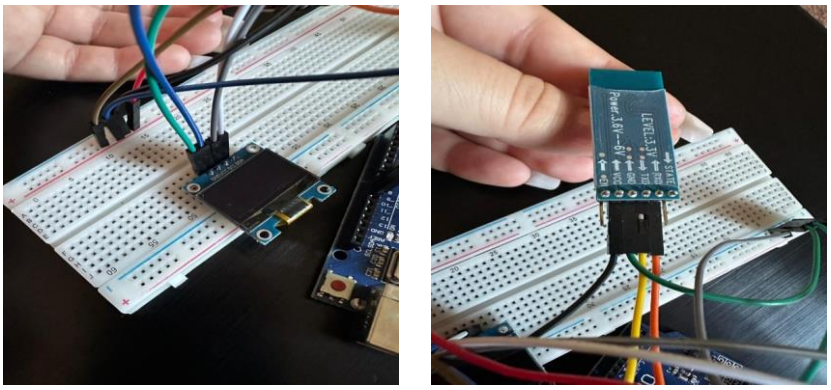

Fig. 9. *Connecting OLED screen and Bluetooth module on Breadboard*

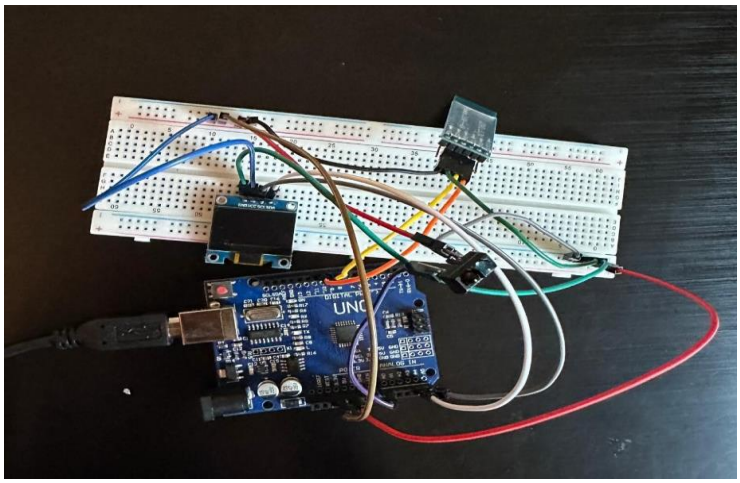

Fig. 10. *The non-invasive intelligent system for blood glucose level estimation*

THE ANNALS OF "DUNAREA DE JOS" UNIVERSITY OF GALATI
FASCICLE IX. METALLURGY AND MATERIALS SCIENCE
Nº. 4 - 2024, ISSN 2668-4748; e-ISSN 2668-4756
Article DOI: https://doi.org/10.35219/mms.2024.4.08

Once all components are connected, the next step is to link the Arduino board to a laptop using a USB cable. This connection enables both programming and powering the board by launching the Arduino IDE, the data will be displayed on the OLED screen and subsequently transmitted via Bluetooth to the corresponding mobile application (Figure 11).

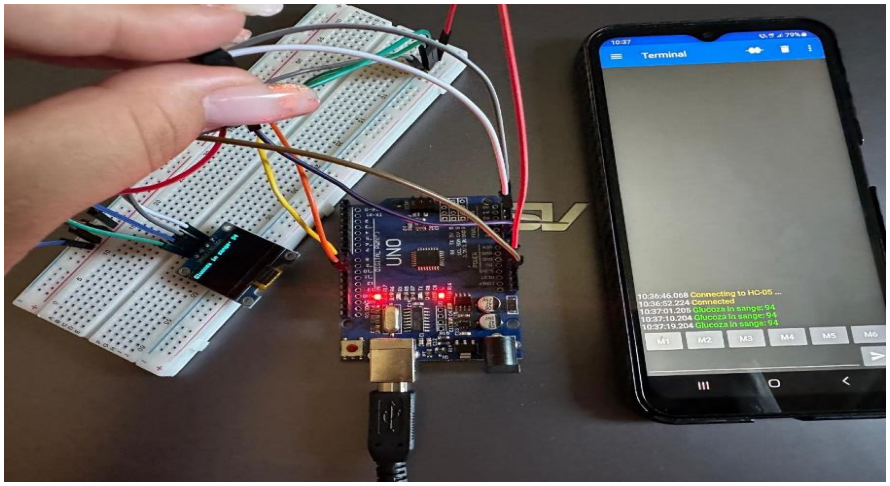

Fig. 11. *Monitoring system - screen and application display*

The TCRT5000 sensor detects any change, and the system successfully updated and transmitted the new values in real-time, both on the OLED screen and to the mobile device. This demonstrates the system's ability to monitor blood glucose fluctuations accurately and in real time.

To validate the accuracy and reliability of blood glucose monitoring device, a rigorous methodology comparing its readings to those of a standard SD glucometer under various conditions and scenarios was employed. By comparing the results from both devices, the accuracy, sensitivity, specificity, and precision of our monitoring system was evaluated. This validation method ensures that the device delivers consistent results aligned with accepted medical standards (Figure 12). After performing ten measurements using both the traditional glucometer method and our new non-invasive approach, we observed differences between the values obtained by the two devices. These results are summarized in the Table 1. The differences can be attributed to several factors: measurement accuracy (differences in the precision of each measurement method), environmental conditions: variations in light, temperature, or other external influences, individual variability due to unique physiological factors of the test subjects. A difference of ±15 mg/dL is considered acceptable for non-invasive glucose monitoring systems according to some standards, such as ISO 15197 [19].

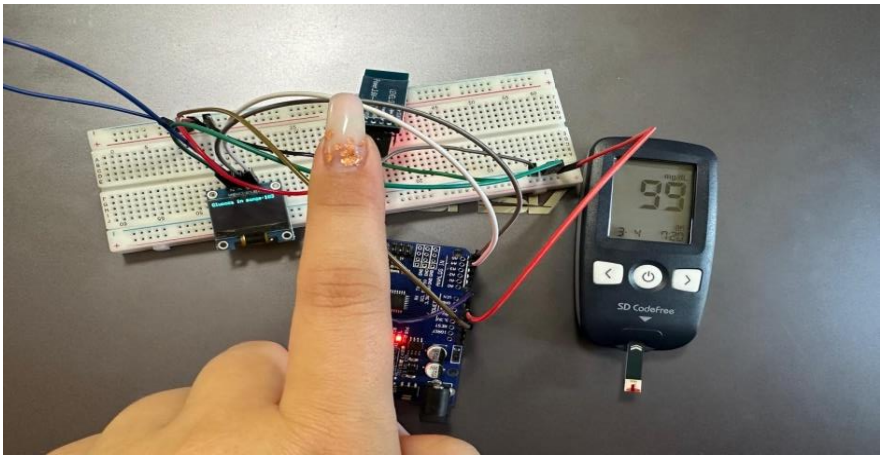

Fig. 12. *Validation of the result with the glucometer*

THE ANNALS OF "DUNAREA DE JOS" UNIVERSITY OF GALATI
FASCICLE IX. METALLURGY AND MATERIALS SCIENCE
Nº. 4 - 2024, ISSN 2668-4748; e-ISSN 2668-4756
Article DOI: https://doi.org/10.35219/mms.2024.4.08

Table 1. *Comparison between invasive and non-invasive methods*

No.	Blood glucose level (invasive method) mg/dL	Blood glucose level (non-invasive method) mg/dL	Difference
1	98	94	+4
2	100	107	-7
3	93	99	-5
4	115	108	+7
5	99	103	-4
6	91	90	+1
7	92	85	+7
8	102	100	+2
9	105	111	-6
10	94	92	+2

The system's performance metrics are summarized in Table 2, highlighting its strong potential as a reliable monitoring solution.

Table 2. *System Performance Metrics*

Metric	Performance (%)
Accuracy	97.14%
Precision	97.9%
Sensitivity	98.59%
Specificity	90.91%

4. Conclusions

The results indicate that the system accurately estimates blood glucose levels by analysing variations in light intensity reflected by blood flow, as confirmed through tests and evaluations. Utilizing a reflective optical sensor and proper coding on the Arduino board, the device demonstrated reliable performance. Additionally, an Android-based mobile application facilitates data reception and transmission via the HC-05 Bluetooth module, with glucose levels formatted as text messages.

The integration of Bluetooth connectivity ensures seamless data transfer, enhancing ease of use for glucose monitoring and management. The results also highlight the potential for future enhancements, such as replacing the TCRT5000 sensor with advanced optical technologies as NIR spectroscopy or Raman sensors, combined with machine learning algorithms, to improve accuracy and efficiency. This evolution could make the system suitable for continuous patient monitoring in clinical settings.

The non-invasive approach, validated by the obtained results, eliminates the discomfort associated with traditional methods, encouraging frequent usage and better health outcomes. The system's affordability and the flexibility of the Arduino platform further support its adaptability for broader applications and customization to meet specific user requirements.

References

[1]. Weinstock R. S., *et al.*, *The Role of Blood Glucose Monitoring in Diabetes Management*, Arlington (VA): American Diabetes Association, 2020.
[2]. Miller E. M., *Using Continuous Glucose Monitoring in Clinical Practice*, Clin Diabetes, 38 (5), p. 429-438, 2020.
[3]. Schubert-Olesen O., Kröger J., Siegmund T., Thurm U., Halle M., *Continuous Glucose Monitoring and Physical Activity*, Int. J. Environ. Res. Public Health, 19, 12296, 2022.
[4]. Kulkarni A., Thool A. R., Daigavane S., *Understanding the Clinical Relationship Between Diabetic Retinopathy, Nephropathy, and Neuropathy: A Comprehensive Review*, Cureus, 21, 16 (3), 2024.
[5]. Lee R., Wong T. Y., Sabanayagam C., *Epidemiology of diabetic retinopathy, diabetic macular edema and related vision loss*, Eye and vision, 2, p. 1-25, 2015.
[6]. Zang B., *et al.*, *The impact of diabetic retinopathy on vision-related quality of life*, [Zhonghua yan ke za Zhi] Chinese Journal of Ophthalmology, 58 (10), p. 760-768, 2022.
[7]. Zhang J., *et al.*, *Diabetic macular edema: current understanding, molecular mechanisms and therapeutic implications*, Cells, 11 (21), 3362, 2022.
[8]. Cade W. T., *Diabetes-related microvascular and macrovascular diseases in the physical therapy setting*, Phys Ther., 88 (11), 1322-1335, 2008.
[9]. Zakir M., *et al.*, *Cardiovascular Complications of Diabetes: From Microvascular to Macrovascular Pathways*, Cureus, 24, 15 (9), 2023.
[10]. Li Y., *et al.*, *Diabetic vascular diseases: molecular mechanisms and therapeutic strategies*, Sig Transduct Target Ther 8, 152, 2023.
[11]. Lee E. Y., *et al.*, *Efficacy of Personalized Diabetes Self-care Using an Electronic Medical Record-Integrated Mobile App in Patients with Type 2 Diabetes: 6-Month Randomized Controlled Trial*, J Med Internet Res., 28, 24 (7), 2022.
[12]. Ahmad F., Joshi S. H., *Self-Care Practices and Their Role in the Control of Diabetes: A Narrative Review*, Cureus, 5, 15 (7), 2023.
[13]. Nuha A. ElSayed, *et al.*, *Diabetes Technology: Standards of Care in Diabetes-2023*, Diabetes Care, 46, S111-S127, 2023.
[14]. Mohammad Mansour, *et al.*, *Wearable devices for glucose monitoring: A review of state-of-the-art technologies and emerging trends*, Alexandria Engineering Journal, vol. 89, p. 224-243, 2024.
[15]. Rosilla Edward, Ronny Priefer, *A comparison of continuous glucose monitors (CGMs) in diabetes management: A systematic*

literature review, Primary Care Diabetes, vol. 17, issue 6, p. 529-534, 2023.
[16]. Taleb Nadine, *et al.*, *Dexcom G4 Platinum and Medtronic Enlite Glucose Sensors Perform Equally Well during Exercise in Patients with Type 1 Diabetes*, A46-A46, 2015.
[17]. Al Hayek A. A., Robert A. A., Al Dawish M. A., *Effectiveness of the Freestyle Libre Flash Glucose Monitoring System on Diabetes Distress Among Individuals with Type 1 Diabetes: A Prospective Study*, Diabetes Ther., 11 (4), p. 927-937, 2020.
[18]. ***, https://ardutooth.en.aptoide.com/app.
[19]. Jendrike N., *et al.*, *ISO 15197: 2013 Evaluation of a Blood Glucose Monitoring System's Measurement Accuracy*, J Diabetes Sci Technol., 11 (6), p. 1275-1276, 2017.

THE ANNALS OF "DUNAREA DE JOS" UNIVERSITY OF GALATI
FASCICLE IX. METALLURGY AND MATERIALS SCIENCE
Nº. 4 - 2024, ISSN 2668-4748; e-ISSN 2668-4756
Article DOI: https://doi.org/10.35219/mms.2024.4.09

SIMULATION OF THE FORGING PROCESS OF A BEARING RING USING MATLAB SOFTWARE

Marian-Iulian NEACȘU
"Dunarea de Jos" University of Galati, Romania
e-mail: mneacsu@ugal.ro

ABSTRACT

In the current work, entitled "Simulation of the forging process of a bearing ring using MATLAB", we created a graphical interface (GUI) using MATLAB software, based on the mathematical relationships specific to the forging process of metallic materials.

By simulating the technological process of obtaining the bearing rings, the material and energy consumption conditions are precisely calculated and highlighted, for the realization of the different profiles of the bearing ring generator.

KEYWORDS: forging, modeling, MATLAB, graphic interface, bearing rings

1. Introduction

The first wrought metals were gold, bronze, and iron, used to make tools, weapons, and jewellery. Later, steel was introduced, and all of these metals were worked using a rock as a hammer, along with the heat generated by fire. This method remained the predominant method for forging metals and steel until the early 19th century [1-3].

The forging of iron and other metals has been vital to the development of human civilizations for millennia. The ability to shape and work metals through forging was a significant step in technological progress since the Bronze and Iron Ages. This process is still as important today [2].

Providing a wide range of essential products, such as metal pipes and fittings, as well as sheet metal and profiles needed in various other industrial sectors, forging is often considered the "heart" of the metalworking industry. These robust and durable parts, obtained by controlled plastic deformation of metal, are essential to contemporary industrial infrastructure [3-5].

Forging is the process by which metal is hammered, pressed, or rolled into a specific shape. This can be achieved either with a hammer, a press, or a die. Essentially, it is the art of heating and working hot metal to obtain a specific design or shape for a specific purpose or use [6-9].

Many of the properties of the material, such as structure, conductivity, and longevity, are improved by machining.

Forging creates parts that have superior mechanical properties with minimal material loss. The starting material, which has a relatively simple geometry, is plastically transformed in one or more ways to create a fairly complex product. Forging usually requires quite expensive tools [10-12].

Simulation of a technological process in general consists of rendering its development based on mathematical models that describe the respective process, with the aim of highlighting the evolution of factors that characterize the final products and the technological process [13, 14].

Recently, virtual simulation has experienced extensive development, this is also due to the advantages that this type of simulation involves, namely: low material costs, does not require the use of tools, devices, installations, does not require energy consumption, does not require measuring equipment, does not pollute the environment etc. [14, 15].

2. Experimental conditions

In this work, a simulation of the process of obtaining rings of various sizes for bearings by forging was carried out using the MATLAB software.

When creating the MATLAB program that makes this simulation possible, all the mathematical expressions specific to the forging process were used.

The creation of the graphical interface for simulating the process of obtaining rings for bearings had as restrictive conditions the fact that the case was

THE ANNALS OF "DUNAREA DE JOS" UNIVERSITY OF GALATI
FASCICLE IX. METALLURGY AND MATERIALS SCIENCE
Nº. 4 - 2024, ISSN 2668-4748; e-ISSN 2668-4756
Article DOI: https://doi.org/10.35219/mms.2024.4.09

taken into account when: The height of the ring (Hinel) is less than or equal to the height of the semi-finished product (Hs).

The simulation of the process of obtaining bearing rings by forging includes the following stages:

Stage I - Initiation of the program made in MATLAB for displaying the Graphical Interface.

Stage II - Choosing the dimensions for the bearing ring.

Stage III - Simulating the mould extrusion.

Stage IV - Simulating the drilling of the semi-finished product.

Stage V - Rolling the rings.

3. Simulation results

Figures 1-6 show images with the graphical interface for simulating the bearing ring extrusion. Figure 1 shows the graphical interface at the beginning of the simulation. Figure 2 shows the graphical interface at the time of choosing the dimensions of the rings to be made. Figure 3 illustrates the extrusion stage of the mould (semi-finished product) from which, in the final stage, the bearing ring will be obtained by rolling. After completing the blank pressing stage, the simulation program also calculates the dimensions of the blank drilling mandrel, which are obviously based on the dimensions of the blank pressed.

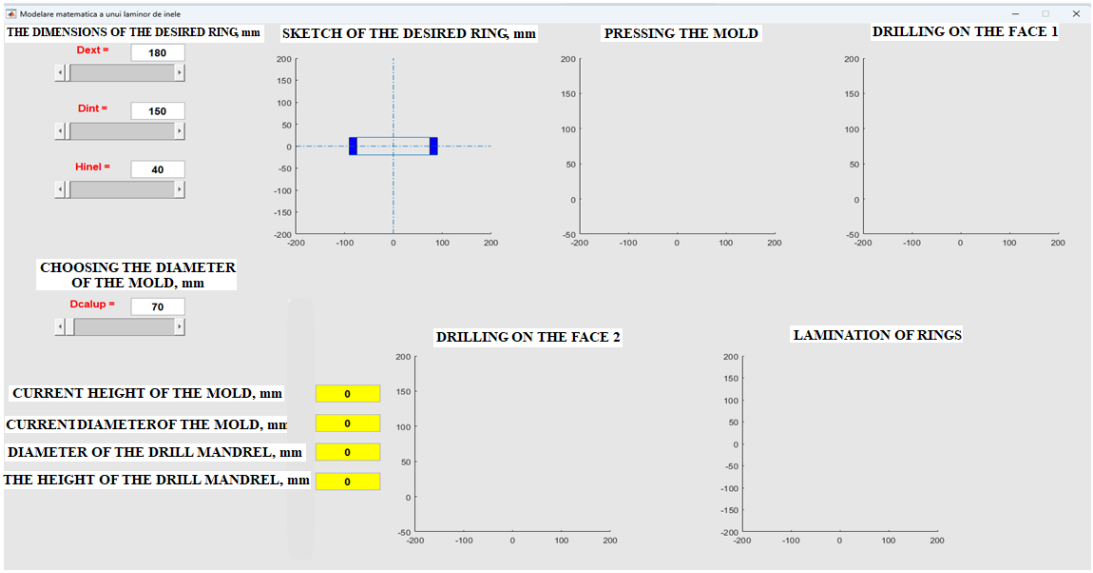

Fig. 1. *Stage I - Initiation of the program created in MATLAB for displaying the Graphical Interface*

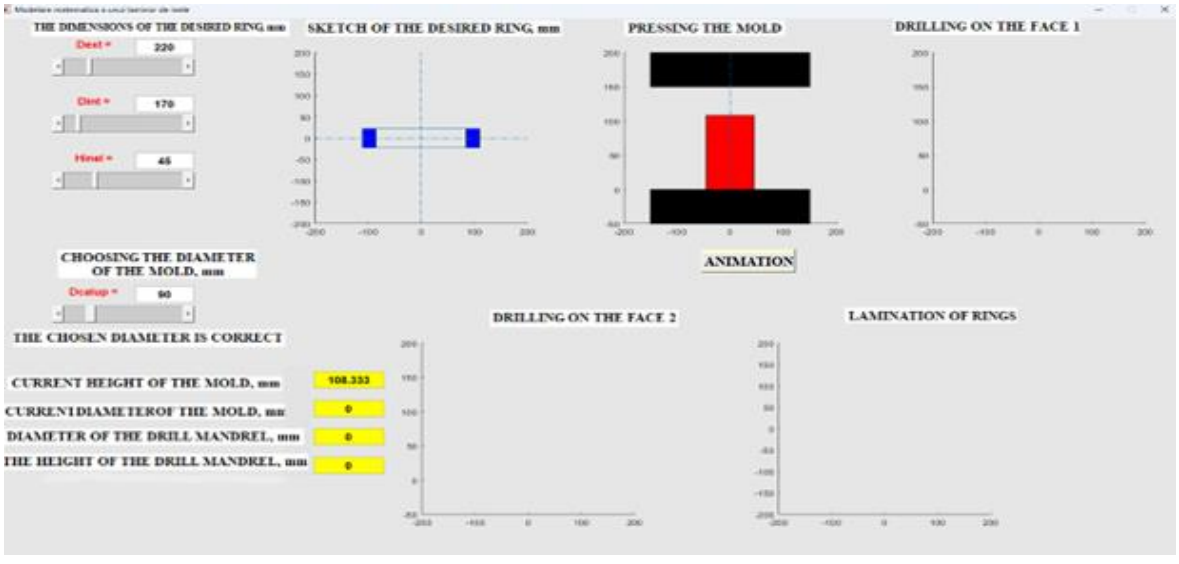

Fig. 2. *Stage II – Choosing the dimensions for the bearing ring*

THE ANNALS OF "DUNAREA DE JOS" UNIVERSITY OF GALATI
FASCICLE IX. METALLURGY AND MATERIALS SCIENCE
Nº. 4 - 2024, ISSN 2668-4748; e-ISSN 2668-4756
Article DOI: https://doi.org/10.35219/mms.2024.4.09

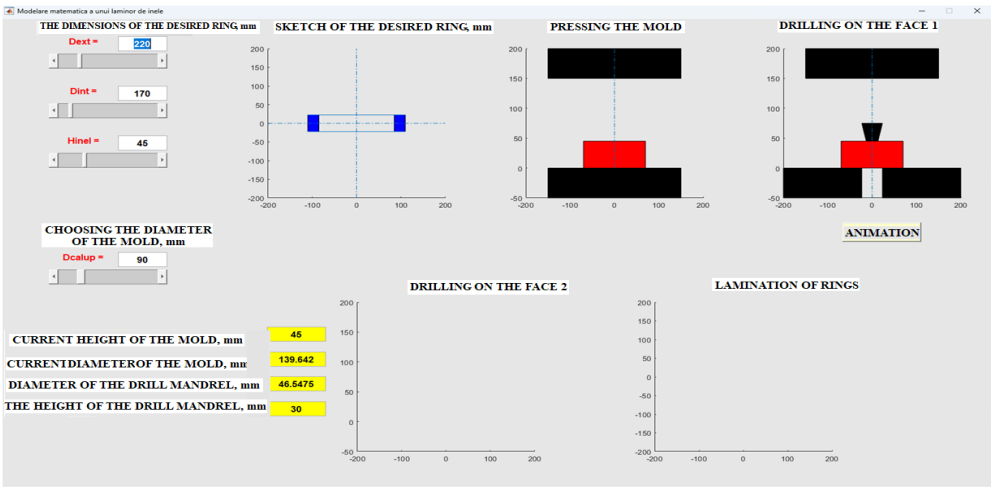

Fig. 3. *Stage III – Simulation of mold release*

Figure 4 and Figure 5 show the simulation of the drilling stage of the semi-finished product using the mandrel, in figure 4 drilling on face 1 and in figure 5 drilling on face 2.

In figure 6 the graphical interface shows the last stage in the simulation of the rolling process of bearing rings.

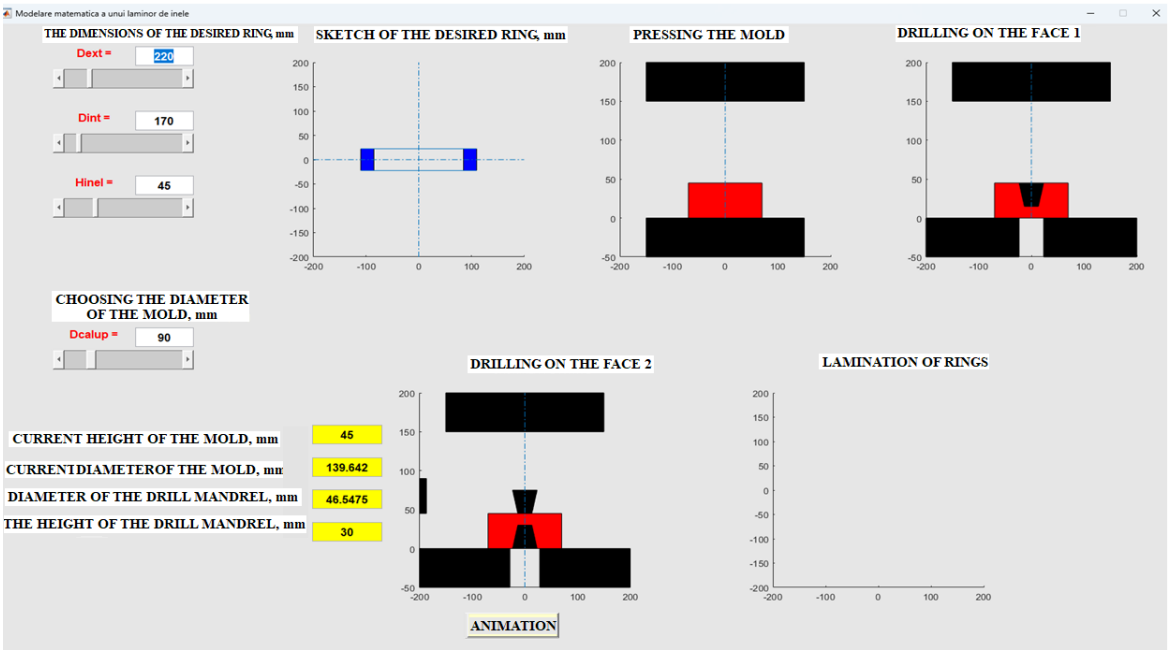

Fig. 4. *Stage IV – Simulating drilling of the blank (side 1)*

THE ANNALS OF "DUNAREA DE JOS" UNIVERSITY OF GALATI
FASCICLE IX. METALLURGY AND MATERIALS SCIENCE
Nº. 4 - 2024, ISSN 2668-4748; e-ISSN 2668-4756
Article DOI: https://doi.org/10.35219/mms.2024.4.09

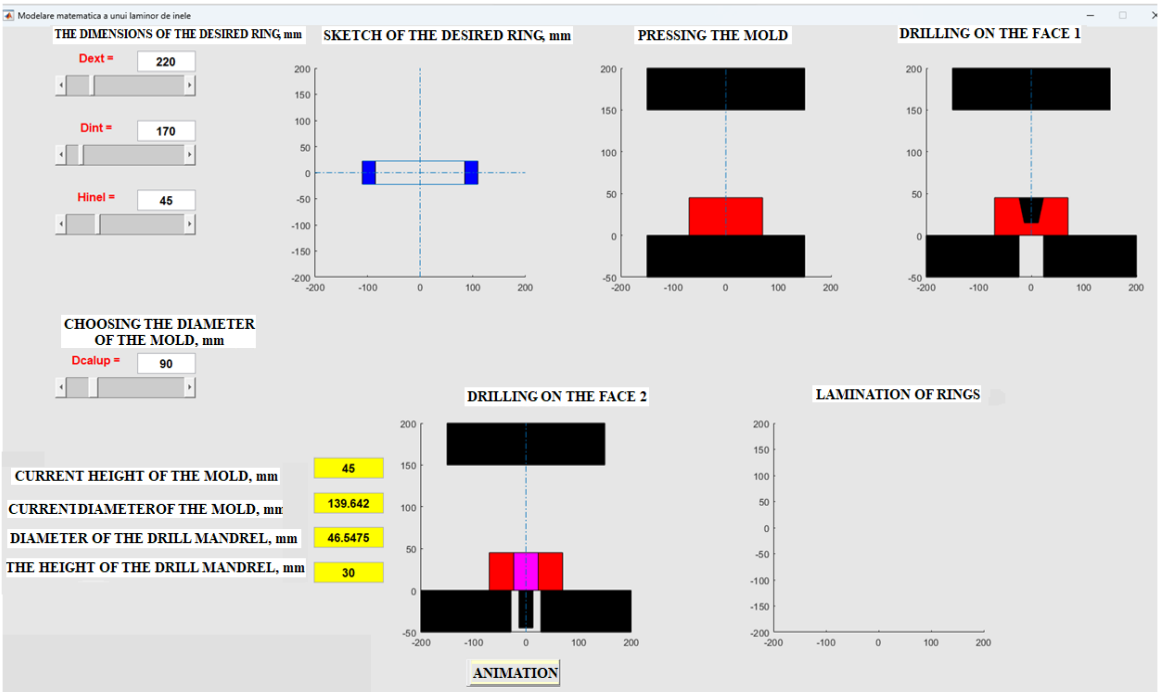

Fig. 5. *Stage IV – Simulating drilling of the blank (side 2)*

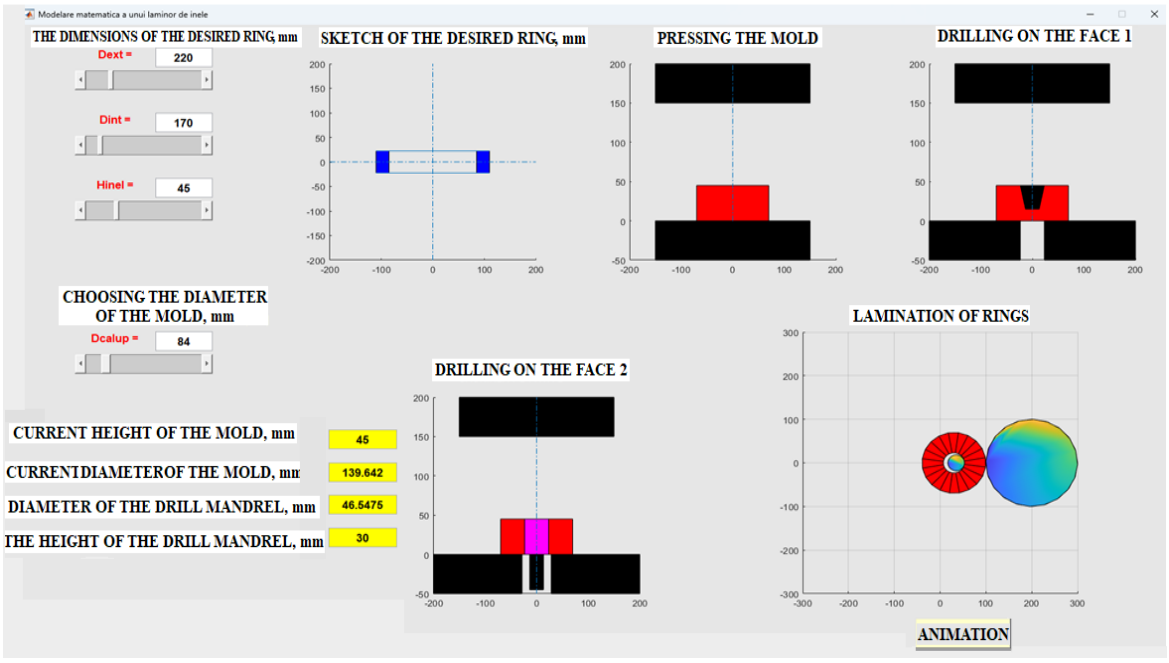

Fig. 6. *Stage V – Ring rolling*

4. Conclusions

Analytical and virtual simulation of a process, carried out using a computer and specialized programs, is based on the transposition of mathematical models into simulation software.

The advantages of both virtual and analytical simulations are:

- low material costs;
- does not require the use of tools, devices, installations;
- does not require energy consumption;
- does not require measuring equipment;
- does not pollute the environment, etc.

By simulating the rolling process of bearing rings, the user can control the process with greater

THE ANNALS OF "DUNAREA DE JOS" UNIVERSITY OF GALATI
FASCICLE IX. METALLURGY AND MATERIALS SCIENCE
Nº. 4 - 2024, ISSN 2668-4748; e-ISSN 2668-4756
Article DOI: https://doi.org/10.35219/mms.2024.4.09

precision, which leads to obtaining rings of better dimensional accuracy.

Also, by simulating the process, material losses can be prevented because through simulation, precise data regarding the dimensions of the initial semi-finished product from which the bearing ring is finally obtained is obtained. By avoiding material losses, energy savings can also be made.

The simulation of rolling of bearing rings allows highlighting the material requirements and energy consumption conditions for creating different profiles of the bearing ring generator.

References

[1]. ***, https://www.wasatchsteel.com/the-history-of-steel-and-metal-forging-part-1/.
[2]. ***, https://en.m.wikipedia.org/wiki/Forging.
[3]. ***, https://www.tfgusa.com/metal-forging-processes-methods/.
[6]. ***, https://www.iqsdirectory.com/articles/forging.html.
[7]. ***, https://typeset.io/search?q=forging.
[8]. ***, https://www.reliance-foundry.com/blog/forging.
[9]. ***, https://www.linkedin.com/pulse/forging-future-brief-overview-metal-industry maintenance world-com-xdfue.
[10]. ***, https://www.somersforge.com/what-is-forging/.
[11]. ***, https://www.scribd.com/doc/90995816/Forjarea-Metalelor.
[12]. ***, https://www.zx-hydraulic.com/news/free-forging-and-die-forging/.
[13]. Taloi D., *Optimizarea proceselor tehnologice – aplicaţii în metalurgie*, Editura Academiei, Bucureşti, 1987.
[14]. Popescu D., Ionescu F., Dobrescu R., Ştefanoiu D., *Modelare în ingineria proceselor industriale*, Editura AGIR, Bucuresti, 2011.
[15]. Ciucă I., Dumitriu S., *Modelarea şi Optimizarea Proceselor Metalurgice de Deformare Plastică şi Tratamente Termice*, Editura Didactică şi Pedagogică, Bucureşti, 1998.

THE ANNALS OF "DUNAREA DE JOS" UNIVERSITY OF GALATI
FASCICLE IX. METALLURGY AND MATERIALS SCIENCE
Nº. 4 - 2024, ISSN 2668-4748; e-ISSN 2668-4756
Article DOI: https://doi.org/10.35219/mms.2024.4.10

THE INFLUENCE OF THERMOMECHANICAL TREATMENTS ON THE MECHANICAL PROPERTIES OF SOME AL-Zn-Mg-Cu ALLOYS

Marian-Iulian NEACȘU
"Dunarea de Jos" University of Galati, Romania
e-mail: marian.neacsu@ugal.ro

ABSTRACT

In this paper, the variation of some mechanical properties was studied according to the values of the thermomechanical processing parameters to which an aluminium alloy of the Al-Zn-Mg-Cu series was subjected.

Thermomechanical processing consisted of a cold plastic deformation followed by an artificial aging performed at various treatment temperature values and various maintenance time values.

Following the application of this thermomechanical processing variant, it can be concluded that the values obtained for the studied mechanical characteristics are closely related to the values of the thermomechanical processing parameters.

KEYWORDS: aluminium alloys, thermomechanical treatment, artificial aging, temperature, holding time

1. Introduction

Al-Zn-Mg-Cu alloys belong to the category of deformable and hardened aluminium alloys. Alloys in the Al-Zn-Mg-Cu system depending on the chemical composition may end up having outstanding mechanical properties, being comparable to Cu alloys or even some steel brands, however, they have the advantage of having a lower density [1].

The presence of alloying elements influences the technological and operational characteristics of Al-Zn-Mg-Cu alloys. Thus, silicon contributes to the increase of mechanical strength, reduces ductility as well as fatigue resistance and influences the behaviour to heat and thermomechanical treatment; magnesium also increases, mechanical strength and hardness but also influence the behaviour to heat treatment. In alloys where Si and Mg are also present, the behaviour to heat treatment depends on the Mg/Si ratio, thus, if this ratio has a high value, then by natural aging the best properties of strength and plasticity are obtained, at a lower ratio artificial aging is required. If iron is also present in the composition of the alloy, at contents below 0.7%, it increases hot stability, in some alloys, producing fragility due to the appearance of its compounds in other alloys [2].

The presence of manganese in these alloys has a hardening effect (each percentage of manganese increases the hardness by 2-3 daN/mm^2) and reduces the brittle effect of iron and finishes the grain. Nickel like manganese has a hardening effect, but more limited and reduces the brittle effect of iron. The main effect of nickel alloying is manifested by increased high temperature resistance, fatigue resistance and creep. Titanium finishes the grain by increasing the tenacity, lithium has a similar effect to magnesium, zinc increases the mechanical strength but decreases the plasticity and chromium increases the resistance to high temperatures [2, 3].

From the experiments made, thermomechanical processing was found to lead to obtaining superior values of the main mechanical properties, and so this method of processing these alloys should be used in practice more than conventional methods [4, 5].

The metallurgical technologies used for special alloys of Al in terms of the size of the finished grain and achieving medium or high strength are of two kinds [6-8]:

1. technological processing that acts on the size of the crystallized grain of some aluminium alloys during the first phases of processing at high temperatures by partially eliminating the structural heterogeneity, by controlling the chemical composition, the casting and homogenization cycles of these alloys. Next, the hot plastic deformation is applied, finally obtaining a recrystallized structure with fine and uniform grains in size.

2. technological processing applied to high-strength alloys, especially those used in the aviation industry. It consists of several stages of plastic deformation and heat treatment, which is

THE ANNALS OF "DUNAREA DE JOS" UNIVERSITY OF GALATI
FASCICLE IX. METALLURGY AND MATERIALS SCIENCE
Nº. 4 - 2024, ISSN 2668-4748; e-ISSN 2668-4756
Article DOI: https://doi.org/10.35219/mms.2024.4.10

thermomechanical processing. In the practice of metallurgical processing, it is found intermediate thermomechanical processing and final thermomechanical processing [9-11].

Generally, intermediate thermomechanical processing is used internationally to improve the plasticity, hardness and corrosion resistance of special aluminium alloys without reducing mechanical strength compared to conventional processing.

The final thermomechanical processing is used to obtain the final strength characteristics combined with good plasticity, corrosion resistance and fatigue resistance.

Alloys in this system are divided into [10]:

1. high-strength alloys, for which the amount (Zn + Mg + Cu) is more than 10%.
2. medium-strength alloys with amount (Zn + Mg + Cu) = 7-9%.
3. alloys with low resistance, for which the amount (Zn + Mg + Cu) is less than 6%.

The high strength of these alloys is achieved after a heat treatment of natural or artificial hardening [11-13].

2. Conditions of experimental research

Experiments were carried out on alloy samples with the chemical composition indicated in Table 1, alloy of the alloy family: Al-Zn-Mg-Cu.

The mechanical properties of the alloy according to EN 485-2-2007 are shown in Table 2.

Table 1. *Chemical composition of the alloy studied*

Alloy	**Cu**	**Zn**	**Cr**	**Fe**	**Mn**	**Si**	**Mg**	**Al**
	0.75	4.3	0.25	0.5	0.17	0.5	2.6	Rest

Table 2. *Alloy properties according to EN 485-2-2007*

Elemental / **Alloy**	**Rm, [MPa]**	**$Rp_{0,2}$ [MPa]**	**A_5 [%]**	**HB**
AlZn4.3Mg2.6Cu	430	370	8	130

Figure 1 shows the sequence of heat and thermomechanical treatment operations, to which the samples from the alloy studied have been subjected. Specific to this variant is the thermomechanical treatment with cold plastic deformation performed between the two artificial aging [14].

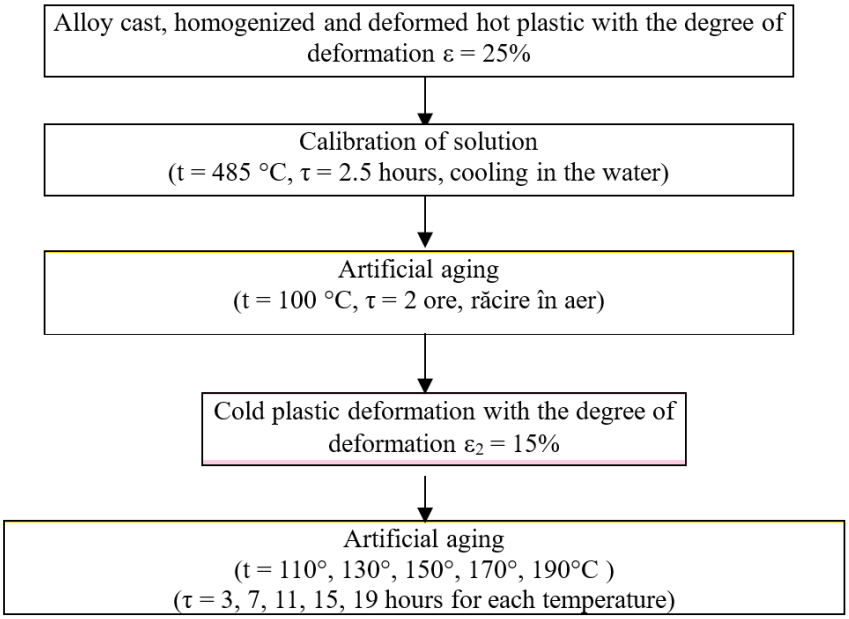

Fig. 1. *Experimental conditions of thermomechanical treatments* [14]

THE ANNALS OF "DUNAREA DE JOS" UNIVERSITY OF GALATI
FASCICLE IX. METALLURGY AND MATERIALS SCIENCE
N°. 4 - 2024, ISSN 2668-4748; e-ISSN 2668-4756
Article DOI: https://doi.org/10.35219/mms.2024.4.10

For structural stabilization of the material, after quenching the solution, an artificial aging with a one-hour maintenance time at 100 °C is carried out. Further, a cold plastic deformation takes place where the samples are deformed with a degree of plastic deformation 15%, in order to reach the established dimensions.

After plastic deformation, an artificial aging is performed at the following temperatures: T_1 = 110 °C, T_2 = 130 °C, T_3 = 150 °C, T_4 = 170 °C and T_5 = 190 °C having these temperatures: τ_1 = 3 hours, τ_2 = 7 hours, τ_3 = 11 hours, τ_4 = 15 hours, τ_5 = 19 hours.

After performing thermomechanical processing, the samples from the alloy studied were subjected to tensile and hardness tests for finding out the values of the mechanical properties (mechanical resistance, flow limit, elongation at breaking and hardness).

Cold plastic deformation accelerates and intensifies the processes of hardening by aging. Cold rolling is aimed on the one hand at increasing the hardness of the material as well as creating favourable conditions for the occurrence of precipitation around dislocations at the next artificial aging. At the same time, this deformation brings the blank to the final size [10, 14].

3. Experimental results

For the analysis of the results and the formulation of conclusions, graphical representations were used that mainly illustrate the influence of technological parameters of aging (age temperature and maintenance time) on the main mechanical properties of the alloy studied belonging to the Al-Zn-Mg-Cu system.

Putting into practice the technological operations according to the processing variant of the alloy investigated, a series of values of the mechanical properties whose values vary depending on the time and temperature of the treatment were obtained.

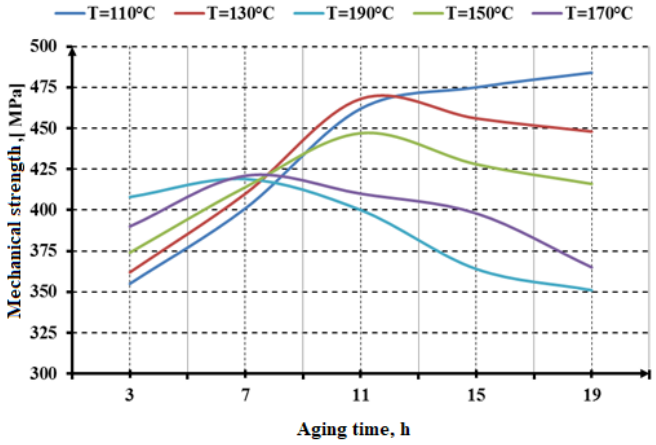

Fig. 2. *The influence of maintenance time on artificial ageing mechanical strength for the alloy studied*

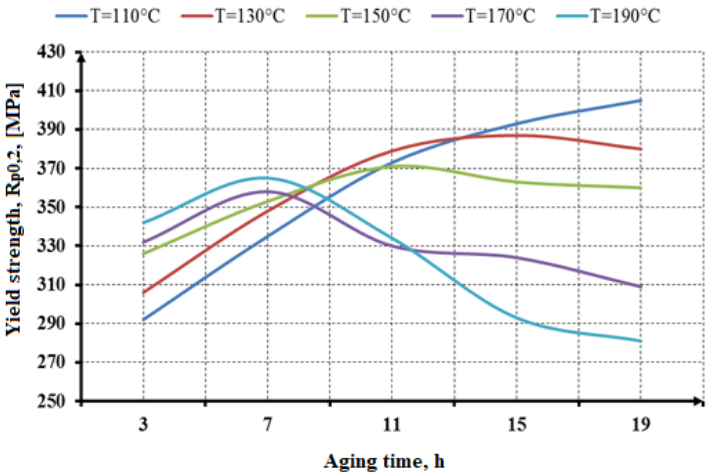

Fig. 3. *The influence of maintenance time on artificial ageing flow limit for the alloy studied*

THE ANNALS OF "DUNAREA DE JOS" UNIVERSITY OF GALATI
FASCICLE IX. METALLURGY AND MATERIALS SCIENCE
Nº. 4 - 2024, ISSN 2668-4748; e-ISSN 2668-4756
Article DOI: https://doi.org/10.35219/mms.2024.4.10

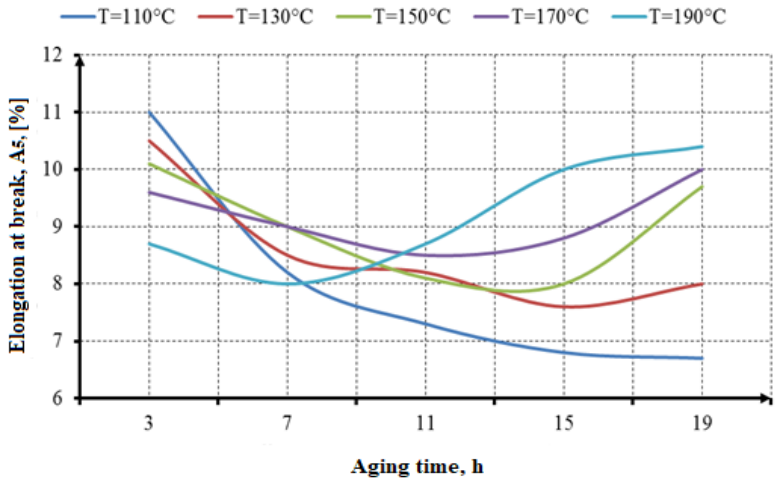

Fig. 4. *The influence of maintenance time on artificial ageing elongation at break for the alloy studied*

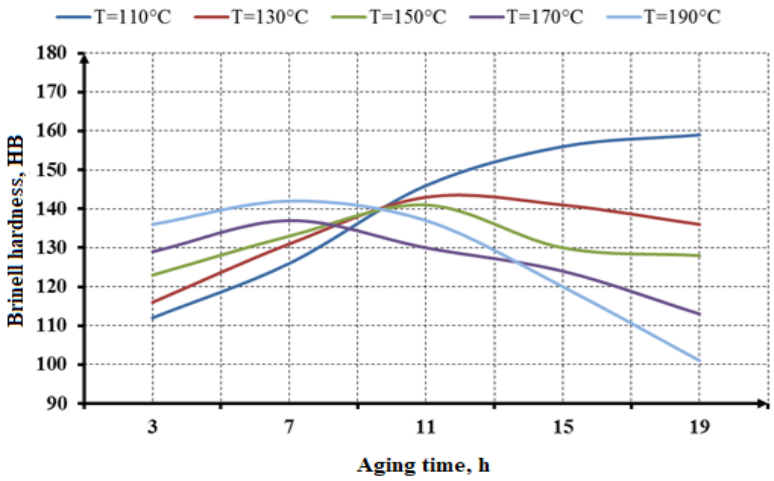

Fig. 5. *The influence of maintenance time on artificial ageing Brinell hardness for alloy studied*

Figure 2 illustrates that as the aging temperature rises, for maintenance times of 3 and 7 hours, an increase in the value of mechanical strength also occurs. For temperatures of 110 °C, 130 °C and 150 °C, mechanical strength values increase only up to and including 11 hours of maintenance. For temperatures of 170 °C and 190 °C, a decrease in strength is observed.

At 110 °C the maximum resistance value shall be recorded for the holding time of 19 hours. Thermal processing at temperatures of 130 °C and 150 °C, leads to a maximum of strength values for a time of 11 hours of aging. For temperatures of 170 °C and 190 °C the mechanical strength has a maximum at a time of 7 hours of treatment.

The process of hardening these structures, according to the literature, is, it occurs by the occurrence of the phenomenon of precipitation and consists in the formation of chemical compounds between the chemical elements that are present and dissolved in the composition of the alloy being studied. After the quenching stage of putting into solution when a solid aluminium solution is obtained, which is supersaturated by dissolving as many alloying elements as possible, aging occurs by precipitation of new formed chemical compounds, which have as activation energy, as the driving force of their formation, the heat from the temperature of artificial aging treatment.

Once these compounds have formed, the phenomenon of their coalescence occurs, if the alloy is kept for too long at the temperature of aging. The coalescence of these compounds has the effect of a decrease in the mechanical strength properties of the alloy that has undergone these thermal processing. This explains the decrease in the strength properties of the alloy studied as the artificial aging temperature

THE ANNALS OF "DUNAREA DE JOS" UNIVERSITY OF GALATI
FASCICLE IX. METALLURGY AND MATERIALS SCIENCE
N°. 4 - 2024, ISSN 2668-4748; e-ISSN 2668-4756
Article DOI: https://doi.org/10.35219/mms.2024.4.10

rises above 150 °C and for holding times of more than 7 hours.

For the flow limit and for the hardness things are mostly the same as for the mechanical strength.

The elongation at breaking has a minimum and a maximum at the temperature of 110 °C, the minimum is obtained for the 19-hour aging time and the maximum for the 3-hour aging time. In the case of the other values of the considered thermomechanical processing parameters, the elongation is inversely proportional to the mechanical resistance.

Following the processing of the alloy, the values obtained for the mechanical strength are higher values or at least equal to those imposed by the euro norm EN 485-2-2007, which is, for variants where the treatment temperature was 110 °C, 130 °C and 150 °C with artificial aging times of 11 hours, 15 hours and 19 hours, respectively, last less for the temperature of 150 °C. Similarly, the situation is also presented for the hardness and flow limit of the alloy studied.

The elongation at breaking was higher or equal to those prescribed by the euro norm EN 485-2-2007, for most experimental variants, except for the following combinations of treatment time and temperature:

- for the temperature of 110 °C at times of 11 hours, 15 hours and 19 hours;
- for the temperature of 130 °C on 15 hours and 19 hours;
- for the temperature of 150 °C at the time of 19 hours.

4. Conclusions

The study of the influence of thermal processing on the most important mechanical properties of aluminium-based alloy in the Al-Zn-Mg-Cu system studied in this paper led to the following conclusions:

1. Since the alloys of the Al-Mg-Zn-Cu system are alloys sensitive to thermomechanical treatments, superior values of mechanical strength result with the preservation at a convenient level of plasticity characteristics.

2. For the alloy studied, the maximum value of the mechanical properties is recorded when the final artificial aging treatment is carried out at a holding time equal to 19 hours at a temperature of 110 °C.

3. Cold plastic deformation between the two applied artificial aging causes a sharp increase in the values of mechanical characteristics (hardness and mechanical strength).

4. At ageing temperatures below 190 °C and for ageing times less than or equal to 11 hours, the increase in the duration of maintenance on ageing results in increased hardness for the alloy studied.

5. For the alloy studied, at the aging temperature of 170 °C and for ageing times longer than 7 hours, the increase in the maintenance time to aging causes the hardness to decrease.

6. The alloy under investigation records an increase in hardness directly proportional to the final artificial aging time for the treatment temperature of 110 °C.

7. By applying the thermomechanical treatment scheme of this paper, the obtained values for mechanical strength were higher or at least equal to those imposed by the euro norm EN 485-2-2007, for situations where the treatment temperature was 110 °C, 130 °C and 150 °C with aging times of 11 hours, 15 hours and 19 hours.

References

[1]. Ioan Fara, *Aluminiul de la materia primă la produse finite*, Editura Tehnică, 2000.
[2]. Rajiv S. Mishra, Mageshwari Komarasamy, *Friction Stir Welding of High Strength 7XXX Aluminum Alloys*, 1st Edition, ISBN: 9780128094655, June 8, 2016.
[3]. Rajiv S. Mishra, Harpreet Sidhar, *Friction Stir Welding of 2XXX Aluminum Alloys including Al-Li Alloys*, 1st Edition, Paperback ISBN: 978012805368, eBook ISBN: 9780128092927, 2016.
[4]. Marian Neacsu, Doru Hanganu, Elisabeta Vasilescu, *Mathematical modeling of thermomechanical treatment process applied to aluminum base alloys for aeronautics*, Analele Universitatii „Dunarea de Jos" din Galati, Fascicula IX Metalurgie si Stiinta Materialelor, ISSN 1453-083X, nr. 4/2011.
[5]. Vasilescu E., Neacsu M., Drugescu E., *International Researches Concerning the Influence of Heat Treatment on Physical and Mechanical Properties of Alluminium Based Alloys*, Conference TEME 2011 New Trends in Environmental and Materials Engineering, Galati, Romania, May 18-20 2011.
[6]. Gâdea S., Petrescu M., *Metalurgie fizica si Studiul metalelor*, Partea a II a, Bucuresti, Editura didactica si pedagogica, 1981.
[7]. Gâdea S., Petrescu M., *Metalurgie fizica si Studiul metalelor*, Partea a III a, Bucuresti, Editura didactica si pedagogica, 1983.
[8]. ***, *Metals Handbook, Non-Ferrous metals*, Ohio, 1999.
[9]. Vermeşan G., *Tratamente termice*, Editura Dacia, Cluj-Napoca,1997.
[10]. Ienciu M., *et al.*, *Elaborarea şi turnarea aliajelor neferoase speciale*, Editura Didactică şi Pedagogică, Bucureşti, 1985.
[11]. Popescu N., Dumitrescu C., *Tratamente termice şi prelucrări la cald*, E.D.P., Bucureşti, 1983.
[12]. Dulămiţă T., *Tehnologia tratamentelor termice*, E.D.P., Bucureşti, 1982.
[13]. Dulămiţă T., Florian E., *Tratamente termice şi termochimice*, Bucureşti, 1982.
[14]. Suciu Marcel-Valeriu, *Teza de doctorat*, Universitatea Tehnica din Cluj-Napoca, 1996.

THE ANNALS OF "DUNAREA DE JOS" UNIVERSITY OF GALATI
FASCICLE IX. METALLURGY AND MATERIALS SCIENCE
Nº. 4 - 2024, ISSN 2668-4748; e-ISSN 2668-4756
Article DOI: https://doi.org/10.35219/mms.2024.4.11

SCRAP METAL FROM CLASSES E1 AND E3 USED FOR STEEL MANUFACTURING IN CONNECTION WITH EUROPEAN LEGISLATION AND CLIMATE POLICIES

Mariana BUȘILĂ
Centre for Nanostructures and Functional Materials (CNMF) from the Interdisciplinary Research Centre in the field of Eco-Nano Technology and Innovative Materials (CC-ITI), "Dunarea de Jos" University of Galati, Romania
e-mail: mariana.busila@ugal.ro

ABSTRACT

To meet the challenges of the steel industry in the European Union related to natural resources and carbon resources, scrap recycling is crucial. Grade E1 (heavy iron) and E3 (mixed iron) are two of the scrap categories used in electric arc furnaces (EAF), a process that uses up to 70% recycled material. This significantly reduces the dependence on minerals and lowers CO_2 emissions compared to traditional blast furnace (BOF) processes.

In the European Union, scrap recycling accounts for around 40% of steel production, and most of the recycled material is used internally in the industry, with a recycling rate of up to 90%. Advanced sorting technologies, including artificial intelligence and hyperspectral imaging, improve the quality of scrap and reduce impurities, which can affect the final properties of the steel. This process also contributes to the circular economy, reducing waste and promoting the sustainable use of resources.

European climate policies, such as the Green Deal and circular economy regulations, support the use of scrap to decarbonise the steel industry. For example, EAF, which uses recycled iron, has a much lower environmental impact compared to traditional processes, saving up to 75% of carbon emissions, a key element of the transition to a greener and more sustainable steel industry in Europe. Thus, recycling scrap, mainly E1 and E3 grades, not only supports local economies and reduces costs, but also contributes significantly to achieving the European Union's climate goals, playing a role in the transition to a circular economy and reducing carbon emissions.

KEYWORDS: metal recycling, circular economy, CO_2 emissions, sustainability, European Green Deal, steel industry

1. Introduction

A strong and competitive steel sector is important to Europe's industrial base. The EU is the second largest steel producer in the world, producing over 177 million tonnes of steel per year, representing 11% of global production [1, 2]. Steel is also part of industrial value chains and is closely linked to many industrial sectors, such as automotive, construction, electronics, mechanical and electrical engineering [2, 3]. This has an important cross-border dimension: 500 production sites in 23 Member States make the steel industry truly European [1, 2]. The European steel sector is in a challenging situation today. The current economic crisis has led to a significant drop-in production activity and associated steel demand, which remains 27% below pre-crisis levels [4].

Steel has been a primary raw material in construction and manufacturing for a long time and will continue to be so in the foreseeable future. However, certain trends in steel production technology and usage could impact its demand. The development of collaborative projects and innovative manufacturing techniques are expected to be the main driving forces behind these trends [5]. Opportunities for innovative steel products will persist with the construction of power plants, transmission lines, and housing and transportation sectors, including onshore and offshore wind farms. [6].

THE ANNALS OF "DUNAREA DE JOS" UNIVERSITY OF GALATI
FASCICLE IX. METALLURGY AND MATERIALS SCIENCE
Nº. 4 - 2024, ISSN 2668-4748; e-ISSN 2668-4756
Article DOI: https://doi.org/10.35219/mms.2024.4.11

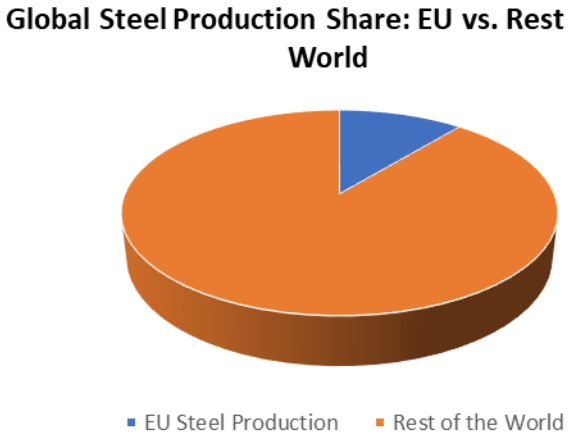

Fig. 1. *Global steel production share: EU vs. Rest of the World*

Even though innovation remains a major factor in the development of new products and new markets, as well as increasing efficiency, it is not the only factor that determines future trends in production. Access to raw materials and energy sources, as well as their prices, will determine, among other things, future trends, and since Europe depends heavily on imports, these prices are likely to remain high for some time [5]. The use of recycled waste as raw materials for steel production [increasing electric arc furnaces (EAFs)] and the use of gas instead of coking coal [when obtaining direct reduction iron (DRI)] could be significant technological trends in the future [7]. The efficient use of resources and climate policies will also be major factors in technological change.

In the short term, increasing the use of recycled waste and disseminating the Best Available Techniques (BAT) could contribute to achieving climate policy goals and improving the sustainable use of scarce resources [5].

2. Recyclable ferrous materials used in the steel-making process

Recycling ferrous materials is an important component of the steel-making process, significantly contributing to resource efficiency and sustainability. Ferrous scrap, which includes various grades of recycled steel, plays a vital role in modern steel production, particularly in Electric Arc Furnaces (EAFs). The EAF process is known for its ability to utilize scrap metal as a primary raw material, with approximately 70% of the input material often being ferrous scrap [8-11]. This method not only reduces the need for virgin materials but also lowers energy consumption and greenhouse gas emissions compared to traditional blast furnace methods [11, 12].

The composition of ferrous scrap can vary widely, affecting the quality and properties of the steel produced. Common impurities in recycled ferrous materials include copper, tin, and other alloying elements, which can adversely impact the mechanical properties of the final product [10, 13]. For instance, elevated copper levels in scrap can lead to issues such as hot shortness during rolling, which compromises the ductility and overall integrity of the steel [13]. Therefore, effective management of scrap quality is essential for maintaining the desired characteristics of the steel, necessitating advanced sorting and processing techniques to minimize contamination [10, 13].

The recycling process itself is facilitated by the inherent properties of steel, which can be recycled indefinitely without significant loss of quality. This characteristic is a cornerstone of the circular economy model, where the goal is to maximize resource use while minimizing waste [14, 15]. The recycling rate for iron is notably high, with estimates suggesting that over 90% of steel products are recycled at the end of their life cycle [16]. This high recycling ratio is attributed to well-established collection and processing systems that efficiently handle ferrous scrap [16].

Technological advancements have also played a significant role in enhancing the recycling of ferrous materials. Innovations such as hyperspectral imaging and artificial intelligence are being employed to improve the characterization and sorting of scrap, allowing for more precise control over the input materials used in steel production [13]. These technologies enable manufacturers to better predict the quality of the scrap and optimize the recycling process, thereby reducing the risks associated with impurities and enhancing the overall efficiency of steel production [13].

One study investigated the effect of the percentage of direct reduced iron (DRI) in the

THE ANNALS OF "DUNAREA DE JOS" UNIVERSITY OF GALATI
FASCICLE IX. METALLURGY AND MATERIALS SCIENCE
Nº. 4 - 2024, ISSN 2668-4748; e-ISSN 2668-4756
Article DOI: https://doi.org/10.35219/mms.2024.4.11

metallic charge on various steelmaking parameters and consumption figures in an electric arc furnace (EAF) [17]. The results showed that the percentage of DRI had a significant impact on electric energy consumption, oxygen consumption, coke consumption, and fluxing materials consumption. This study highlights the importance of considering the metallic charge composition in optimizing the steelmaking process and reducing resource consumption [17].

Another study focused on the production of sponge iron powder by reducing rolling mill scale. The reduction of mill scale allowed for the reuse of this material as metallic load in steel manufacturing or as a raw material in the production of iron-based powder metallurgy parts. This research demonstrates the potential for utilizing mill scale as a metallic charge to reduce waste and improve resource efficiency in the steel industry [18, 19].

Furthermore, a study investigated the influence of emulsol type on energy-power consumption and surface contamination in DC01 steel cold rolling on a continuous four-stand mill. The use of emulsols with higher kinematic viscosity was found to reduce the specific consumption of electricity in some cases. This research suggests that optimizing the properties of emulsols used in the rolling process can contribute to reducing energy consumption and improving the efficiency of electric mills [20].

Moreover, careful selection of the metal charge in electric furnaces, including the use of direct reduced iron (DRI) or recycled metallurgical waste, plays a key role in optimizing resource consumption, reducing pollution and improving the overall efficiency of the steelmaking process. This approach also contributes to significant savings by reducing the costs associated with raw materials and energy. In addition, recycling of ferrous materials supports economic development by creating jobs and stimulating growth in the recycling industry, highlighting its importance in the economic landscape and the sustainability of industrial processes.

Given the essential role of scrap recycling in optimising the steel production process and reducing environmental impact, it is important to understand how different scrap grades, such as E1 and E3, contribute to these processes. The percentages of use of these grades can vary depending on industrial sources and regions, and here is how these values can be approached and where relevant references can be found.

1. Grades E1 and E3 in standards:
- Grades E1 and E3 are defined according to the European standard EN 13920 for scrap metal, and their use is well documented in steel industry reports.
- E1 is predominantly used due to its higher weight and purity, being favoured for electric arc furnaces (EAF).
- E3, being a mixed grade, has a more varied but often lower utilization due to impurities.
2. Sources for statistical data:
- World Steel Association (worldsteel.org): Publishes annual reports on scrap metal recycling and consumption by region and category.
- Eurofer (European Steel Association): Includes information on ferrous material recycling in the EU, according to European standards.
- Local industry reports: Companies such as Liberty Steel or ArcelorMittal publish data on raw materials used, including scrap percentages.
3. General estimates:
- According to industry reports, E1 represents approximately 30-50% of scrap used in EAF due to its higher density and quality (Figure 2).
- E3 can contribute 15-25%, being more often used in combination with other grades, to balance costs and mechanical properties (Figure 2).

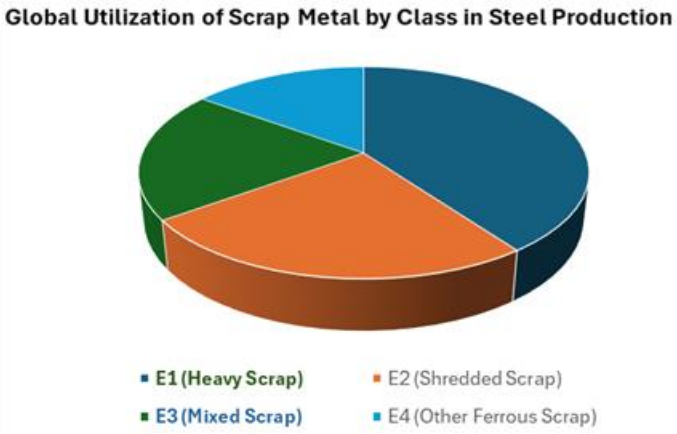

Fig. 2. *Global utilization of scrap metal by class in steel production*

3. Advanced technologies in recycling and production

Advanced technologies in recycling and production enhance the efficiency of ferrous metal recycling, reduce operational costs, and minimize environmental impact. Sorting systems based on hyperspectral imaging and artificial intelligence allow for the precise identification of impurities and the separation of materials. They facilitate the recycling process by increasing sorting efficiency and reducing material contamination [18].

Integrating recycled metals with other recycled materials, such as direct reduced iron (DRI), helps reduce energy and raw material consumption. This approach not only optimizes the production process, but also reduces CO_2 emissions associated with the extraction and processing of virgin minerals [18].

These technologies not only optimize the quality of the steel produced, but also contribute to reducing operational costs and environmental impact. For example, the use of scrap metal instead of raw ores reduces CO_2 emissions and limits the degradation of ecosystems.

4. European legislation and climate policies

The European Union places a strong emphasis on reducing carbon emissions and using resources efficiently through strategies such as the Green Deal and circular economy regulations. These policies encourage the use of scrap in the steel production process, a sustainable practice that aligns the industry with climate goals [21, 22].

European regulations also impose strict standards on the quality of recycled materials, requiring advanced sorting and processing technologies. This approach stimulates the adoption of Best Available Techniques (BAT), increasing the competitiveness of the industrial sector and reducing the environmental impact [21, 22].

5. Conclusions

Recycling scrap metal in classes E1 and E3 represents a pillar of sustainability in the steel industry, significantly contributing to reducing emissions and promoting a circular economic model.

Recycling ferrous materials is integral to the steel-making process, driven by environmental sustainability and economic efficiency.

The scrap metal materials undergo the melting process to create new or other steel products, which not only helps to reduce carbon emissions and waste but also aligns with the current European climate policies.

The ability to recycle steel indefinitely, combined with advancements in technology and a focus on quality management, positions the steel industry as a leader in the transition toward a circular economy. As the demand for sustainable practices continues to grow, the role of ferrous scrap in steel production will likely expand, further enhancing its significance in the global materials landscape.

Acknowledgment

This research was supported by grant number 795/10.11.2022, beneficiary Iulicris Recycling SRL Galati, Romania, entitled „Experimental research on the quality of metal waste, E1 and E3 class, with a view to their use in the development of general-purpose steels, in accordance with product standards", awarded to M.B.

References

[1]. Draxler M., *et al.*, *The steel industry in the European Union on the crossroad to carbon lean production-status, initiatives and challenges*, BHM Berg- Und Hüttenmännische Monatshefte, 165 (5), p. 221-226, https://doi.org/10.1007/s00501-020-00975-2, 2020.
[2]. Vögele S., *et al.*, *Challenges for the european steel industry: analysis, possible consequences and impacts on sustainable development*, Applied Energy, 264, 114633. https://doi.org/10.1016/j.apenergy.2020.114633, 2020.
[3]. Andreotti M., *Sdgs in the eu steel sector: a critical review of sustainability initiatives and approaches*, Sustainability, 15 (9), 7521, https://doi.org/10.3390/su15097521, 2023.
[4]. Grammatikos T., Vermeulen R., *The 2007-2009 financial crisis: changing market dynamics and the impact of credit supply and aggregate demand sensitivity*, SSRN Electronic Journal, https://doi.org/10.2139/ssrn.2054510, 2012.
[5]. Gajdzik B., *Post-pandemic steel production scenarios for poland based on forecasts of annual steel production volume*, Management Systems in Production Engineering, 31 (2), p. 172-190, https://doi.org/10.2478/mspe-2023-0019, 2023.
[6]. Diotti A., *et al.*, *Sustainable recycling of electric arc furnace steel slag as aggregate in concrete: effects on the environmental and technical performance*, Sustainability, 13 (2), 521, https://doi.org/10.3390/su13020521, 2021.
[7]. Vinayaka K., Puttaswamy P., *Prediction of arc voltage of electric arc furnace based on improved back propagation neural network*, Sn Computer Science, 2 (3), https://doi.org/10.1007/s42979-021-00556-1, 2021.
[8]. Xylia M., *et al.*, *Weighing regional scrap availability in global pathways for steel production processes*, Energy Efficiency, 11, p. 1135-1159, https://doi.org/10.1007/s12053-017-9583-7, 2018.
[9]. Yang M., *et al.*, *Circular economy strategies for combating climate change and other environmental issues*, Environ Chem Lett 21, p. 55-80, https://doi.org/10.1007/s10311-022-01499-6, 2023.
[10]. Panasiuk D., *et al.*, *International comparison of impurities mixing and accumulation in steel scrap*, Journal of Industrial Ecology, 26 (3), p. 1040-1050, https://doi.org/10.1111/jiec.13246, 2022.
[11]. Andrade C., *Steel circular economy in the civil construction: a study case of steel industry*, Mix Sustentável, 9 (5), p. 51-63, https://doi.org/10.29183/2447-3073.mix2023.v9.n5.51-63, 2023.

[12]. Rane K., Date P., *Recycling-cum-manufacturing process for utilization of finely divided ferrous metallic scrap*, https://doi.org/10.20944/preprints201809.0549.v1, 2018.
[13]. Cooper D., *et al.*, *The potential for material circularity and independence in the U.S. steel sector*, Journal of Industrial Ecology, 24 (4), p. 748-762, https://doi.org/10.1111/jiec.12971, 2020.
[14]. Miçooğullari S., *Circular economy, solid waste recovery, and growth: an empirical analysis for sustainable development in the 100th anniversary of the republic*, Gaziantep University Journal of Social Sciences, 22 (Cumhuriyet'in 100. Yılı), p. 373-385, https://doi.org/10.21547/jss.1354297, 2023.
[15]. Nakajima K., *et al.*, *Simultaneous material flow analysis of nickel, chromium, and molybdenum used in alloy steel by means of input–output analysis*, Environmental Science & Technology, 47 (9), p. 4653-4660, https://doi.org/10.1021/es3043559, 2013.
[16]. Guo M., Huang W., *Consumer willingness to recycle the wasted batteries of electric vehicles in the era of circular economy*, Sustainability, 15 (3), 2630, https://doi.org/10.3390/su15032630, 2023.
[17]. Hassan A., *et al.*, *Melting characteristics of alternative charging materials in an electric arc furnace steelmaking*, Ironmaking & Steelmaking, 48 (10), p. 1136-1141, https://doi.org/10.1080/03019233.2021.1945876, 2021.
[18]. Echterhof T., *Review on the use of alternative carbon sources in eaf steelmaking*, Metals, 11 (2), 222, https://doi.org/10.3390/met11020222, 2021.
[19]. Kirschen M., *et al.*, *Process Improvements for Direct Reduced Iron Melting in the Electric Arc Furnace with Emphasis on Slag Operation*, Processes, 9, 402, https://doi.org/10.3390/pr9020402, 2021.
[20]. Kukhar V., *et al.*, *Influence of emulsols type on energy-power consumption and surface contamination at dc01 steel cold rolling on the continuous four-stand mill*, Problems of Tribology, 27 (4/106), p. 19-26, https://doi.org/10.31891/2079-1372-2022-106-4-19-26, 2022.
[21]. ***, Home-https://european-steel.eu/assets/publications/reports-or-studies/annual-report-2023/FINAL_EUROFER_Annual-Report_2023.pdf.
[22]. ***, https://www.euric-aisbl.eu/images/Position-papers/feb-2023---boosting-steel-scrap-recycling_positionpaper_final.pdf.

THE ANNALS OF "DUNAREA DE JOS" UNIVERSITY OF GALATI
FASCICLE IX. METALLURGY AND MATERIALS SCIENCE
Nº. 4 - 2024, ISSN 2668-4748; e-ISSN 2668-4756
Article DOI: https://doi.org/10.35219/mms.2024.4.12

AN INTELLIGENT SYSTEM BASED ON ARDUINO FOR BLOOD LEAKAGE DETECTION

Mihaela MARIN[1,2], Cătălina ROŞU[1], Florin Bogdan MARIN[1,2]
[1] "Dunarea de Jos" University of Galati, Romania
[2] Interdisciplinary Research Centre in the Field of Eco-Nano Technology and Advance Materials CC-ITI, Faculty of Engineering, "Dunarea de Jos" University of Galati, Romania, 47 Domnească Street, RO-800008, Galaţi, Romania
e-mail: mihaela.marin@ugal.ro

ABSTRACT

Chronic kidney disease (CKD) is a global health issue, requiring renal replacement therapies like haemodialysis for patient survival. However, the procedure carries risks, particularly blood leakage, which can lead to severe complications. This study presents the design and implementation of an intelligent system that continuously monitors blood leakage during haemodialysis using an Arduino Nano-based platform. The main components include: a photoelectric sensor, HC-05 Bluetooth module, and piezoelectric buzzer, all integrated to detect blood loss and trigger alarms. The photoelectric sensor identifies blood leakage by sensing interruptions in an infrared beam, with data transmitted wirelessly to a mobile application. When leakage is detected, visual and auditory alerts are generated, allowing for immediate intervention. This system highlights the potential for IoT-enabled medical monitoring to improve the quality of life for haemodialysis patients through real-time data transmission and remote supervision.

KEYWORDS: blood leakage detection, Arduino, haemodialysis, chronic kidney disease, IoT

1. Introduction

Chronic kidney disease affects millions of people globally, and renal replacement therapy, as well as haemodialysis, is crucial for patient survival. In this context, effective monitoring of haemodialysis patients becomes essential to prevent complications and increase their quality of life [1-6]. The number of deaths caused by chronic kidney disease is globally prevalent [7], regardless of ethnicity, race, or gender. Chronic kidney disease is a serious and progressive condition that affects kidney function over the long term. It can result from a variety of factors, such as hypertension, diabetes, glomerulonephritis, or unidentified causes. (Figure 1) [8].

Haemodialysis is an essential medical procedure for patients with chronic or acute kidney failure who can no longer naturally eliminate toxins and excess fluids from the body. This technology has revolutionized kidney disease treatment, offering patients a new chance at life and an improved quality of life [9-12].

Haemodialysis involves extracting blood from the patient's body, filtering it through a dialysis machine to remove toxins and excess fluids, and then returning the purified blood to the body. Any interruptions, such as blood leakage, can lead to significant complications, including hypotension, anaemia, or infection [13-17]. Traditional methods of monitoring, which rely heavily on manual observation, are insufficient for ensuring rapid detection and response [18]. Here, Arduino-based systems provide a modern, automated solution. Arduino microcontrollers have become indispensable in developing intelligent systems for healthcare applications due to their versatility, affordability, and ease of use. In the context of haemodialysis, these microcontrollers offer a reliable platform for integrating multiple sensors, actuators, and communication modules, enabling real-time monitoring and efficient management of critical parameters [19-23].

THE ANNALS OF "DUNAREA DE JOS" UNIVERSITY OF GALATI
FASCICLE IX. METALLURGY AND MATERIALS SCIENCE
Nº. 4 - 2024, ISSN 2668-4748; e-ISSN 2668-4756
Article DOI: https://doi.org/10.35219/mms.2024.4.12

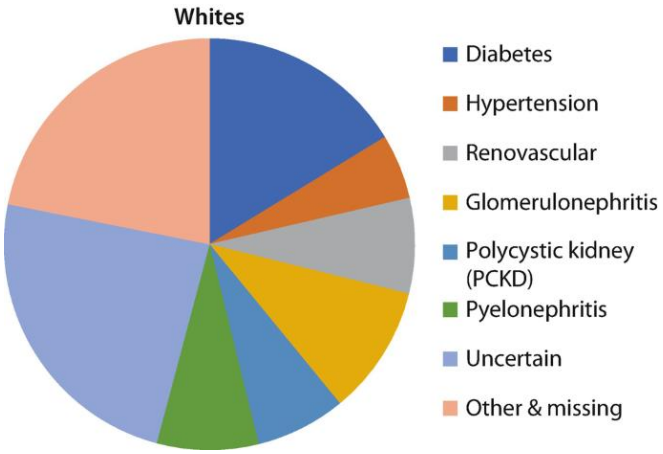

Fig. 1. *The causes of chronic kidney disease* [8]

2. Experimental procedure

The research consists of implementing an intelligent system for monitoring blood loss during haemodialysis therapy. The components used for this study, as shown in Figure 2, include the Arduino Nano board, Bluetooth module, photoelectric sensor, buzzer, and stop button. Once all elements are connected, the Arduino IDE platform and the code will be used to program the proposed system. There are two main components involved in the alarm system: the detection unit and the receiving unit. The sensing unit is responsible for detecting alarm conditions, while the receiving unit receives this information and can take appropriate action.

The detection unit is represented by the Arduino Nano board, together with the photoelectric sensor. The receiving unit is represented by the HC-05 Bluetooth module connected to the Arduino board and the mobile phone. This unit receives information from the sensing unit. The photoelectric sensor records the amount of blood loss, and the microcontroller analyse the received recording. The Arduino board to perform the calculations send the data to the buzzer and Bluetooth module. The mobile phone also being the receiving unit receive the transmitted data and the alarm will activate.

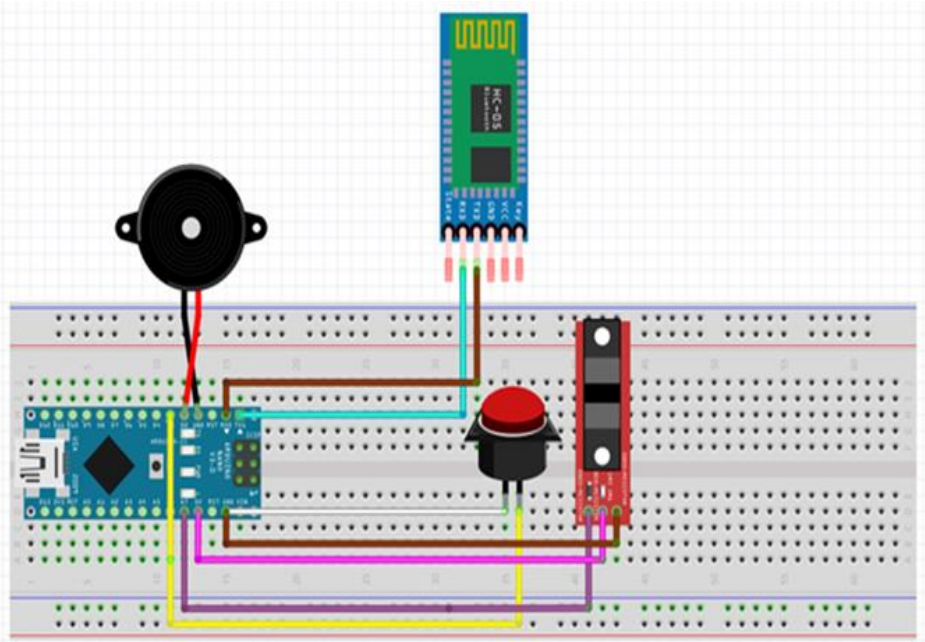

Fig. 2. *The system block diagram*

THE ANNALS OF "DUNAREA DE JOS" UNIVERSITY OF GALATI
FASCICLE IX. METALLURGY AND MATERIALS SCIENCE
Nº. 4 - 2024, ISSN 2668-4748; e-ISSN 2668-4756
Article DOI: https://doi.org/10.35219/mms.2024.4.12

The infrared photoelectric sensor has three pins: the supply pin (VCC), the ground pin (GND), and the output pin (OUT). The infrared photoelectric sensor is an optical coupling component, it is electrically isolated, divided into the emission part and the reception part. The principle is to convert input electrical signals into light, which causes the light emitting unit to emit infrared light. The receiving unit, the collector, receives the infrared light and will transform it into electrical signals, thus the receiving portion and the emitting portion of the photoelectric sensor become conductive.

The sensor model used is MOC7811 (Figure 3) for detecting blood leaks. When blood is present and interrupts the light beam, it is detected by the sensor, indicating the presence of blood. In cases of blood loss or a blockage in blood flow, the light beam will be obstructed, triggering warning signals.

The Arduino Nano (Figure 4) is a compact development board that is part of the diverse Arduino board range, which includes models such as Uno, Leonardo, Mega, and Micro. The microcontroller, composed of a central processing unit (CPU), memory, and various peripheral devices, performs the typical function of reading incoming data, performing calculations on this data, and controlling the environment based on the results.

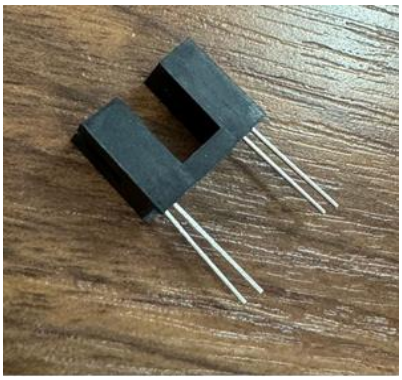

Fig. 3. *Connecting the sensor pins to the Microcontroller*

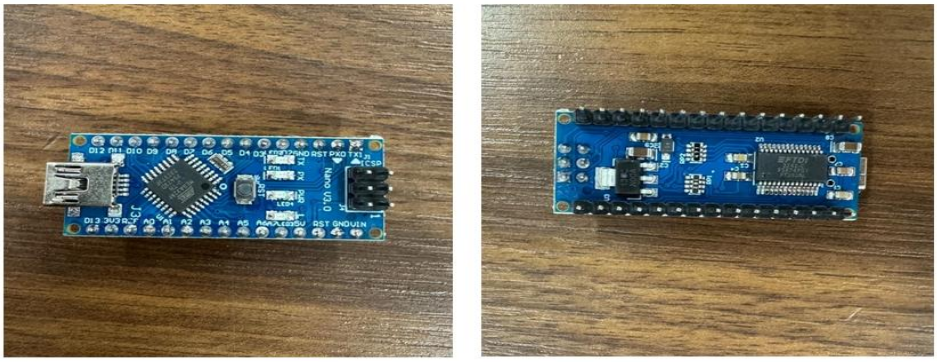

a b

Fig. 4. *Arduino Nano Microcontroller: a) front side; b) back side*

The HC-05 module (Figure 5) is designed for compatibility with Arduino microcontrollers, enabling wireless serial connections without the need for a direct line of sight between devices. Its cable-free operation, combined with low power consumption and minimal processing power requirements, makes it particularly suitable for healthcare devices. As a user-friendly Bluetooth SPP (Serial Port Protocol) module compliant with Bluetooth V2.0, the HC-05 offers a practical and efficient solution for a wide range of wireless applications.

a b

Fig. 5. *HC-05 Bluetooth Module: a) front side; b) back side*

Furthermore, Bluetooth is extremely relevant in the current context, where the large number of gadgets requires wireless solutions to avoid clutter and ensure efficient and convenient interfacing. The

THE ANNALS OF "DUNAREA DE JOS" UNIVERSITY OF GALATI
FASCICLE IX. METALLURGY AND MATERIALS SCIENCE
Nº. 4 - 2024, ISSN 2668-4748; e-ISSN 2668-4756
Article DOI: https://doi.org/10.35219/mms.2024.4.12

piezoelectric buzzer HND-2312 operates within a voltage range of 3-24V. The buzzer is used as an alarm that activates when the value read by the photoelectric sensor exceeds a certain threshold, indicating an issue. A warning sound is emitted until the alarm is manually deactivated.

Figure 6 illustrates the interface of the LEDS CONTROL APP, downloaded on a phone after the setup configurations are completed. The Bluetooth option is activated from the Android device settings, and in the LEDS CONTROL APP. The connection of the Arduino board with jumper wires is depicted in Figure 7. The connection of the photoelectric sensor on the breadboard is presented in Figure 8. The connection of the buzzer to the Arduino Nano system is presented in Figure 9. BT04-A is the Bluetooth module to which the connection is established, as shown in the Figure 10, managing serial communication to receive data from the Arduino. In Figure 11 is represented the connection of the stop button on the breadboard. In Figure 12 is illustrated the complete system configuration.

Fig. 6. *Interface of the LEDS CONTROL APP*

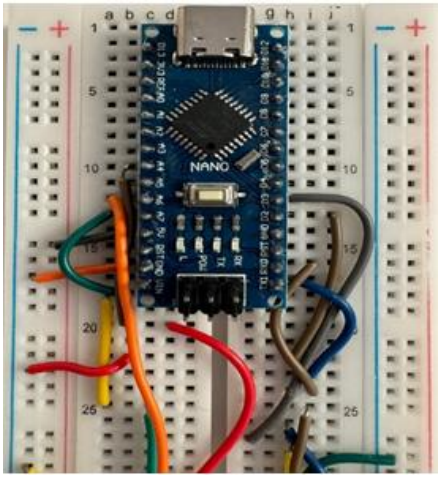

Fig. 7. *Connecting the Arduino board with jumper wires*

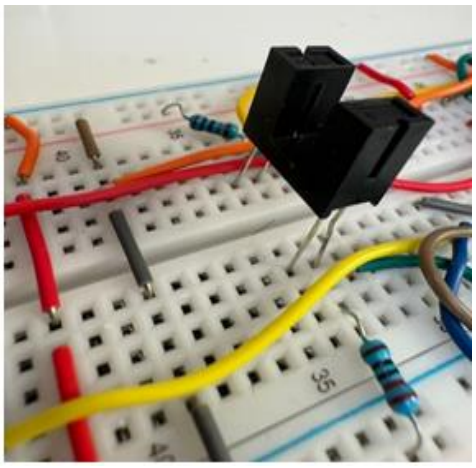

Fig. 8. *Connecting the photoelectric sensor on the breadboard*

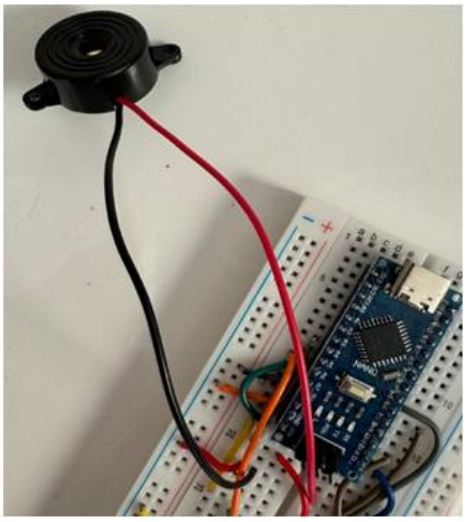

Fig. 9. *Connecting the buzzer*

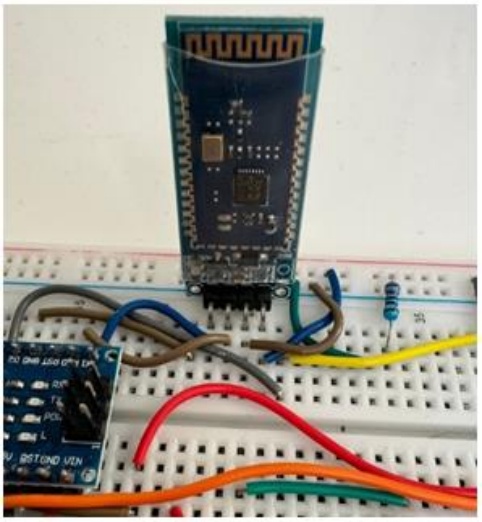

Fig. 10. *Connecting the Bluetooth module*

THE ANNALS OF "DUNAREA DE JOS" UNIVERSITY OF GALATI
FASCICLE IX. METALLURGY AND MATERIALS SCIENCE
Nº. 4 - 2024, ISSN 2668-4748; e-ISSN 2668-4756
Article DOI: https://doi.org/10.35219/mms.2024.4.12

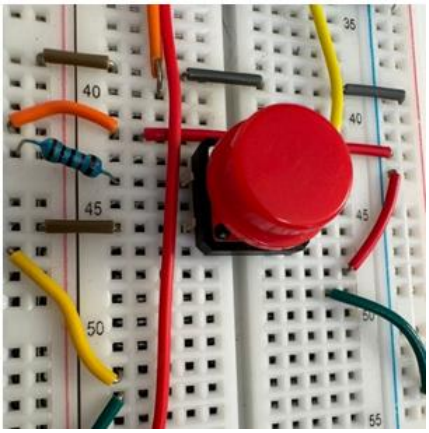

Fig. 11. *Connecting the stop button on the breadboard*

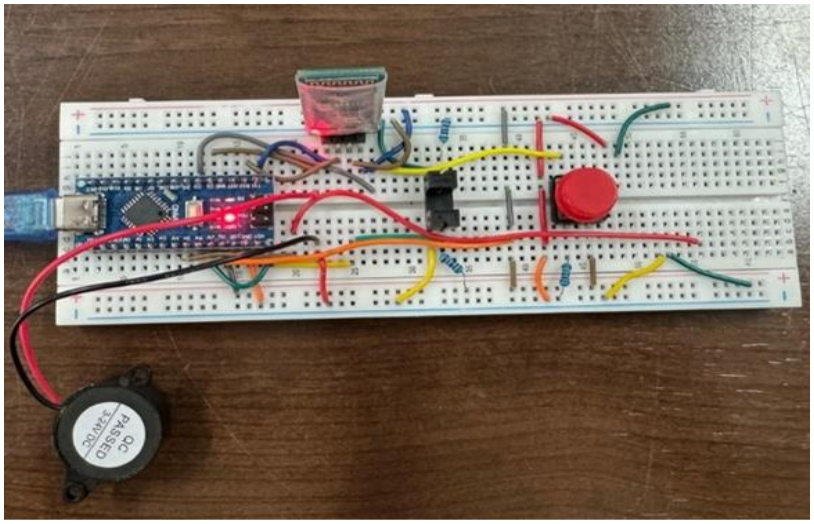

Fig. 12. *Complete system configuration*

3. Results and discussions

The primary components of the system as infrared photoelectric sensor, Arduino Nano microcontroller, HC-05 Bluetooth module, and buzzer work in tandem to monitor, detect, and alert in the event of blood leakage. The results indicate that the sensor achieved consistent readings in controlled environments, successfully detecting blood or blockage in the tubing. This is critical in haemodialysis, where even minor leaks can lead to significant health risks. The sensor's sensitivity threshold, set at a value of 1000, was adjusted for optimal balance between sensitivity and false positives, ensuring the system only triggered alarms in genuine cases of leakage.

When the value detected by the sensor exceeds a certain threshold (in this case, 1000), with the tube being red and at least 10 seconds having passed since the last alarm deactivation, the system will activate the alarm to notify the user (Figure 13), where the value displayed in the app is increased, and the alarm is triggered. On the mobile phone, the message displayed is "WARNING: LEAKAGE DETECTED!"

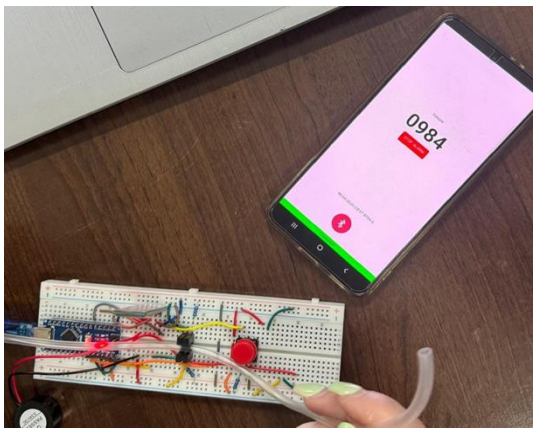

Fig. 12. *Initial value recorded by the sensor and tube placement*

THE ANNALS OF "DUNAREA DE JOS" UNIVERSITY OF GALATI
FASCICLE IX. METALLURGY AND MATERIALS SCIENCE
N°. 4 - 2024, ISSN 2668-4748; e-ISSN 2668-4756
Article DOI: https://doi.org/10.35219/mms.2024.4.12

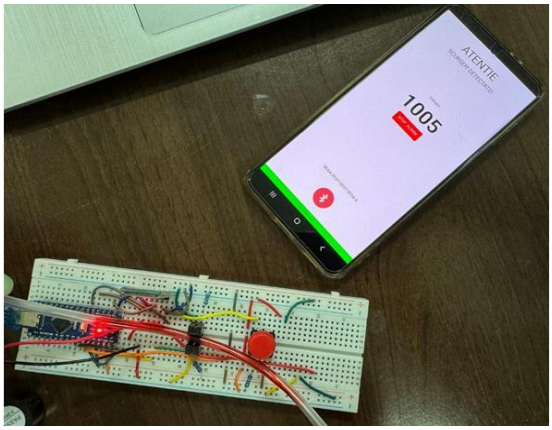

Fig. 13. *The red colour of the tube and the increased value activate the alarm*

4. Conclusions

The developed system demonstrated its ability to detect blood leakage through the use of an infrared photoelectric sensor connected to an Arduino Nano platform. Experimental tests showed that the sensor can accurately detect fluctuations in blood levels, triggering auditory and visual alarms in emergency situations.

During testing, the system demonstrated a prompt reaction time, with the buzzer activating within milliseconds of a detected leak, and a notification promptly sent to the mobile app. The 10-second delay before reactivation, designed to prevent continuous triggering, provided a balance between effective monitoring and alarm fatigue. When the threshold was reached, the tube's red colour was detected, visually and audibly signalling leakage to the user and mobile device.

Integrating the Bluetooth module into the system enabled real-time data transmission to the mobile application, LEDS CONTROL APP. This feature facilitates continuous remote monitoring of vital parameters, providing valuable information for quick intervention to both medical personnel and patients.

While the system performed well in simulated environments, further testing in clinical settings would provide additional insights into its real-world efficacy. Variability in tubing material or blood consistency could influence detection sensitivity, suggesting potential for further refinement in sensor calibration. Future enhancements may include the integration of advanced data analytics to predict leakage trends or the addition of Wi-Fi capability for broader connectivity. Additionally, including a battery backup and waterproofing measures could enhance its practicality in diverse clinical contexts.

The system's results, as well as the ease of use and reliability, highlight its potential for enhancing patient safety during haemodialysis.

References

[1]. Francis A., *et al.*, *Chronic kidney disease and the global public health agenda: an international consensus*, Nat Rev Nephrol 20, p. 473-485, 2024.
[2]. Bello A. K., *et al.*, *Epidemiology of haemodialysis outcomes*, Nat Rev Nephrol., 18 (6), p. 378-395, doi: 10.1038/s41581-022-00542-7, 2022.
[3]. Liew A., *Perspectives in renal replacement therapy: Haemodialysis*, Nephrology (Carlton), 23 Suppl 4, p. 95-99, doi: 10.1111/nep.13449, 2018.
[4]. Ifeoma I. Ulasi, *et al.*, *Chronic Kidney Disease Burden in Low-Resource Settings: Regional Perspectives*, Seminars in Nephrology, vol. 42, issue 5, 151336, 2022.
[5]. Vadakedath S., Kandi V. Dialysis, *A Review of the Mechanisms Underlying Complications in the Management of Chronic Renal Failure*, Cureus, 23, 9 (8), 2017.
[6]. Karkar A., *Modalities of hemodialysis: quality improvement*, Saudi J Kidney Dis Transpl., 23 (6), p. 1145-61, doi: 10.4103/1319-2442.103553. PMID: 23168842, 2012.
[7]. Kovesdy C. P., *Epidemiology of chronic kidney disease: an update*, Kidney Int Suppl (2011), 12 (1), p. 7-11, 2022.
[8]. O'Toole J. F., Sedor J. R., *Kidney disease: new technologies translate mechanisms to cure*, J Clin Invest., 124 (6), p. 2294-2298, 2014.
[9]. Thajudeen B., Issa D., Roy-Chaudhury P., *Advances in hemodialysis therapy*, Fac Rev., 16, 12:12, 2023.
[10]. Vega-Vega, Olynka y Toro-Cisneros, Noemí del, *Advances in Dialysis in the last Decade*, Rev. invest. clín. [online]., vol. 75, n. 6, p. 273-273, 2023.
[11]. Power Albert, Duncan Neill, Goodlad C., *Advances and innovations in dialysis in the 21st century*, Postgraduate medical journal., 85, p. 102-107, 10.1136/pgmj.2008.071837, 2009.
[12]. Abro A., *et al.*, *Chronic Kidney Disease: Epidemiology and Causes*, In: Harber, M. (eds) Primer on Nephrology, Springer, Cham., 2022.
[12]. Flythe J. E., *Dialysis-Past, Present, and Future: A Kidney360 Perspectives Series*, Kidney360, 4 (5), p. 567-568, 2023.
[13]. Kovesdy C. P., *Epidemiology of chronic kidney disease: an update*, Kidney Int Suppl (2011), 12 (1), p. 7-11, 2022.
[14]. Singh Ajit, Heldaus Jerome, Msaki Andrew, *Hemodialysis Complications: A Clinical Insight*, International Journal of All Research Education and Scientific Methods., 11, p. 2455-6211, 10.56025/IJARESM.2023.11323640, 2023.
[15]. Saha M., Allon M., *Diagnosis, Treatment, and Prevention of Hemodialysis Emergencies*, Clin J Am Soc Nephrol., 12 (2), p. 357-369, 2017.
[16]. Abe H., Mafune Ki., *Risk factors for maintenance hemodialysis patients undergoing elective and emergency abdominal surgery*, Surg Today 44, p. 1906-1911, 2014.
[17]. Frank T. Padberg, *Complications of arteriovenous hemodialysis access: Recognition and management*, Journal of Vascular Surgery, vol. 48, issue 5, Supplement, p. S55-S80, 2008.
[18]. Koirala N., Anvari E., McLennan G., *Monitoring and Surveillance of Hemodialysis Access*, Semin Intervent Radiol, 33 (1), p. 25-30, 2016.
[19]. Keshaviah P. R., Shaldon S., *Haemodialysis Monitors and Monitoring*, in: Drukker, W., Parsons, F.M., Maher, J.F. (eds) Replacement of Renal Function by Dialysis. Springer, Dordrecht, 1983.
[20]. Abel Mata-Lima, Ana Rita Paquete, José Javier Serrano-Olmedo, *Remote patient monitoring and management in nephrology: A systematic review*, Nefrología, vol. 44, issue 5, p. 639-667, 2024.

[21]. Ross Edward A., Jennifer L. Paugh-Miller, Robert W. Nappo, *Interventions to improve hemodialysis adequacy: protocols based on real-time monitoring of dialysate solute clearance*, Clinical Kidney Journal, 11, p. 394-399, 2017.

[22]. Paniagua Ramón, *et al.*, *Utility of Remote Monitoring in Patients on Automated Peritoneal Dialysis*, Revista de investigación clínica, 75 (6), p. 318-326, 2023.

[23]. Sandys V., Sexton D., O'Seaghdha C., *Artificial intelligence and digital health for volume maintenance in hemodialysis patients*, Hemodial Int., 26 (4), p. 480-495, 2022.

THE ANNALS OF "DUNAREA DE JOS" UNIVERSITY OF GALATI
FASCICLE IX. METALLURGY AND MATERIALS SCIENCE
Nº. 4 - 2024, ISSN 2668-4748; e-ISSN 2668-4756
Article DOI: https://doi.org/10.35219/mms.2024.4.13

THE EFFECT OF NATURAL AGEING HEAT TREATMENT ON THE MECHANICAL PROPERTIES OF THE AlZn4.5Mg1 ALLOY

Marian-Iulian NEACȘU
"Dunarea de Jos" University of Galati, Romania
e-mail: mneacsu@ugal.ro

ABSTRACT

In this paper, the influence of the time of artificial aging on the variation of the values of the mechanical properties of AlZn4.5Mg1 alloy was studied.

By applying the thermal processing variant described in the paper, an increase in the values of the resistance properties was obtained as the natural aging time increases to the value of 1080 hours. Above this value of the natural aging duration the values of the properties of mechanical strength record a decrease.

KEYWORDS: aluminium alloy, heat treatment, natural aging, mechanical characteristics

1. Introduction

Aluminium alloys are widely used in almost all branches of contemporary industry, so implicitly also in aeronautics due to special properties such as: high mechanical strength, low specific weight, chemical stability, etc, good thermal conductivity, good to very good corrosion resistance etc. [1, 2].

The close collaboration between aircraft manufacturers and metallurgical engineers has led to the production of materials with special characteristics.

Aluminium alloys have an elaboration technology with specific peculiarities, which are presented in the profile literature, and, what are determined on the one hand by the variation of their physical-mechanical properties and on the other hand by some conditions that they must meet, either in cast condition, be in deformed plastic state [2, 3].

For a long time, the main materials used in aeronautics were high-strength aluminium alloys of the dural type (Al-Cu-Mg), but their scope was reduced when alloys appeared special aluminium ziral (Al-Zn-Mg-Cu) [3].

The use of Al-Zn-Mg-Cu alloy blanks meant a gain in the weight of aircraft construction. Moreover, due to the high values of the flow limit of the alloy 7075 in the Al-Zn-Mg-Cu system, semi-finished products of this alloy can be used for most building elements loaded with compression loads (upper wing panels, fuselage compression area, poles, struts and ribs) [4].

Special aluminium alloys from Al-Zn-Mg-Cu system, of zicral type, it has special characteristics (such as high mechanical strength) that give it extra interest compared to other aluminium alloys, especially Al-Cu-Mg system alloys, of dural type, considered until recently to be the best performers [2].

The 7xxx series (Al-Zn-Mg-Cu) are aluminium alloys that are mainly used in the aerospace industry due to high-level mechanical properties. These mechanical characteristics are obtained by a control of the process of precipitation hardening [3-5].

Phase transformations in solid state, if allowed in the balance diagram of the alloy, it is an essential condition for achieving a heat treatment by tempering and natural or artificial aging on an aluminium alloy [4, 6, 7].

An alloy of this type is one that can withstand an order-disorder reaction; the hardening process that accompanies this process (similar to hardening by precipitation) is determined by the order-disorder reaction. The conditions for this form of hardening are quite strict, so the most important methods, often used for these alloys, are, they are based on precipitation from a supersaturated solid solution and eutectoid decomposition [7, 8].

In aluminium alloys with structural hardening, the increase in mechanical characteristics is due to complex interactions between the underlying matrix dislocations and precipitate particles occurring in the alloy structure following ageing [9].

The appearance of Guinier-Preston areas or precipitates of compound in the alloy structure determines in their vicinity a series of discontinuities

THE ANNALS OF "DUNAREA DE JOS" UNIVERSITY OF GALATI
FASCICLE IX. METALLURGY AND MATERIALS SCIENCE
Nº. 4 - 2024, ISSN 2668-4748; e-ISSN 2668-4756
Article DOI: https://doi.org/10.35219/mms.2024.4.13

of structural, chemical, energetic nature, etc. Depending on the nature of the discontinuities, there may be several mechanisms by which the mobility of these dislocations leading to the production of hardening of aluminium alloys is impaired [10].

2. Experimental conditions

Materials for experimental research are samples of an aluminium alloy of the Al-Zn-Mg-Cu system with the chemical composition shown in Table 1.

The values of the mechanical properties of the alloy studied according to EN 485-2-2007 [180] are shown in Table 2.

Experimental research on the influence of natural aging heat treatment on AlZn4.5Mg1 alloy was conducted according to the scheme in Figure 1.

The adopted research variant aims, for a degree of plastic deformation at hot = 25%, the influence of the maintenance duration at natural aging on the studied mechanical properties.

They were made for conducting experiments of the research variant, samples with dimensions: length = 105 mm; height = 5.7 mm; width = 60 mm.

Table 1. *Chemical composition of the alloy under investigation*

Element / Aloy	Zn	Mg	Cu	Si	Fe	Cr	Mn	Al
AlZn4.5Mg1	4.5	1.4	0.2	0.35	0.4	0.35	0.5	rest

Table 2. *Alloy properties according to EN 485-2-2007*

Proprieties / Aloy	Rm, [MPa]	$Rp_{0,2}$ [MPa]	A_5 [%]	HB
AlZn4.5Mg1	350	280	10	104

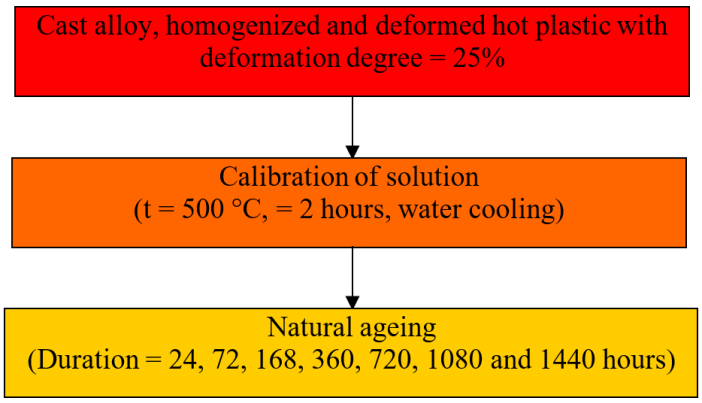

Fig. 1. *Schema de procesare termică adoptată*

3. Results of experimental research

After performing the heat treatment variant and performing the tests for finding out the values of the researched mechanical properties, the diagrams of variation of the mechanical characteristics studied according to the natural aging time according to Figures 2, were drawn up, 3, 4 and 5.

Figure 2 shows the variation in mechanical strength values (Rm) with natural aging time. Figure 3 shows variation in flow resistance values ($Rp_{0,2}$) of the alloy studied according to natural aging time. Figure 4 illustrates the variation in Brinell (HB) hardness with the natural ageing time at which the alloy under study was subjected. Figure 5 shows the variation in the elongation values at breakage (A5) with the natural ageing time at which the alloy under study was subjected.

THE ANNALS OF "DUNAREA DE JOS" UNIVERSITY OF GALATI
FASCICLE IX. METALLURGY AND MATERIALS SCIENCE
N°. 4 - 2024, ISSN 2668-4748; e-ISSN 2668-4756
Article DOI: https://doi.org/10.35219/mms.2024.4.13

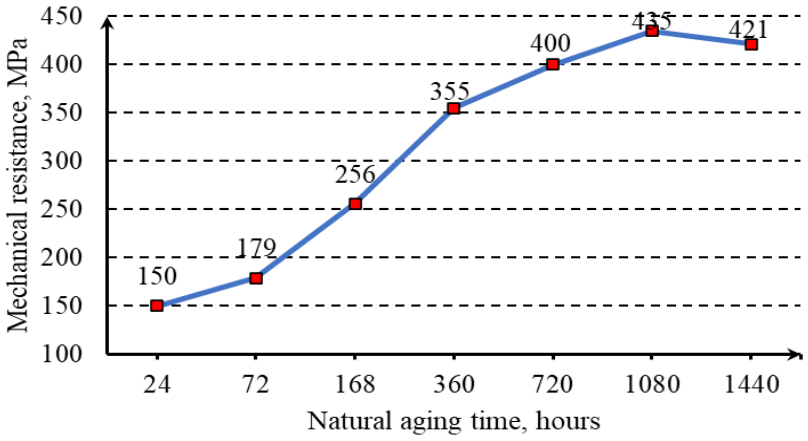

Fig. 2. *Variation of mechanical strength values with natural aging time*

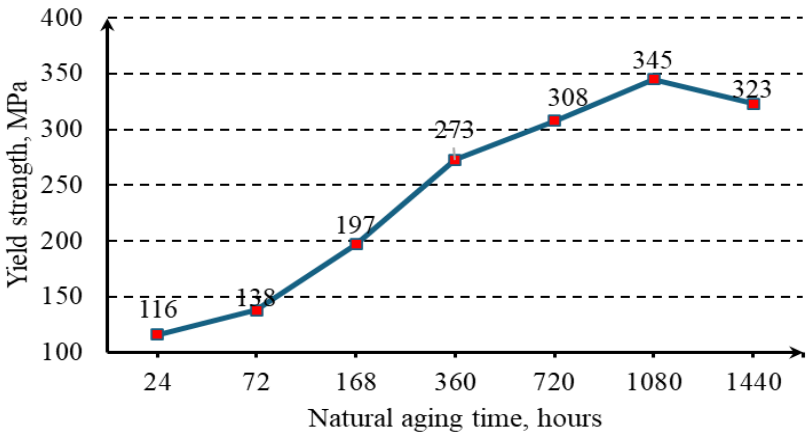

Fig. 3. *Variation in flow resistance values with natural aging time*

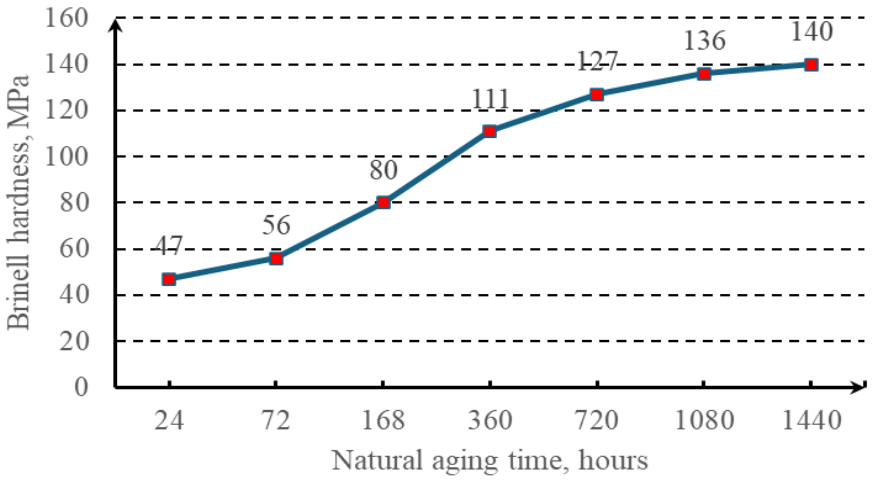

Fig. 4. *Variation of Brinell hardness values with natural aging time*

THE ANNALS OF "DUNAREA DE JOS" UNIVERSITY OF GALATI
FASCICLE IX. METALLURGY AND MATERIALS SCIENCE
No. 4 - 2024, ISSN 2668-4748; e-ISSN 2668-4756
Article DOI: https://doi.org/10.35219/mms.2024.4.13

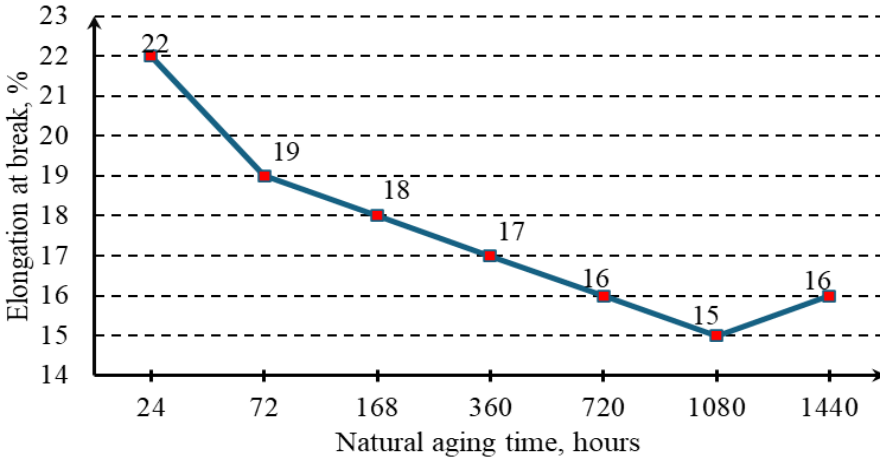

Fig. 5. *Variation of elongation values at breakage with natural aging time*

4. Conclusions

Specific for all three strength properties (Rm, $Rp_{0.2}$ and HB) after the realization of the heat processing variant is that they increase as the natural aging time increases, recording a maximum of 1080-hour aging time values. The further increase in natural aging time causes the values of these three resistance properties to begin to decline for the 1440-hour value of aging time.

As for the elongation at breakage, it is observed from the variation of the recorded values that the elongation decreases as the natural aging time increases.

The graph shows that the elongation records a minimum at the time of 1080 hours, after which a slight increase follows.

For both strength and elongation properties this variation is explained by the fact that the precipitates formed during the natural aging process have reached a critical value of their size, then follows their growth by coalescence.

More specifically, the growth of large ones occurs at the expense of small ones and structurally there is a decrease in the grain limits, which leads to a decrease in mechanical properties of strength, and, at the expense of plasticity.

References

[1]. Ioan Fara, *Aluminiul de la materia primă la produse finite*, Editura Tehnică, 2000.
[2]. Rajiv S. Mishra, Mageshwari Komarasamy, *Friction Stir Welding of High Strength 7XXX Aluminum Alloys*, 1st Edition, ISBN: 9780128094655, June 8, 2016.
[3]. Moldovan P., *Alliages nonferreux*, Ed. Matrix Rom Bucureşti, 2003.
[4]. Giacomelli I., *Aspecte privind unele procedee de îmbătrânire accelerată a aliajelor de aluminiu pentru turnare*, revista Construcţia de Maşini, nr. 8/1992.
[5]. Stoicănescu M., Giacomelli I., *Influenţa tratamentului termomagnetic asupra proprietăţilor aliajelor de aluminiu plasticizabile şi de turnare*, Revista de turnătorie, 4/2001.
[6]. Dumitrescu C., Şaban R., *Metalurgie fizică – Tratamente termice*, Editura, Fair Partners, Bucuresti, 2001.
[7]. Oajdea F. N., Dima M. I., *Experimental researches for the determination of the ATC şi 10Mg alloy fatigue life function of different thermal treatment cycles*, p. 5-8, Metalurgia Internaţional, vol. XV, special issue no. 2, ISSN 1582-2214, 2010.
[8]. Popescu R. M., Dima M. I., Oajdea F., *Special heat treatments applied to foundry aluminium alloy*, Metalurgia Internaţional vol. XIV, special issue no. 16, Editura Ştiinţifică F.M.R, p. 24-27, 2009.
[9]. Mac Kenzie Scott D., *Heat treating aluminium for aerospace applications*, The 13th IFHTSDE Congress, 7-10 October, Columbus, Ohio, p. 617-626, 2002.
[10]. Stoicănescu M., Giacomelli I., *Mechanical properties of aluminum alloys obtained as a result of unconventional heat treatment*, Conferinţa Internaţională de Ştiinţa şi Ingineria Materialelor, BRAMAT, 2005.

MANUSCRISELE, CĂRŢILE ŞI REVISTELE PENTRU SCHIMB, PRECUM ŞI ORICE CORESPONDENŢE SE VOR TRIMITE PE ADRESA:

MANUSCRIPTS, REVIEWS AND BOOKS FOR EXCHANGE COOPERATION, AS WELL AS ANY CORRESPONDANCE WILL BE MAILED TO:

LES MANUSCRIPTS, LES REVUES ET LES LIVRES POUR L'ECHANGE, TOUT AUSSI QUE LA CORRESPONDANCE SERONT ENVOYES A L'ADRESSE:

MANUSCKRIPTEN, ZIETSCHRITFTEN UND BUCHER FUR AUSTAUCH SOWIE DIE KORRESPONDENZ SID AN FOLGENDE ANSCHRIFT ZU SEDEN:

After the latest evaluation of the journals by the National Center for Science Policy and Scientometrics (**CENAPOSS**), in recognition of its quality and impact at national level, the journal will be included in the B^+ category, 215 code (http://cncsis.gov.ro/userfiles/file/CENAPOSS/Bplus_2011.pdf).

The journal is already indexed in:

DOAJ: https://doaj.org/

SCIPIO-RO: http://www.scipio.ro/web/182206

EBSCO: http://www.ebscohost.com/titleLists/a9h-journals.pdf

Google Academic: https://scholar.google.ro

Index Copernicus: https://journals.indexcopernicus.com

Crossref: https://search.crossref.org/

The papers published in this journal can be viewed on the website: http://www.gup.ugal.ro/ugaljournals/index.php/mms

Name and Address of Publisher:
Contact person: Prof. Dr. Eng. Elena MEREUȚĂ
Galati University Press - GUP
47 Domneasca St., 800008 - Galati, Romania
Phone: +40 336 130139
Fax: +40 236 461353
Email: gup@ugal.ro

Name and Address of Editor:
Ș. L. Dr. Eng. Marius BODOR
"Dunarea de Jos" University of Galati, Faculty of Engineering
111 Domneasca St., 800201 - Galati, Romania
Phone: +40 336 130208
Phone/Fax: +40 336 130283
Email: marius.bodor@ugal.ro

AFFILIATED WITH:

- THE ROMANIAN SOCIETY FOR METALLURGY
- THE ROMANIAN SOCIETY FOR CHEMISTRY
- THE ROMANIAN SOCIETY FOR BIOMATERIALS
- THE ROMANIAN TECHNICAL FOUNDRY SOCIETY
- THE MATERIALS INFORMATION SOCIETY (ASM INTERNATIONAL)

Edited under the care of the FACULTY OF ENGINEERING

Annual subscription (4 issues per year)

Fascicle DOI: https://doi.org/10.35219/mms

Volume DOI: https://doi.org/10.35219/mms.2024.4

Editing date: 15.12.2024
Number of issues: 200
Printed by Galati University Press (accredited by CNCSIS)
47 Domneasca Street, 800008, Galati, Romania